Evaluation of the effect of breast implants on the accuracy of the CT attenuation Correction (CTAC) map for SPECT/CT myocardial perfusion imaging: A phantom study

ABDULLAH JADIA ALANEZI

School of Health and Society

University of Salford

Submitted in Partial Fulfilment of the Requirements of the

Degree of Doctor of Philosophy (PhD)

2022

Research Supervisors

1- Professor Laurence Kenney (main supervisor)

School of Health and Society

Centre for Health Sciences Research, Brian Blatchford bldg.

University of Salford, Manchester M6 6PU

Email: L.P.J.Kenneyl@salford.ac.uk

2- Dr. John Thompson (co-supervisor)

School of Health and Society

Directorate of Radiography

L617, Allerton Building, Frederick Road Campus,

University of Salford, Manchester M6 6PU

Email: j.d.thompson@salford.ac.uk

3- Dr. Katy Szczepura (advisor)

School of Health and Society

Directorate of Radiography

L609, Allerton Building, Frederick Road Campus,

University of Salford, Manchester M6 6PU

Email: k.szczepura@salford.ac.uk

CONTENTS

List of Tables

List of Figures

Acknowledgements

I would like to express my gratitude and appreciation for Professor Laurence Kenney, Dr John Thompson and Dr Katy Szczepura for their consistent support and guidance during the running of this research project. Furthermore, my gratitude also extends to the staff at the Nuclear Medicine department in Manchester Royal Infirmary for facilitating the experiments in their facility. I would also like to give my sincere thanks to my deceased father, who died in December 2019 of cancer, and my deceased mother, who passed away 14 years ago, for their great role in my life and their numerous sacrifices for my brothers and me. I cannot thank them enough for all the support and love they have given me. I would never have made it here without them. I wish to thank them for everything. Allah, I ask You by Your mercy, which envelopes all things, that you forgive my parents. Everything is bought except fathers and mothers. My deceased father's dream was attending my graduation ceremony, but our God called him to paradise before my graduation date. I remember his words when I return to my study after every single holiday, 'My son, I am proud of you. Please concentrate on your study, try to do your best every time, and respect all people'. Dear father, without your support and patience, I could not have achieved any goal in my life. You were my teacher and guide. Thank you, Dad, for always believing in me even when I did not believe in myself. You made me what I am today. Thank you for your unconditional love.

I would like to express my deepest gratitude to my cute daughters, Kadi and Ghzal, and my cute sons, Naif and Turki who have supported me throughout this research project and for being good kids with their mother when I was studying at the university. I would like to thank my brothers, relatives and friends for their continuous support and endless prayers. Finally, I would like to thank my employers, the Ministry of Health, and the Saudi Cultural Bureau in London, for giving me the opportunity to perform this study

List of Abbreviations

Acronym	Definition
AAPM	American Association of Physicists in Medicine
AC	Attenuation Correction
ACR	American College of Radiology
ALARP	As low as Reasonably Practicable
ATCM	Automatic Tube Current Modulation
AUC	Area Under Curve
BHF	British Heart Foundation
BMI	Body Mass Index
BNMS	British Nuclear Medicine Society
CAD	Coronary Artery Disease
CCA	conventional coronary angiography
CCT	Cardiac Computed Tomography
CHD	Coronary heart disease
CT AC	Computed Tomography Attenuation Correction
CT	Computed Tomography
CVD	Cardiovascular Disease
FOV	Field Of View
ECG	Echocardiography,
FDA	Food and Drug Administration
FTC	Fixed Tube Current
FWHM	Full width at half maximum
GEME	General Electric Medical Systems
ICD	implantable cardioverter-defibrillator
HU	Hounsfield Units
IEC	International Electrotechnical Commission
IPEM	Institute of Physics and Engineering in Medicine
kV	Tube Kilovoltage
LAD	left anterior descending artery

LC_x	left circumflex branch
LV	Left Ventricle
mA	X-Ray Tube Milliampere (Tube Current)
MBq	Megabecquerel
MDCT	Multi-Detector Computed Tomography
MHRA	Medicines & Health Care products Regulatory Agency
MI	Myocardial Infarction
MPI	Myocardial Perfusion Imaging
MRI	Magnetic Resonance Imaging
NAC	Non – Attenuation Corrected
PET	Positron Emission Tomography
QC	Quality Control
RCA	Right Coronary Artery
ROI	Regions of interest
SD	Standard Deviation
SPECT	Single Photon Emission Computed Tomography
^{99m}TC	Technetium-99m

Abstract

Background: Myocardial perfusion imaging (MPI) using single photon emission computed tomography (SPECT) imaging can assess myocardial viability and perfusion. However, overlying thoracic structures, such as ribs or breast tissue lead to gamma ray attenuation. This attenuation does not occur equally for all body regions. Photons emitted from deeper structures will undergo more attenuation than superficial structures, causing artefacts within the image that can mimic pathology - such as ischaemia. Such artefacts can be removed or minimised by using attenuation correction (AC) maps generated using computed tomography (CT). Breast implants that have density higher than normal breast tissue, could affect the accuracy of the CT numbers used for AC.

Methods: Imaging protocols were compared with and without three sizes of breast implant, in a phantom study. The first experiment used a diagnostic CT scanner to design the method. The second experiment was carried out in a clinical centre using the CT components of a SPECT/CT scanner to assess the impact of three different breast implants on CT number accuracy when the CTAC is applied in SPECT/CT MPI. The last experiment used a clinical SPECT/CT scanner and ^{99m}TC as a radiotracer to mimic the clinical MPI scan.

Results: The first and second experiments found that large breast implants led to a greater difference in CT HU and CT numbers compared to baseline, than the small or medium implants, but the differences were within the tolerance range (±5HUs). This suggested that even large breast implants did not impact in a clinically significant way on the accuracy of CT HUs and CT numbers. However, the third experiment found that large breast implants resulted in a more significant difference in corrected counts and thus more overcorrection than small or medium breast implants.

Conclusion: The study illustrates that large breast implants resulted in a greater differences in CT HUs, CT number and corrected counts than small or medium implants. Increasing the tube current (mA) improves the CT HU accuracy without significant impact, apart from an increase in the radiation dose to the patient.

Chapter 1: Introduction

Coronary artery disease (CAD) typically arises as a result of a blockage in the arteries supplying oxygenated blood to the heart. A partial blockage can lead to decreased myocardial blood flow to the heart, which is commonly experienced in the form of shortness of breath and chest pains. When these vessels are entirely blocked, it can cause myocardial infarction and subsequently irreversible damage to the myocardium due to a continuous lack of oxygenated blood. Importantly, CAD is recognised as the most common form of heart disease and is the one of the key causes of death in the West (Goetze et al., 2007)

Treatment can be more effective and complications such as heart attacks prevented if CAD is diagnosed early. The aim of diagnosing CAD in the early stages is to identify patients who would benefit from treatment and hence minimise the risk of mortality, reduce costs and improve patients' lifestyles. Imaging tests can be particularly beneficial in diagnosing CAD because these tests can examine the structure and function of the heart. Accuracy in diagnosing CAD is therefore essential to minimise unnecessary procedures (Douglas & Daubert, 2015). Nuclear cardiology with myocardial perfusion imaging (MPI) has achieved clinical acceptance as the standard of care for patients with known or suspected CAD. MPI is regarded as the most common, least invasive imaging approach when seeking to diagnose and implement risk stratification among patients with CAD (Underwood et al., 2004). MPI using single-photon emission computed tomography (SPECT), a nuclear medicine imaging test, is widely used to confirm or exclude a diagnosis of coronary obstruction in patients with clinically suspected CAD (Underwood et al., 2004). When using this functional imaging technique, a small amount of radiotracer is injected into the patient to show how well blood flows through the cardiac muscle. MPI using SPECT can be applied to assess myocardial viability and perfusion. In nuclear cardiology, SPECT and CT imaging are used in the same scanner; a CT scanner is combined with a SPECT scanner and is called hybrid imaging. CT technology generates data depending on the differences in the attenuation levels of the scanned area (Rodriguez-Granillo et al., 2015). A CT scanner is used to determine the exact anatomic location of the region and compensate for photon attenuation. Image acquisition occurs within a CT scanner as the X-ray tube and detectors rotate around the patient. The exit radiation is calculated by the detectors multiple times, and the data are sent to a computer. SPECT/CT is a hybrid imaging technique that integrates two modalities (CT and SPECT), thus offering anatomical and functional images in one scan. One of the main advantages of SPECT/CT is that it provides accurate anatomic localisation of an identified abnormality and thereby improves the diagnostic accuracy and

specificity of nuclear medicine studies (Israel et al., 2019). Notwithstanding, SPECT/CT in MPI to detect CAD has some limitations, and the diagnosis of CAD can be challenging.

Attenuation artefacts are one of the main limitations of SPECT MPI scans. These artefacts can occur due to technical errors, such as inadequate equipment quality control (QC), or part of the patient's anatomy, such as breast. The artefacts ensue due to photons that arise in the myocardium interacting with the tissue around the cardiac area. These photons may be absorbed or scattered before detection by gamma detectors. Breast attenuation is one of the main soft tissue artefacts for female patients, with the number of photons attenuated based on variations in breast size, shape and position. Artefacts in images can be defined as features that appear but do not exist in the true object being imaged. These features can mimic pathology, obscure pathology or degrade the image quality. For instance, breast attenuation artefacts can mimic a fixed perfusion defect in the left ventricle wall (false positive result). The severity of the artefacts depends on the breast size and density (Garcia, 2016; Walz-Flannigan et al., 2018), with the most common cardiac segment affected by breast attenuation being the anterior wall of the left ventricle. Furthermore, breast implants can prevent the meaningful estimation of myocardial perfusion by a SPECT gamma camera owing to the significant artefacts that can be created by their presence (Farag & Heo, 2015; Henzlova & Duvall, 2019).

In 2021, 93% of the 14,354 cosmetic procedures in the UK were performed on women, a fall of 26% from 2020. The number of breast augmentation procedures performed in the UK peaked in 2013 at over 11 thousand, while it dropped in the subsequent years reaching approximately four thousand in 2021. Breast augmentation was the top surgical procedure for women in 2021: 4,010. However, breast augmentation was not of the top surgical procedure for men in the same period. (SURGEONS, 28 February 2021).

Overlying structures such as breast tissue can also create artefacts due to the attenuation of the emitted gamma rays. The attenuation of the emitted radiation decreases the specificity test, which makes it difficult to differentiate between CAD and breast attenuation artefacts. This may give the appearance of perfusion defects that are indicative of pathology (Hasan Raza, 2016). Not addressing breast soft tissue artefacts may lead to unnecessary tests, including invasive cardiac catheterisation, with the burden of additional risk and expense (Gimelli et al., 2013; Qutbi & Soltanshahi, 2018). Because breast soft tissue can reduce radioisotope uptake and appear as a defect, a hybrid system such as SPECT/CT can improve the photon attenuation of soft tissue through the application of attenuation correction (AC), which improves diagnostic

performance. Such artefacts can be removed or minimised using AC maps generated from CT images. Furthermore, CT is used to generate AC to compensate for any photons that may be attenuated by soft breast tissue. AC is the main technique used to improve the sensitivity and specificity of diagnostic CAD as it reduces the possibility of misdiagnoses and decreases the likelihood of false positive defects. Many previous studies have found that AC increases specificity compared to non-corrected images.

Although various techniques can be used to apply AC to improve diagnostic accuracy, CT AC is the most common technique used in clinical practice. AC improves the diagnostic accuracy of SPECT MPI, mainly in women who have large breast. AC also decreases the need for rest images when the stressed image is acquired beforehand, so patients will not receive any additional radiotracer doses (Gimelli et al., 2013; Huang et al., 2016, 2019; Mannarino et al., 2019).

While various artefacts can degrade the quality of reconstructed CT images, one of the primary sources of these artefacts is high-density objects, such as breast implants. Their presence may lead to incorrect CT numbers. This may in turn affect diagnostic accuracy, leading to a false positive diagnosis and thus cause unnecessary cardiac diagnostic tests, such as invasive coronary angiography which carry an increased risk of complications (Iskandrian & Garcia, 2016; Walz-Flannigan, Brossoit, Magnuson, & Schueler, 2018). These artefacts can have a significant effect on cardiac diagnostic accuracy.

To the best of my knowledge, no previous studies have considered the effect of breast implants, including different sizes, on diagnostic accuracy in either a phantom or patient-based study. Furthermore, no studies have thus far examined the impact of breast implants of various sizes on the accuracy of AC maps for the CT component of SPECT MPI. Any inaccuracies in measuring CT numbers as a result of the aforementioned factors may therefore lead to inaccuracies in the AC compensation, which may influence CAD diagnosis. The accuracy of the CT numbers used for AC in SPECT MPI is essential for ensuring proper corrections are applied to emission maps. While a larger breast may cause artefacts in the SPECT data, no previous studies have shown whether artefacts caused by dense materials affect the accuracy of CT values. The smallest differences in CT numbers between the reference (no breast implant attached) and different breast implant sizes in the cardiac region could be considered important indications for choosing the optimum parameters for clinical acquisitions.

Chapter 2: Background and Literature Review

Numerous factors can affect the diagnostic performance of myocardium perfusion. These include breast size variations, which may impact photon attenuation, and breast implant materials, which may be denser than normal breast tissue, thus causing high breast attenuation artefacts in MPI. It is therefore important to understand the main anatomical components of cardiac and female breast anatomy, including the soft tissue structures, when considering the imaging challenges inherent to the diagnosis of CAD, particularly among female patients with breast implants. It is also essential to understand the techniques and tests used to diagnose CAD in order to compare each technique. In this chapter, the focus is on CT components and artefacts due to CT scanners being integrated with SPECT gamma cameras as a hybrid system. CT is used to generate AC to compensate for any photons that may be attenuated by breast soft tissue. Furthermore, understanding attenuation and AC helps explain how attenuation photons may affect the diagnostic accuracy of myocardial perfusion.

Accordingly, a comprehensive search of the literature was conducted via ScienceDirect, PubMed, Medline and Google Scholar to identify relevant articles. The search was limited to articles written in English. The following terms were used: breast, breast implants, attenuation, attenuation correction (AC), CT number, soft tissue attenuation, SPECT artefacts, myocardial perfusion imaging (MPI), photons interactions and CT technology.

2.1 Coronary Artery Disease (CAD)

Coronary artery disease (CAD) is a reduction in the blood flow in the arteries supplying oxygenated blood to the heart. When these vessels are entirely blocked, myocardial infarction and irreversible damage to the myocardium occurs (Goetze, Brown, Lavely, Zhang, & Bengel, 2007). CAD is the most common form of cardiac disease and is one of the leading causes of morbidity and mortality in the Western world (Cassar, Holmes Jr, Rihal, & Gersh, 2009), as the disease is steadily increasing among developing countries. Accuracy in diagnosing CAD is essential to minimise unnecessary procedures (Douglas & Daubert, 2015). The aim of diagnosis in the early stages of CAD is to identify patients who would benefit from treatment, hence minimising the mortality rate and cost and improving patient lifestyle.

2.2 Heart Anatomy and Physiology

2.2.1 The Heart's Anatomy

Understanding the heart's anatomical structure is important for understanding its function. The heart is located in the middle of the human body in the lower part of the thoracic cavity between the lungs. It consists of four chambers: the right atrium, right ventricle, left atrium and left ventricle (LV). The small superior chambers that receive blood into the heart are called the atria, whereas the large inferior chambers that pump blood out of the heart are called the ventricles (Philip I. Aaronson, 2013). The left atrium receives oxygenated blood from the lungs and pumps this blood into the LV. The function of the right atrium is to receive deoxygenated blood returning from other parts of the body. The right ventricle supplies blood to the pulmonary system for oxygen extraction, and the LV supplies blood to the entire body, including the lungs.

2.2.1.1 The Heart's Blood Vessels

The heart's six major blood vessels are the larger arteries and veins that connect to the atria and ventricles and carry blood to and from the heart. These blood vessels are called the aorta, the pulmonary artery, the pulmonary vein, the superior and inferior vena cava and the coronary arteries. The function of the aorta is to carry blood from the heart into the system's circulation. The pulmonary artery carries deoxygenated blood away from the right side of the heart and into the lungs for gas exchange, while the pulmonary veins carry oxygenated blood from the lungs to the left atrium. The large superior and inferior venae cava carry deoxygenated blood from the upper and lower parts of the body to the right atrium. The coronary arteries, which are the focus of this thesis, supply blood to the muscles of the heart (Sherwood, 2010).

2.2.1.2 The Heart's Chambers and Muscles

The four chambers of the heart are separated by septa and valves. Deoxygenated blood pools into the right atrium from the superior and inferior vena cava, and this blood pumps into the right ventricle through the tricuspid valve, which regulates the flow of blood between the right atrium and the right ventricle. Blood is ejected through the pulmonary valve, which regulates the flow of blood from the right ventricle into the pulmonary arteries during ventricular systole. Blood then enters the left atrium, moves through the mitral valve, allowing oxygenated blood to move from the left atrium into the LV, and exits for systemic circulation via the aortic valve (Levick, 2013).

The heart wall consists of three muscles: the pericardium, myocardium and endocardium. The pericardium is a thin layer that surrounds the heart, and it protects the heart by reducing friction. The myocardium is the middle and thickest layer of the heart wall; it is responsible for maintaining the heart's pumping of blood around the body. The endocardium is the inner layer that lines the valves, which open and close to regulate blood flow within the heart chambers (Aaronson, Ward, & Connolly, 2020). The heart muscles are supplied by the coronary arteries. The function of the coronary arteries is to deliver oxygenated blood to the heart muscles (Levick, 2013).

2.2.1.3 The Coronary Arteries

The coronary arteries originate from the aorta and are then divided into the left coronary artery (LCA) and the right coronary artery (RCA). The LCA splits into two branches: the left circumflex artery (LCX) and the left anterior descending artery (LAD). These arteries supply the left and anterior parts of the heart, whereas the RCA supplies the right and posterior part of the heart (Figure 1). The RCA originates from the right aortic sinus of the ascending aorta, moves anteriorly and to the right between the right auricle and the pulmonary artery and then descends vertically into the right atrioventricular sulcus. The length of the RCA ranges from 12 to 14 cm (Francesco Faletra, 2008; Frank H. Netter, 2014; Villa et al., 2016).
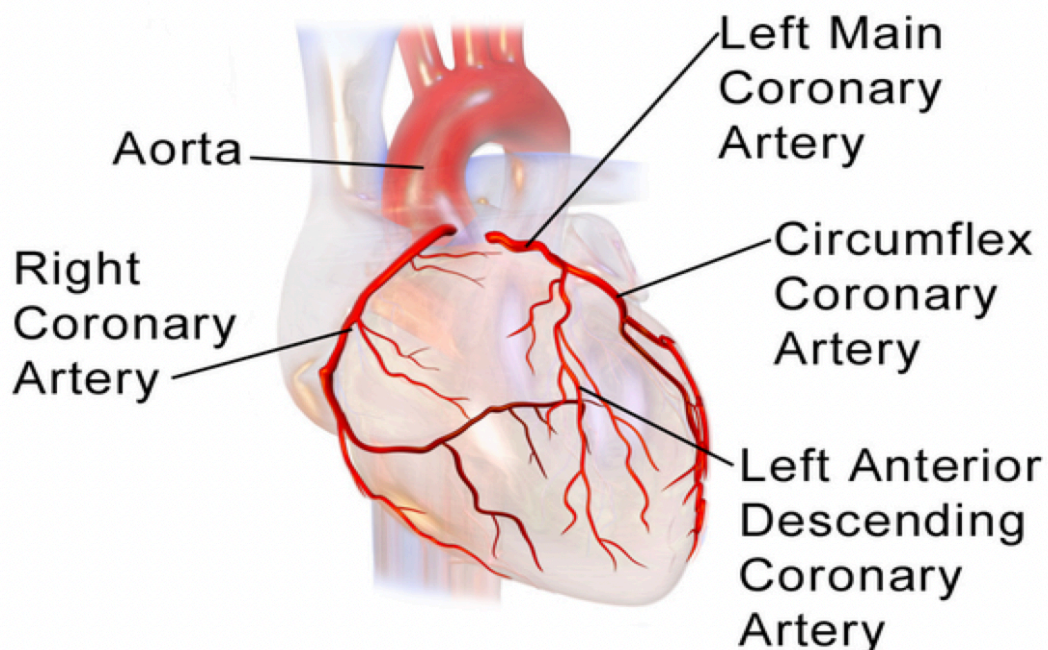
Figure 1: An illustration of the anatomy of the cardiac coronary system (Wikipedia, April 7, 2021).

The LCA originates from the left aortic sinus of the ascending aorta. It lies mainly between the pulmonary trunk and the auricle of the left atrium. The normal length of the LCA ranges from 2 mm to 4 cm (Francesco Faletra, 2008). It moves behind the pulmonary trunk for 5–10 mm before dividing into the LAD artery, which supplies the anteroseptal heart wall, and the LC_X, which supplies the posterior and lateral sides (Villa et al., 2016). The normal length of the LAD ranges from 10 to 13 cm, and the normal length of the LCX ranges from 5 to 8 cm.

As will be described in the next section, stenosis of the arterial wall can cause a reduction in the required blood flow, which can contribute to the malfunctioning of the heart.

2.3 Definition of CAD and Its Causes

CAD is defined as the narrowing or blockage of the coronary arteries. The most common reason behind CAD is a build-up of fatty (atherosclerosis) deposits along the walls of the coronary artery (Mujoriya & Bodla, 2012). Atherosclerosis is characterised by a hardening of the arterial walls and the narrowing of the internal artery diameter, which leads to the gradual narrowing and restriction of blood flow to the heart muscles (see Figure 2; Townsend et al., 2015).
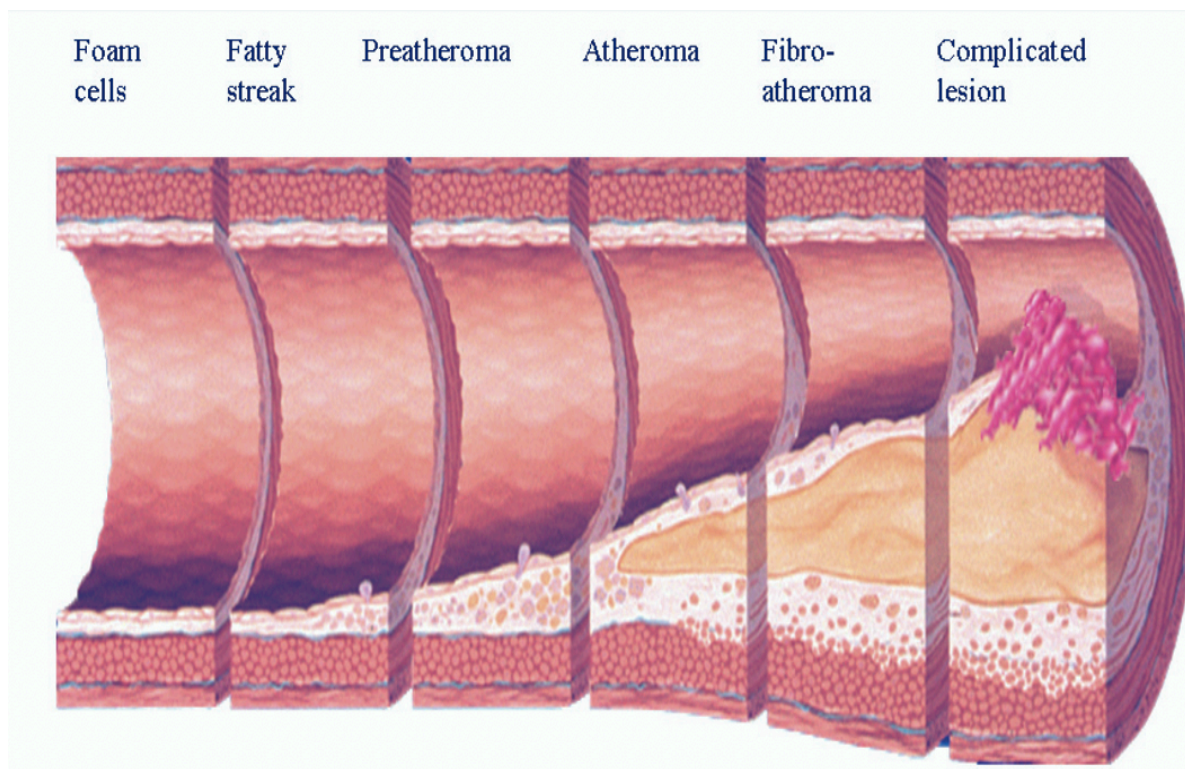
Figure 2: Progression of atherosclerosis (Stary et al., 1995).

Atherosclerosis is a slow process that takes decades to develop into a pathological condition. Atherosclerosis progresses through various stages. The first stage of atherosclerosis is the appearance of irregular yellow-white discolouration (foam cells) on the surface of the inner artery. This occurs in most people by the age of 20. The second stage involves fatty streaks. The fatty streaks are lipid-containing foam cells in the wall of the artery. Over time, these fatty streaks can develop into atherosclerosis lesions, which can be visible using histology. The third stage is preatheromas, which form the bridge between early and advanced lesions. The disease becomes clinically obvious with the development of fibrous plaque. The fourth stage is called atheroma, which is the accumulation of cells that include lipids and fibrous connective tissue between the endothelium lining and the artery walls' smooth muscle cells. This can develop by the end of the third decade of life. The fifth stage is called fibroatheroma, which is the first of the advanced lesions of atherosclerosis. The final stage can be critical stenosis, which considerably minimises the diameter of the artery. Once the plaque ruptures, it can lead to a thrombus, which is a blood clot that can cause partial or complete blockage of the artery (Odeberg et al., 2014).

2.4 Risk Factors of CAD

Various factors can increase the risk of developing CAD, including preventable factors such as lifestyle (e.g. alcohol consumption, diet, physical inactivity and smoking), non-preventable factors (e.g. age, gender, family history), and metabolic factors (e.g. diabetes) (Hajar, 2017), table 1 summarises the preventable risk factors. When the coronary arteries are narrowed, the amount of oxygenated blood that can pass through the vessels and perfuse the myocardium is reduced. As a result, the partially blocked coronary arteries may no longer be capable of meeting the demand for oxygenated blood required by the myocardium due to exercise (stress). This reduction in oxygenated blood to the heart muscle (called ischaemia) creates angina (chest pain). When the coronary artery is completely blocked, a portion of the heart muscle dies (myocardial infarction; (Boyette & Manna, 2019).

Table 1: coronary artery disease (CAD) preventable risk factors

Risk Factor	How Each Factor Contributes to CAD Development
Smoking	Smoking is one reason for the reduction of blood vessel distensibility. Smoking can lead to an increase in coronary artery wall stiffness. Smoking is also associated with increased fibrinogen levels, increased platelet aggregation and decreased High blood cholesterol (HDL) cholesterol levels. Hence, it can cause damage to an endothelial cell of an artery, and then plaque can form, which can lead to plaque rupture and thrombosis (Ambrose & Barua, 2004).
High blood cholesterol	Cholesterol is a fatty substance found in the blood. The probability of plaque build-up in the cardiac artery increases with increased blood cholesterol levels.
Obesity	Obesity is associated with an increase in blood pressure, which can cause endothelial injury, an initial step in atherosclerosis (MacCance, 2010). Because obese individuals typically have a high amount of fat, there is also an association with high blood cholesterol (Ades & Savage, 2017).
Diabetes mellitus	A person with poorly controlled diabetes mellitus can experience high blood sugar (glucose) levels, which can damage blood vessels and lead to plaques (National Institute of Health, 2005).

2.5 Prevalence, Incidence and Demographics of CAD

Approximately 2.3 million people in the UK have CAD, with around 1.5 million being male and 830,000 being female. The incidence of CAD has declined in the UK in recent years due to favourable changes in risk factors, such as a decline in smoking. The incidence rate of CAD in the UK has declined by about 3% between 2013 and 2017 in both men and women aged < 54 years old and by approximately 16% for those over 75.

The prevalence of CAD increases with age and is higher in males than females (Malakar et al., 2019). In the UK, more than 2.3 million people are currently living with CAD. However, in the UK, the prevalence of CAD decreased by about 19% between 2013 and 2017 for both men and women. The prevalence among males decreased by approximately 14%, whereas it declined by 30% among women. In 2017, the prevalence of CAD in the UK in people aged 65 years and

over was 11.4%, compared to 2.7% in people in the 45–54 age group (Bhatnagar, Wickramasinghe, Wilkins, & Townsend, 2016).

2.6 Mortality Rate of CAD

CAD remains the leading cause of death for both men and women worldwide. CAD is the leading cause of death worldwide and is also the leading cause of mortality in the UK, where it accounts for 13% of premature deaths in males and 8% in females. The number of deaths due to CAD in the UK in 2018 was 40,395 men and 23,737 women, but with age, the mortality gap narrows. The British Heart Foundation's (BHF, 2018) figures show that, over the age of 75, more women than men die of CAD.

CAD death rates in the UK decreased from 1975 to 2018 in both males and females. This reduction in mortality rates from CAD over the last decades has been due to a focus on primary prevention (e.g. a reduction in major risk factors, such as smoking cessation and increased physical activity) and improvement in diagnosis and treatment (Nowbar, Gitto, Howard, Francis, & Al-Lamee, 2019).

2.7 Imaging Tools Used to Investigate CAD

2.7.1 Overview of Methods Used to Diagnose CAD

Accurate CAD diagnosis is crucial, as it allows the selection of suitable treatments that can reduce CAD symptoms and the risk of heart attack or death (Cassar et al., 2009). Early diagnosis of CAD is important in preventing death from this disease, since approximately half of heart attacks and sudden deaths occur without previous symptoms (Forrester & Shah, 2020). It is essential to identify patients who would benefit from treatment in order to minimise the mortality rate and health care costs. Furthermore, accurate detection of CAD is important for minimising unnecessary procedures (Liu, Maniadakis, Gray, & Rayner, 2002).

Optimal procedures for diagnostic CAD need to be sensitive, specific and safe. A non-invasive diagnostic procedure is preferable due to the reduction of adverse risk in the testing, and any scan would ideally limit the patient's exposure to ionising radiation.

An electrocardiogram (ECG) monitors the electrical activity in and around the heart and is the most common first-line physical test used to diagnose CAD for every patient who attends primary or secondary care with a suspected heart problem. An ECG is both safe and cheap to administer. ECG data provide evidence of a past myocardial infarction or one that is in progress and can indicate that the patient does not have CAD (Khairuddin, Azir, & Kan, 2017; Lilly &

Braunwald, 2012). However, ECG has only a reported sensitivity of 68% and a specificity of 77% for diagnosing CAD (Cassar et al., 2009).

2.7.2 Common Imaging Modalities

Available imaging techniques (invasive and non-invasive) can either exclude CAD or detect the presence of CAD. There are two main imaging modalities for diagnostic CAD: anatomical imaging, such as magnetic resonance imaging (MRI) and computed tomography (CT), and functional imaging, such as nuclear cardiology (single photon emission computed tomography [SPECT] and positron emission tomography [PET]) and echocardiography (echo). Anatomical imaging concentrates on non-invasively visualising the coronary arteries and assessing their narrowing. Functional imaging assesses the blood flow consequences of a narrowing or blockage in the arteries affected by CAD. The anatomical and functional imaging used for diagnosing CAD are explained in the following sections.

2.7.3 Anatomical Imaging Techniques

Anatomical imaging is used to visualise coronary artery obstruction in patients with known CAD. It detects luminal stenosis but provides few details about the vessel wall or plaque. Anatomical imaging modalities range from invasive procedures, such as angiography (the most commonly used), to non-invasive anatomic modalities, including CT and MRI (Hanson & Bourque, 2019).

2.7.3.1 Angiography

Coronary angiography is an invasive technique defined as the radiographic visualisation of the coronary vessels after the injection of contrast. It is the gold standard for assessing anatomic CAD because of the accuracy of defining the extent of coronary luminal obstruction (Paternò et al., 2019). The angiography procedure involves an X-ray that guides a catheter into the patient's coronary arteries via either the radial artery or the femoral artery. A contrast agent is injected into the coronary arteries, and another X-ray image is collected to visualise the blood vessels and assess any narrowing or blockages (Çimen, Gooya, Grass, & Frangi, 2016; Morrish & Goldstone, 2008). Coronary angiography in the diagnosis of CAD has a sensitivity of 95–99% and a specificity of only 64–83% (Members et al., 2013). Coronary angiography is associated with several possible complications that may involve bleeding or infection at the access site, damage to the coronary vessels, ionising radiation and risks such as renal failure associated with the use of contrast agents (Kern, Sorajja, & Lim, 2015).

2.7.3.2 Magnetic Resonance Imaging (MRI)

Cardiac MRI is a non-invasive procedure that uses a strong magnetic field and radio waves to generate detailed images of the heart structures and associated blood vessels (Nikolaou, Alkadhi, Bamberg, Leschka, & Wintersperger, 2011). MRI is used to assess the function and structure of the cardiovascular system through the injection of a contrast medium known as gadolinium. The gadolinium contrast medium highlights the blood vessels, allowing their structures to be examined and how they are working. It can also assist in providing details related to the tissue blood supply (Saba, 2017). The advantages of MRI include its high spatial resolution and the fact that there is no ionising radiation from the scanning procedure. The contrast utilised in MRI has low toxicity, resulting in few reactions. However, MRI is not suitable for patients who have certain medical devices, such as pacemakers, and the modality is expensive and of limited availability (Jerosch-Herold, Seethamraju, Swingen, Wilke, & Stillman, 2004; D. C. Lee & Klocke, 2006). The sensitivity and specificity of cardiac MRI in identifying obstructive cardiac disease are 89% and 76.2%, respectively (Laspas et al., 2020).

2.7.3.3 Computed Tomography (CT)

Cardiac CT is a non-invasive technique used to assess CAD with a high degree of diagnostic accuracy. It utilises iodine, a contrast agent, and CT scanning to assess whether the coronary arteries have been obstructed or narrowed. An intravenous cannula is required for the contrast injection (Chaturvedi, Oppenheimer, Rajiah, Kaproth-Joslin, & Chaturvedi, 2017). The sensitivity and specificity of CT in the diagnosis of CAD are 96% and 79%, respectively (Moss, Williams, Newby, & Nicol, 2017). Drawbacks of cardiac CT include increased radiation dose, motion artefacts, allergic contrast reaction and contrast-induced renal toxicity (Maurovich-Horvat, Ferencik, Voros, Merkely, & Hoffmann, 2014; Polonsky et al., 2010).

2.7.4 Functional Imaging Techniques

The essential aim of functional imaging is to detect the existence and degree of myocardial ischaemia of CAD. It includes several techniques, such as echo, PET and SPECT/CT. However, functional imaging has seen significant growth over the past two decades (Lee, Qutub, Aljizeeri, & Chow, 2013)

2.7.4.1 Echocardiography (Echo)

An echocardiogram (echo) uses a transducer to send and receive ultrasound waves to visualise the heart's anatomy. Echo provides a quick and easy assessment of heart structures and wall motion. Areas of abnormally reduced motion can indicate CAD; for instance, reduced

movement in parts of the heart wall may have been caused by myocardial infarction or reduced oxygen supply (Esmaeilzadeh, Parsaee, & Maleki, 2013; Leischik et al., 2016). The sensitivity and specificity of echo in the diagnosis of CAD are 81% and 84%, respectively (Sicari & Cortigiani, 2017). Echo is commonly available, easy to use, cheap and uses non-ionising radiation, and the devices can be brought to a patient's bedside (Votavová, Linhartová, Kořínek, Marek, & Linhart, 2015). However, the operator's skills can impact the effectiveness of echo as a diagnostic tool (Esmaeilzadeh et al., 2013; Leischik et al., 2016).

2.7.4.2 Positron Emission Tomography/Computed Tomography (PET/CT)

PET/CT is one of two general categories of nuclear medicine imaging (PET/CT and SPECT/CT) involving radionuclides that decay with gamma-ray emission. PET is a technique that measures the metabolic activity of the cells of body tissues. The concept of PET is that, when the patient is intravenously injected with a small amount of a radiopharmaceutical, radiation is emitted and then registered by external detectors that are positioned in various directions. The PET radiopharmaceutical emits positrons (positively charged electrons), which go on to cause electron annihilation, the creation of two gamma photons emitted in opposite directions at the rest mass of the positron/electron (511 keV(Kaufmann & Camici, 2005). The signal recorded by an array of detectors around the body comes from the gamma rays emitted when the positrons collide with the electrons in the tissue (Zipes, Libby, Bonow, Mann, & Tomaselli, 2018). The benefits of a PET scanner include its ability to measure absolute radionuclide uptake, its assessment of metabolism (e.g. oxygen and glucose) and the fact that its resolution is better than a SPECT scanner (Driessen, Raijmakers, Stuijfzand, & Knaapen, 2017). A recent study evaluated the accuracy of PET imaging in diagnosing CAD and reported sensitivity and specificity of 91% and 90%, respectively (Schindler et al., 2020). The limitations of a PET scanner are its cost, higher radiation levels and the need for a cyclotron to produce radiotracers that have short half-lives (Blake, Johnson, & VanMeter, 2003). Furthermore, the availability of PET scanners is low compared with SPECT.

2.7.4.3 Single Photon Emission Computed Tomography/Computed Tomography (SPECT/CT)

SPECT/CT is a minimally invasive technique that uses a small amount of radiopharmaceutical injected intravenously to produce images that show the blood flow to the myocardium. There are two commercially available radiopharmaceuticals for use with myocardial perfusion imaging (MPI) scans. ^{99m}Tc-labelled sestamibi and ^{99m}Tc-labelled tetrofosmin are the most commonly used in clinical practice to evaluate pathology within the cardiac. Both

radiopharmaceuticals are cleared rapidly from the blood, and their myocardial uptake is similar (Borges-Neto et al., 2000). This technique uses a radiation-detecting camera to visualise the radiopharmaceutical distribution administered to the patient and a CT scanner to determine the exact anatomic location of the region and to compensate for photon attenuation. SPECT/CT can image myocardial perfusion, ventricular function and viability with a single test. Dynamic exercise is the stress technique of choice for assessing patients with suspected or known CAD, provided that the patient can exercise to a sufficient workload (e.g. at least 85% of the maximum expected heart rate). A radiopharmaceutical should be injected as close to peak exercise as possible. After the radiopharmaceutical injection, patients should be encouraged to exercise for a minimum of one minute. However, when the patient cannot exercise adequately, pharmacological stress is a perfect alternative to dynamic exercise. In such tests, pharmacologic agents can be used to mimic the heart's response to physical stress (i.e. exercise; (Anagnostopoulos et al., 2004). Coronary artery stenoses can be evaluated by detecting the presence of perfusion or wall motion abnormalities (Al Badarin & Malhotra, 2019). In this technique, the patient is injected intravenously with a radiopharmaceutical that is taken up in the cardiac muscle to estimate regional coronary blood flow, usually at rest and stress conditions (Schuijf et al., 2005). Gamma photons leave the heart in all directions, and as they move through the body toward the gamma camera, they often interact with soft tissues. Various SPECT planar images are obtained of the patient from different angles, and the data from this set of two-dimensional (2-D) images are utilised to reconstruct a three-dimensional (3-D) image tomographically.

In SPECT imaging, photons are emitted out of the patient and detected by gamma cameras. As photons traverse through the body, they undergo attenuation. If the source was perfectly at the centre of a homogenous body, and they all underwent equal attenuation there would be no need for attenuation correction. However, the human body is not homogenous in tissue densities and emissions do not originate from a single source. So, for correction of the attenuation of the photons, CT is used. CT data is a representation of the attenuation of the photons as they go through tissue; it is an attenuation map. By combining accurate information from the emission and transmission approaches, we can get attenuation corrected images. Clearly, accurate CT attenuation mapping is essential.

Various studies have evaluated the accuracy of SPECT imaging and reported a sensitivity and specificity of 87−89% and 73−75%, respectively. Israel et al. (2019) showed that SPECT/CT MPI with attenuation correction (AC) has a sensitivity of 89 % compared to 87 % without AC and a specificity of 81 % compared to 73 % without AC (Israel et al., 2019).. SPECT/CT's

advantages over PET/CT include familiarity among providers, wide availability, lower dosimetry and enhanced image quality (Bateman, 2012). The disadvantages of this modality are the long imaging time, the risk of misregistration of artefacts due to patient movement between SPECT acquisitions and CT and the ionisation radiation emitted by the radiopharmaceutical (Bybel et al., 2008).

Although SPECT and PET both use a tracer agent and detect gamma rays, the gamma radiation emitted by the tracer material in SPECT is directly measured, while the positrons emitted by the PET tracer are annihilated with electrons, which leads to the emission of two gamma photons that travel in opposite directions. To enhance accuracy, these gamma photons are detected in coincidence to indicate a positron emission or an annihilation event. SPECT scans are cheaper than PET scans, and the SPECT isotopes (^{99m}Tc or ^{201}TI) are easier to acquire and have a longer half-life to decay. In addition, the availability of a SPECT gamma camera compared to that of PET makes SPECT more widely used for functional CAD diagnosis (Dorbala et al., 2018b). Therefore, this is one of the strengths of SPECT /CT that allows it to be widely used as a functional imaging modality for CAD and is discussed in more detail in the following section.

2.8 Principles of Cardiac SPECT/CT Imaging

2.8.1 General Principle of SPECT/CT

Current trends indicate a significant increase in SPECT/CT equipment. For example, recent European data show a 22% increase in SPECT/CT scanners installed in France from 2015 to 2018, with comparable data available from the United Kingdom and Germany(Van den Wyngaert, Elvas, De Schepper, Kennedy, & Israel, 2020).

Different types of gamma cameras are utilised for various imaging applications. They may be single, dual, or triple-headed, movable or fixed (Mariani et al., 2010). The head of the single-headed camera is a single crystal detector connected to a bank of PMTs and positioned on a gantry, with the entire system referred to as a head. The gantry enables the camera to move across different parts of the body, and some devices additionally incorporate a moving bed to enable imaging of the whole-body volume. The most common configuration is the dual-head camera, which consists of two heads that may be simultaneously positioned in different areas across the body, enabling two images to be acquired simultaneously(Dorbala et al., 2018a).

While fixed gamma cameras are commonly used in nuclear medicine, special mobile cameras have been developed for imaging smaller organs, such as the thyroid, or patients who cannot move easily. These cameras typically utilise Cadmium Zinc Telluride (CZT) detectors with

smaller sizes (Engbers et al., 2017). For the imaging of individuals with suspected coronary artery disease, cardiology-dedicated gamma cameras have been developed. These smaller-sized gamma cameras utilise semiconductor detectors made of CZT crystals linked with Cesium Iodide Thallium [CsI(T1)]. Advanced iterative reconstruction techniques and novel collimator designs enable these cameras to acquire images more efficiently, resulting in enhanced image quality(Błaszczyk, Adamczewski, & Płachcińska, 2021). In contrast to conventional cameras, these newly developed cameras for imaging the cardiac; additionally, they utilise a larger proportion of the available detector area to record a higher count sensitivity. Multiple detectors performing simultaneous imaging allow these cameras to acquire images more quickly, and they typically produce 5 to 10 times higher count sensitivity, allowing a lower patient dose (Van den Wyngaert et al., 2020).

SPECT/CT is a hybrid imaging technique that integrates two modalities (CT and SPECT), offering anatomical and functional images in one scanner, as the combination of coregistered anatomical and functional images improves sensitivity and specificity(Mariani et al., 2010). Direct ways of integrating structural and functional information were conceived and prototyped during the early development of emission and transmission computed tomography. Researchers began developing approaches in the late 1980s to integrate radionuclide emission imaging with x-ray transmission imaging in a single system (Seo, Mari, & Hasegawa, 2008). The GE MilleniumTM hybrid SPECT/CT camera equipped with the HawkEyeTM single-slice CT was the first commercial SPECT/CT combination constructed as a single unit (Ljungberg & Pretorius, 2018). The CT generated images with a slice thickness of 1cm and a 256×256 matrix size with a spatial resolution of approximately 3.5 mm. Because of the poor resolution, the unit was not regarded as a diagnostic CT. It took about 10 minutes to complete an acquisition that matched the field of view (FOV) for the SPECT cameras, increasing the risk of motion artifacts. However, current SPECT/CT systems, offered by different manufactures, all offer high-resolution diagnostic CT units as part of their SPECT/ CT systems. (Ljungberg & Pretorius, 2018). In the SPECT technique, a patient is given an intravenous injection with a radiotracer that emits gamma photons. The number of photons measured is proportional to the flow of blood in the cardiac tissue (Beller & Heede, 2011). An external rotating camera is used to detect gamma photons (Cherry et al., 2012; Vlajković & Matović, 2012). The external rotating camera comprises a rotating gantry and at least one mounted gamma camera head that acquires 2-D projection images from equally distanced angular intervals around the patient's body. 2-D images are created from images taken typically every 3–6º (Gibbons et al., 2009). A complete 360º rotation is usually employed to perform an optimal reconstruction. A tomographic

reconstruction algorithm is applied to the projections via pre-defined software to create a 3-D data set. Similar to CT, PET or MRI technology, the data set can be manipulated to allow visualisation of thin slices along the viewer's preferred axis of the body (i.e. axial, coronal, or sagittal; Germano et al., 2013). Image acquisition can be accelerated with the use of a multiheaded camera. For example, a dual-headed camera or triple-headed camera can be utilised, with the heads placed 180º or 120º apart, respectively, allowing the simultaneous acquisition of two or three projections (Germano et al., 2013).

The material of the SPECT detector has been developed. Digital solid-state SPECT detector technology has become commercially available in recent years. Cadmium-zinc-telluride (CZT) detectors provide high count sensitivity, system resolution, and energy resolution, allowing significant reductions in administered activities or acquisition time (Ljungberg & Pretorius, 2018). However, NaI(Tl) is a scintillation material that has been in use for a long time, is commonly available and inexpensive, and is still the most often used detector material in SPECT systems (Duan et al., 2022). The primary characteristic of scintillators is that the photon energy absorbed is transformed into visible light proportionally to the energy deposited. The light is detected by photomultiplier tubes (PMTs) and converted to electrons at the cathode surface of the PMTs. Furthermore, many PMTs are required to determine the location of the interaction in the crystal; therefore, the scintillation camera head is quite large and requires sophisticated tuning methods to ensure that all PMTs provide identical signal amplitudes for the same input energy (Błaszczyk et al., 2021). Furthermore, commercial SPECT systems using cadmium-zinc-telluride (CZT) have recently been introduced. CZT is a solid-state detector material with a density of 5.78 g cm^3 that generates signals from the accumulation of induced charge caused by photoelectric interactions or Compton scattering. Individual anodes collect the induced charges because a high voltage is applied between the cathode and the pixelated anodes. Therefore, each anode functions as an individual detector (Van den Wyngaert et al., 2020). The main advantage of CZT is increasing the overall system sensitivity significantly. The improvement in sensitivity can be utilised to minimise the acquisition time of a given administered activity, and the total effective dose could be reduced by decreasing the administered activity (Oddstig et al., 2013).

Hybrid technology has advantages and limitations. One of the main advantages of hybrid technology is that it provides accurate anatomic localisation of an identified abnormality; nuclear medicine examination reflects the disease process's pathophysiologic status. This leads to improved diagnostic accuracy and the ability to identify abnormalities in organs. However, hybrid technology has some limitations: equipment cost is high, and additional items are

required, such as lead shielding and increased room space. In addition, misregistration can occur between two scanners due to patient movement. This misregistration impacts anatomic localisation and creates an incorrect attenuation map, producing defects in AC images (Bybel et al., 2008).

Due to advancements in physics, engineering, and radiopharmaceuticals, the SPECT/CT system has developed over the past two decades as a feature-rich and mature technology suited for clinical usage (Van den Wyngaert et al., 2020). However, the appropriate use of SPECT/CT in the clinical setting must take into account a number of factors, such as the availability of different radionuclides and the need to image one or more body regions using optimised acquisition modes.

2.8.2 Interactions of Photons with Matter

Two general forms of radiation are produced in the radioactive decay process: charged particles, such as α and β particles, and photons, such as γ rays and x rays (Fermvik, 2011). The energy in both forms of radiation transfers its energy to matter through contact due to ionisation and atoms and through the excitation of molecules. In nuclear medicine, there are four interactions between photons and matter; only three kinds of these interactions play a role in SPECT: photoelectric absorption, Compton scattering and Rayleigh scattering.

2.8.2.1 Photoelectric Absorption

Photoelectric absorption is a type of atomic absorption in which an atom absorbs the energy of an incident photon entirely, leading to the disappearance of the photon and the ejection of the orbital electron from the atom. The process of an ejected photon is called a photoelectron. When the photoelectron is ejected from the shell, it receives kinetic energy, which is equal to the difference between the electron shell binding energy and the incident photon energy (Cherry, Sorenson, & Phelps, 2012; Sharp, Gemmell, Murray, & Sharp, 2005)), as shown in Figure 3.
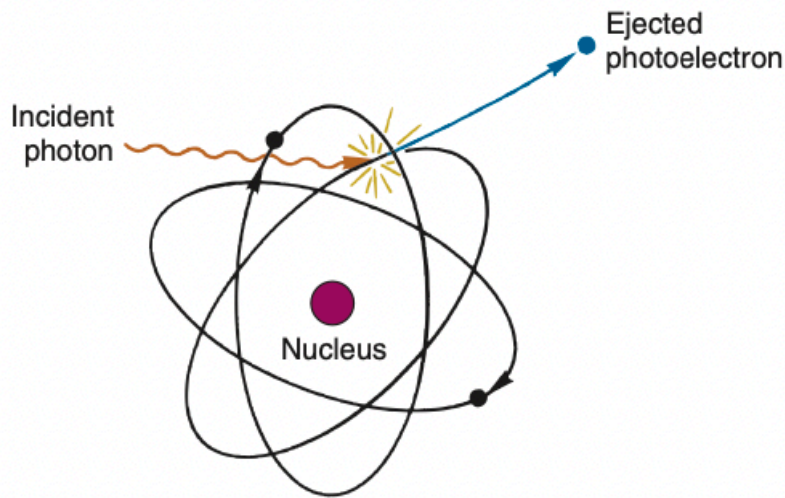
Figure 3: Photoelectric absorption interaction (Cherry et al., 2012).

The kinetic energy of the photoelectron can be described as follows:

$E_{pe} = E_0 - K_B,$

where, E_{pe} is the ejected electron kinetic energy, E_0 is the energy of an incident photon and K_B is the binding energy to the electron shell. The likelihood of photoelectric absorption is based on the atomic number of the material, and the probability increases in proportion to Z^3, where Z is the atomic number of the atom (Cherry et al., 2012). Therefore, the probability of photoelectric absorption increases with materials that have lower incident photon energies and higher atomic numbers.

2.8.2.2 Compton Scattering

Compton scattering interaction refers to the collision between a photon and an outershell orbital electron with low binding energy (Jones, Hogg, & Seeram, 2013). The Compton scattering effect does not lead to the disappearance of the incident photon; instead, part of its energy is transferred to the electron and deflected at an angle of scattering (Cherry et al., 2012), as shown in figure 4.
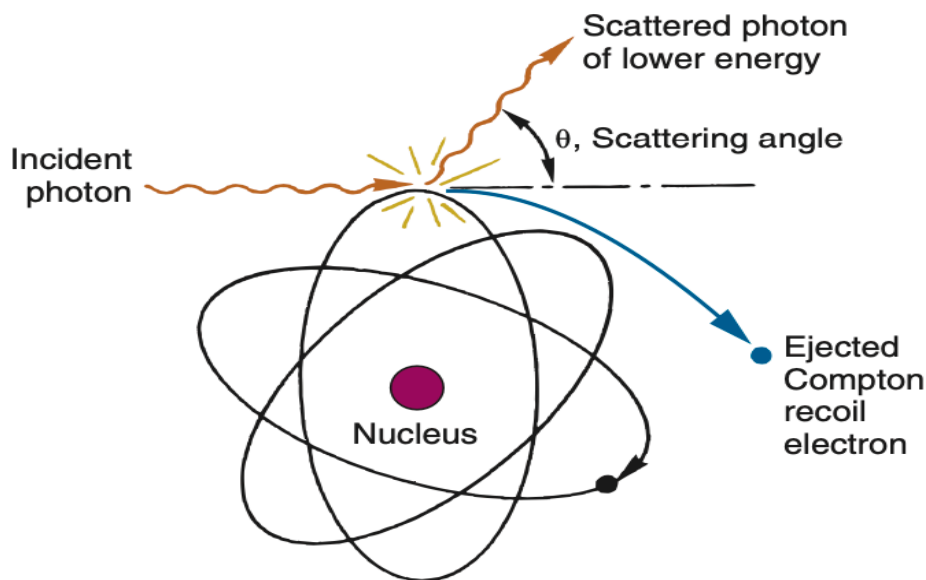
Figure 4: Compton scattering interaction (Cherry et al., 2012)

In this interaction, some photon energy is lost, and the remaining photon, termed a "scattered photon," has lower energy and travels in random directions. When the photon loses a small amount of energy in the interaction, a small scattering angle occurs, whereas when it loses greater energy, it results in a larger scatter angle (Jones et al., 2013). Maximum energy loss happens when the photons are totally backscattered and emerge at 180° to their initial direction (Cherry et al., 2012). The likelihood of Compton scatters increases in the case of photons with high energies and in low atomic number materials, such as human tissue (Sharp et al., 2005).

2.8.2.3 Rayleigh Scattering

Rayleigh scattering occurs when the incident photon does not have enough energy to liberate the electron from its bound state. In this interaction, the incident photon is scattered by bound atomic electrons. This interaction causes neither atomic excitation nor ionisation. However, the incident photon changes its direction. At the end of the interaction, the bound electrons regain their original state (Cherry et al., 2012; Sharp et al., 2005).

2.9 The Gamma Camera System

The gamma camera, also known as the Anger camera (Cherry et al., 2012), is an instrument mounted on a gantry containing a radiation detector and a series of apertures or collimators. A simple gamma camera schematic is illustrated in Figure 5.

As shown in Figure *5*, photons emit in all orientations and exit the body to be registered by a gamma camera. Photons transmitted from a patient are collimated by lead plates with parallel holes (called collimators), which allow a small percentage of these photons to hit a scintillation crystal detector in the gamma camera. The photons that reach the detector are only those photons that are not absorbed by the material of the collimator (Van Audenhaege et al., 2015). The function of scintillation crystals is to convert gamma photons into light photons. Then, the light photons are converted into electrical signals by photomultiplier tubes (PMTs; (Hasan et al., 2017). Each scintillation event creates a large number of light photons, which are normally detected by more than one PMT. Each scintillation event is localised using electronic circuits that incorporate position logic, known as Anger logic (Jones et al., 2013). Scintillation events are then illustrated as a 2-D array of counts that are converted into a 2-D image using a table of colours.
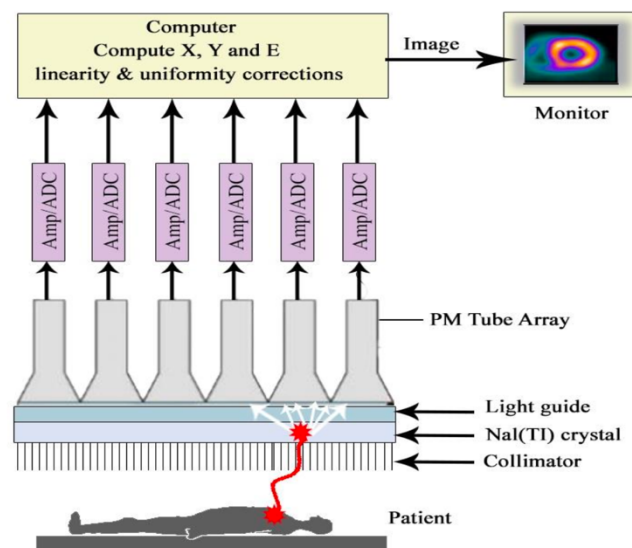
Figure 5: Gamma camera scheme (Cherry et al., 2012).

2.9.1 Types of Collimators

Collimators can control the noise, resolution and sensitivity of the functional SPECT image (Islamian, Azazrm, Mahmoudian, & Gharapapagh, 2015). They are usually classified as pinhole, parallel hole, converging and diverging collimators.

The commonly used collimator in clinical imaging of the heart is known as the parallel hole collimator. It consists of a plate of dense material that has holes parallel to the line of incoming photons and perpendicular to the scintillation crystal. Its function is to allow only photons to travel along a path perpendicular to the detector head and interact with the crystal. The walls between collimator holes are called septa, and they absorb photons emitted by unwanted sources. Only those photons that are not absorbed by the collimator are detected at the detector. When the septa length increases, the resolution is high, but the sensitivity is low because it decreases the penetrated photons (Van Audenhaege et al., 2015; Weinmann, Hruska, & O'Connor, 2009).

2.10 Image Correction Methods

2.10.1 Attenuation and Its Correction

As previously mentioned, when photons pass through any material, they interact with it to some degree. There are two fundamental interaction mechanisms for those photons with energies that fall into the range commonly identified in the field of nuclear medicine – that is, in the keV range. First, the photoelectric absorption and, second, the photon could demonstrate a scattering interaction (i.e. Compton scattering; (Bushberg & Boone, 2011). Organs and tissues of a patient may absorb gamma rays, scattering them out of the field of view (FOV) and causing the number of photons that interact with the detector to decrease compared to the total number of photons emitted. This can lead to the count values of pixels in the reconstructed images not being proportional to the pixel count values in the true radiopharmaceutical distribution (Miles, Cullom, & Case, 1999).

When the photons are emitted and travel through the medium or organ, attenuation might be generated by tissues, such as in the lungs, ribs, breasts and diaphragm, in different planar projections. Such attenuations impact the total detector efficiency and can create variation in the SPECT images, demonstrating the absolute and relative uptake of the radiotracer. This can ultimately lead to attenuation artefacts. When these artefacts are misidentified or not identified, they might cause misinterpretation of MPI, leading to an inaccurate diagnosis. Therefore, addressing attenuation problems by using AC approaches is essential for avoiding diagnostic

inaccuracy in MPI SPECT images, prognoses and treatment plans (Bai et al., 2010; Cherry, Sorenson, Phelps, & Methé, 2004).

AC can be defined as an approach that removes attenuation artefacts from SPECT images. When attempting to correct for attenuation effects, attenuation maps need to be gathered for all objects undergoing imaging. This ensures that the attenuation experienced by the photons emitted at a location and detected by the spatially distributed detectors can be calculated.

AC approaches may be categorised as either constant attenuation or transmission source (Bailey & Humm, 2014). Constant attenuation assumes a known body outline and a known attenuation coefficient; it can then be assigned to all points within the outline. It may only be applied in the abdominal or brain regions because their tissues are uniform (Ogawa, 2004; PASSAU, 2011) . The body outline can be determined from emission data in regions with uniform attenuation, such as the brain and abdomen. The spatial distribution of the linear attenuation coefficient value can then be assigned to the defined region based on the type of tissue to generate the corresponding attenuation map (Tadesse, Geramifar, Tegaw, & Ay, 2019). Because it is typically difficult to define the patient's body outline using only emission data without transmission data. Consequently, constant attenuation techniques have had limited clinical application. However, when applied to heterogeneous regions of the body, uniform attenuation compensation can result in significant inaccuracies and should be utilised for homogeneous regions such as the brain and abdomen, which are primarily composed of soft tissue (Dewaraja et al., 2013). This is not the case for cardiac scans because the heart is surrounded by tissue with varying attenuation coefficients. To address this issue, an attenuation map for cardiac scans is obtained with a radionuclide transmission source or a CT scanner. The CT approach uses the X-ray tube as a source of radiation, which accordingly results in the commonly referenced hybrid SPECT/CT (Garcia, 2007). Importantly, CT has replaced radionuclide transmission imaging, with a focus on non-uniform AC. AC techniques have improved the quality of the image and the sensitivity and specificity of MPI (Tantawy, Abdelhafez, Helal, Kany, & Saad, 2020). Therefore, the European Association of Nuclear Medicine (EANM) has recommended using AC for cardiac SPECT scans (Camoni, Santos, Attard, Mada, Pietrzak, Rac, Rep, Terwinghe, & Fragoso Costa, 2020) .

2.10.2 CT Technology

The CT scanner was invented by two independent scientists, Allan Macleod Cormack from South Africa and Godfrey Newbold Hounsfield from the United Kingdom. In 1971, the first

CT scanner was used to diagnose a patient who had a suspected brain tumour. The first marketed commercial CT scanner, the EMI CT 1000, was produced in 1973. The images from this scanner took 20 seconds to generate, with an image quality of 320 x 320 pixels. Modern CT scanners can generate images in a hundred milliseconds, with excellent resolution (e.g. 2048 x 2048 pixels; Ciernak, 2011).

CT technology generates data depending on the differences in the attenuation levels of the scanned area (Rodriguez-Granillo et al., 2015). It creates a volume of data that can be used to demonstrate various structures based on tissue thickness and composition. In CT, X-ray beam attenuation depends on the tissue thickness and composition (physical density and atomic number), with the beam traversing a path between the tube and detector (Kalisz et al., 2016). The effect of attenuation on the overall quality of an image is noteworthy because tissue density and thickness differ from one part of the patient's body to another. In CT images, each pixel represents the attenuation coefficient of the X-ray beam of the various tissue densities; this attenuation value is called the CT number, or Hounsfield unit (HU).

2.10.2.1: CT numbers and Hounsfield Units:
In Computed Tomography (CT), x-ray beam attenuation depends on both attenuation coefficient and thickness of the tissue. The process of image reconstruction generates a 3D matrix of CT numbers, representing the attenuation that arises at the equivalent points in the patient. CT numbers are the standard values that are used in the calculation of X-ray absorption and attenuation in materials. These CT numbers are then calibrated to the corresponding CT number of water for each CT scanner, resulting in the data being presented in Hounsfield Units (HU)(Mamourian, 2013). The linear attenuation coefficient of water is used as a reference to measure CT numbers, because it does not change based on the energy of the X-ray. Each voxel of the image is allocated a Hounsfield unit (HU), representing the electron density of the tissue or standardised attenuation coefficient (Lamba et al., 2014). If the attenuation coefficient of the tissue is less than the water attenuation coefficient, where the HU of water is 0, the HU is negative; if the attenuation coefficient of the tissue is more than the attenuation coefficient of water the HU will be positive. For example, fat has a negative HU owing to its low attenuation coefficient, whereas dense tissues such as bone have a high positive HU (Kalender, 2011; Szczepura et al., 2017).

$$CT\ number = 1000 \times \frac{(\mu\ tissue - \mu\ water)}{\mu\ water}$$

The attenuation coefficients are fully dependent on the tissue density due to the characteristic x-ray beams that computed tomography uses with heavy filtration and high kilo Volts (KV) (Di, Carli M. F, and Martin J. Lipton,2007). CT numbers can be used to identify certain tissues and abnormalities to support clinical diagnosis (Szczepura et al., 2017). In this application CT numbers are used to correct the emission map for photons attenuation that occur in the patient, this is known as attenuation correction. The transmission map is based on CT numbers to correct the emission map to reduce attenuation artefacts (Patton & Turkington, 2008). Consequently, any inaccuracies in CT numbers could lead to inaccuracies in the corrected emission data. CT numbers can be affected by many factors, such as beam hardening, scatter radiation, reconstruction artefacts, and variations in patient size, shape, and position within the scanner; all of which may cause significant intra- and inter-scanner variabilities of the measured CT numbers(Lamba et al., 2014).

In research encompassing a number of different CT scanners as provided by various manufacturers, with the inclusion of hybrid systems, it was established that HU differences between systems were overall very small, with HU differences found to be less than 5 across all ACR CT Accreditation Phantom structures when there was consistency in the kVp. However, when there was variation in kVp, there was the presence of dependence of HU value on the kVp. Notably, a significant decrease in HU was found to be linked with an increase in kVp for acrylic, bone and polythene regions of the phantom (Cropp *et al.*, 2013). Another work centred on CT numbers' energy dependence, as carried out by Mahmoudi *et al*., established that the scanner response varied in line with the material's atomic number; in other words, low atomic number structures witnessed an increase in HU in line with an increased kVp, whereas those structures recognised as having a high atomic number concluded with the opposite effect. This was witnessed across a clinical range of kVp values spanning 80–130. (Mahmoudi *et al.*, 2016). Importantly, at the present time, there is the use of HU values to stage regional lymph nodes in PET/CT; this is recognised as a highly considered prognostic factor, with the mean HU value of malignant nodes measured at 48±13, whilst benign lymph nodes were found to be 75±18 (Kim *et al.*, 2012). Furthermore, in PET/CT, the HU value was applied in such a way so as to aid estimation of early bone metastases amongst patients with prostate cancer, where the hybrid approach has proven useful in identifying a link between F-18 Choline uptake and the HU value of bone. In this vein, it was established by Beheshti *et al*. that a HU level of more than 825 may be linked with a complete lack of FCH uptake (Beheshti *et al.*, 2010). Importantly, as has been established, there is a need for HU accuracy to be well-considered when choosing imaging parameters. In this regard, it is clear that caution should be ensured

whenever using HU so as to direct patient management. Importantly, a prominent consideration for clinical adopting CT HU values in the estimation of disease and the identification of how to treatment illness is acquisition parameters.

2.10.3 Hybrid Imaging System for Attenuation Correction (SPECT/CT)

Hybrid technology can be defined as integrating anatomical and functional images into one scanner. The system of SPECT modalities with AC adheres to the following basic requirements: 1) an ability to produce attenuation images with high quality (i.e. accuracy), illustrating low noise and no artefacts of respiratory motion, and 2) involves advanced algorithms to reconstruct SPECT images that address non-uniform attenuation and the scattering of photons (Garcheva-Tsacheva, 2012).

"In CT, the term artefact is applied to any systematic discrepancy between the CT numbers in the reconstructed image and the true attenuation coefficients of the object"(Barrett & Keat, 2004, p. 1680). In AC imaging, CT images can produce patient-specific attenuation maps because they include pixel values that are associated with the linear attenuation coefficient (μ) at that point in the patient. This is measured by considering the mean energy of the X-ray photons applied to create the CT image. The calculation of the linear attenuation coefficient is performed at the X-ray energy as opposed to the gamma photon energy. This means that there is a need to identify a calibration curve to ensure that the linear attenuation coefficients obtained from the CT scan are converted to those paralleling the emission photons' energy (Mousa, Kusminarto, & Suparta, 2017). Tissue-equivalent calibration materials allow the CT number to be calculated against the known attenuation coefficient at the photon energy of the radionuclide, as applied in the emission study. Using these approaches, it is possible to utilise CT scans to correct emission images for several different radiopharmaceuticals.

2.10.4 Computed Tomography Attenuation Correction (CTAC)

Several studies have addressed the value of computed tomography attenuation correction (CTAC) in clinical practice. A recent meta-analysis summarised that, by using AC within MPI SPECT/CT, the accuracy of interpreting images to detect CAD is improved or increased compared to using non-attenuated corrected (NAC) images (Huang et al., 2016). A considerable amount of literature has been published on CTAC. These studies have assessed CTAC in MPI SPECT/CT with different analytical procedures. Case et al. (2005) found that specificity is increased when CTAC is applied without compromising sensitivity. Utsunomiya et al. (2005) revealed that CTAC images had higher specificity and accuracy compared to NAC

images within SPECT/CT MPI scans, and variation in diagnostic accuracy was statistically significant (P = 0.03). A statistically significant difference has been found between diagnostic accuracy when comparing corrected (CT-based AC images) and uncorrected images (Utsunomiya, 2005; J. Huang et al., 2016; Huang et al., 2019). Masood et al. (2005), in examining 39 patients with a low likelihood of CAD and 118 patients with subsequent invasive coronary angiography, revealed that CTAC in MPI SPECT/CT consistently improved the overall diagnostic performance of readers with various interpretive approaches and experience(Masood et al., 2005). (Apostolopoulos & Savvopoulos, 2016) showed that CT-based AC of SPECT using a dual-head SPECT/CT scanner enhanced the overall diagnostic accuracy of MPI and is therefore well-suited for routine clinical use.

Mathur et al. (2013) examined 1,383 patients who had stress MPI SPECT/CT imaging. Patient images were reviewed for both CTAC and CT without AC. Without using CTAC, less than half of the patients had a normal diagnosis; however, when applying CTAC, the percentage of patients interpreted as normal increased to 83% (Mathur et al., 2013). Irrespective of some of the arguably adverse findings, it remains clear that AC may prove useful, especially among female patients. Females with suspected or otherwise identified CAD are viewed as a difficult group to diagnose, to some degree, due to significant variability in breast attenuation and generally smaller cardiac volume. Clinically, there is a benefit to using AC with SPECT, as it causes a significant reduction in false positives for both rest-stress studies and stress-only imaging. These false-positive findings are likely frequently due to attenuation artefacts that are estimated to have occurred in 50–78% of studies (Mathur et al., 2013).

Sharma et al. (2012) compared the advantages of using AC images over uncorrected images in terms of specificity. In this study, the stress-rest SPECT MPI patient data (n = 168) were reviewed. Two experienced nuclear cardiologists analysed the SPECT images, and the readers were blinded to the patients' clinical information. The study found that there was an improvement in specificity for both readers when comparing corrected and uncorrected images (Reader 1: 73.9% NAC vs 88.8% AC; Reader 2: 82.6% NAC vs 89.1% AC; (Sharma, Patel, Karunanithi, Maharjan, & Malhotra, 2012). Overall, CTAC can improve the accuracy of CAD diagnoses by compensating for soft-tissue attenuation.

2.10.5 CT Acquisition

The following subsections describe the main CT acquisition parameters that impact image quality and CT HU accuracy.

2.10.5.1 Tube Voltage (kV)

The term "tube voltage" (kVp) refers to an electrical potential difference that is applied across the cathode and anode of the X-ray tube to accelerate electrons (Dowsett, 2013). It is quantified as kilovoltage (kV) and impacts the liberated electron energy from the cathode and, consequently, the X-ray beam's penetrating energy. An increase in kVp increases the X-ray beam energy, improves the penetrative ability of the X-ray beam and decreases the image contrast (Dowsett, 2013; Kaza et al., 2014).

The CT X-ray tube voltage in kV is one of the main parameters affecting CT HU values (Afifi, Abdelrazek, Deiab, Abd El-Hafez, & El-Farrash, 2020). Mahur et al. (2017) analysed the impact of various tube voltages on CT HUs for different tissue substitutes in a phantom study. The study found that changes in kVp settings between different substitutes resulted in no statistically significant variation in the measured CT HUs, although the largest difference in CT HUs was seen in the condition of high-density materials and a CT scan at the lowest kVp. Thus, no significant difference was noted in the CT HUs of various density materials for different kVp values (Mahur et al., 2017). However, Garner et al. (2017) investigated the effect of different tube voltages on CT HUs of the L1 vertebra bone in 191 patients. The study found that the CT HU values of the bone changed with kVp settings and that CT HUs corresponding to the L1 vertebra bone had a statistically significant reduction as the tube voltage increased (Garner, Paturzo, Gaudier, Pickhardt, & Wessell, 2017). In 2021, Saini et al. (2021) analysed the effect of variations in tube voltage on CT HU values of a CIRS phantom that is constructed of proprietary tissue equivalent epoxy materials. The study found that the most significant change in CT number was observed in bone material compared to different CT tube voltages, followed by lung and water equivalent material. A small CT number was noticed in lung equivalent material because the electron density is extremely low, making it more sensitive to imaging noise over variations in tube voltages (Saini, Pandey, Kumar, Singh, & Pasricha, 2021). Mahmoudi et al. 2016, conducted additional research on the energy dependence of CT numbers and found that the variation of CT HU depends on the electron density of the material: structures with a high electron density increase HU with increasing kVp, while structures with a low electron density experience the opposite effect. This occurred between 80 and 130 kVp, which is a clinical kVp value range (Mahmoudi, Jabbari, Aghdasi, & Khalkhali, 2016).

For lower-energy scans, the probability of photoelectric interactions occurring increases, especially in materials with a high atomic number (Z). Increased photoelectric interactions,

therefore, result in increased measured CT HUs for high-Z tissues at low kVp compared to the same tissues at higher energies (Grantham, Li, Zhao, & Klein, 2015).

2.10.5.2 Tube Current (mA)

The term tube current is generally understood to mean amperage, which defines the rate of electron flow through the X-ray tube filament. The flux of photons during the acquisition of the image can be controlled by the tube current (mA) and time (s). Increasing the number of incident photons produced in the X-ray filament allows more photons to be detected by the image receptor; thus, image noise is reduced (Quinn, 2011).

Thompson et al. (2013) evaluated the impact of four different tube currents using on the SPECT/CT scanner on lesion detection performance within an anthropomorphic chest phantom. The study confirms that differences in tube current do not affect tissue attenuation and HU values. Consequently, the linear attenuation coefficients that generate the attenuation map should also be unaffected (Thompson, Hogg, Higham, & Manning, 2013). Preuss et al. (2008) evaluated both the phantom and patient (regions of interest [ROIs] in the heart) images using two different tube current acquisitions (2.5 and 1 mA). Three materials were studied in the phantom, and the study found that the differences between the mean values of the CT number (or HU values) were statistically insignificant (Preuss et al., 2008). Lawson et al. (2016) found no noticeable variation in HU changes between different tube currents. This study used five CT tube currents (8, 12, 15, 40 and 80 mA) to create CTAC maps after a single SPECT acquisition. The study confirmed that variations in tube current did not affect tissue attenuation or HU values. A low-dose CT was found to be adequate for generating AC in quantitative SPECT. The study's findings showed that the quality of the AC map was not affected by increasing mA in the SPECT/CT scanner (Lawson, Avram, Dewaraja, & Ackermann, 2016a). Although the decreased tube current led to an increase in noise, noise was not the main impact on AC. Consequently, based on the manufacturer's instructions, and to minimise radiation exposure, a low tube current, commonly with a relatively high pitch, is recommended to perform AC in MPI (Camoni, Santos, Attard, Mada, Pietrzak, Rac, Rep, Terwinghe, & Costa, 2020). Because it is common practice to smooth CT data before using it for attenuation correction, noise in the data has minimal impact; hence image quality can be optimised, while keeping the patient's effective dose low. Therefore, in this application manufacturers recommend a low tube current (10-20 mA) combined with a relatively high pitch, to reduce radiation exposure. There are many studies confirming that variations in tube current did not

affect tissue attenuation or HU values (Thompson, Hogg, Higham, & Manning, 2013), (Preuss et al., 2008) and (Lawson, Avram, Dewaraja, & Ackermann, 2016).

2.11 SPECT/CT Artefacts

In the case of SPECT/CT, the CT element may be applied for both localisation and AC, with both requiring accurate co-registration between modalities. AC further depends on CT numbers' presenting a suitable and precise attenuation coefficient measurement at a known CT energy (Nichols & Van Tosh, 2019).

Image artefacts can be caused by several factors: the nature of the physics, patient characteristics (soft tissue) and inappropriate use of the scanner. Artefacts may also occur on CT images due to high-density materials, such as metal or silicone breast implants, and truncation. Finally, additional imaging dilemmas, such as misregistration or inaccurate AC, may occur due to patient movement or respiratory movement (Jiang, 2009). Some types of artefacts that can occur are discussed below.

2.11.1 Truncation

Truncation artefacts can be defined as artefacts that occur when the part of the body imaged remains outside the FOV of the detectors because of the patient's body habitus or the specifications of the scanner, such as a small FOV. A truncation artefact may cause an inaccurate AC map and decrease the quality of an image, especially in a large patient (Livieratos, 2015). The accuracy of an AC map might be decreased with small FOV detectors in SPECT imaging due to the severe truncation of the areas that are not being analysed in the emission data. Truncation artefacts are commonly seen in images from dedicated cardiac SPECT scanners due to the typically small FOV. Within the heart imaging procedure, truncation can cause an inaccurate diagnosis of the heart; it may appear as a fixed perfusion defect (infarction) or a reversible perfusion defect (ischaemic) in reconstructed myocardium imaging, and it might lead to unnecessary cardiac catheterisation (Wosnitzer, Gadiraju, & DePuey, 2011). New iterative reconstruction methods and truncation correction are becoming available to compensate for the truncation of the torso of large patients. Artefacts can be minimised using an extended FOV reconstruction of the affected region (Gnanasegaran, Cook, Adamson, & Fogelman, 2009).

2.11.2 Misregistration

Hybrid SPECT/CT image misregistration results in artefact-reduced counts in the anterior and anteroseptal cardiac walls. Tonge et al. (2006) studied 94 patients (64 males, 30 females) who

underwent rest and stress MPI. Misregistration was recognised as significant in more than one-third (35%) of the cases. In those cases where misregistration resulted in heart tissues being corrected by the attenuation coefficient, anterior and apical segment-located artefacts were found to be probable (Tonge et al., 2006). The study Saleki et al. (2019) indicated that using registration correction appears clinically significant for MPI using SPECT/CT, even if only a small misalignment exists (Saleki et al., 2019).

Misregistration artefacts may also be generated because of patient motion. These commonly arise in the form of streaking or shading following reconstruction (Boas & Fleischmann, 2012). In clinical SPECT examinations, the performance of MPI tests is limited by respiratory motion. In MPI studies, motion can result in blurring artefacts, a reduction in image resolution, and image misinterpretation, particularly for regional and global left ventricular (LV) function, and a reduced ability to detect regions with lower tracer uptake. Respiratory gating has been proposed as an applicable method for minimising respiratory motion blur on cardiac SPECT images (Zhang, Sun, Pretorius, King, & Mok, 2020).

Respiratory-induced heart motion influences SPECT acquisition in two ways. First, because SPECT images are obtained for a significantly longer time than CT scans, spatial misalignment between sequentially acquired SPECT and CT images may impact the attenuation correction of the emission data (Polycarpou et al., 2017). Several studies have demonstrated that such misalignment can result in image artefacts and under- or overestimating tracer activity. Due to the SPECT data being averaged over multiple breathing cycles, respiration may also cause image blurring along the direction of motion. This can lead to an incorrect uptake, influencing the perception of regional localization in the cardiac walls. Motion-induced artefacts can cause false-positive findings and may be misinterpreted as ischemia, influencing coronary artery disease diagnosis (Okuda, Nakajima, Kikuchi, Onoguchi, & Hashimoto, 2017).

Patient motion, whether voluntary or involuntary, such as respiration and cardiac motion, throughout the image acquisition process may lead to motion blurring, image degradation, and motion artefacts (Zaidi & Hasegawa, 2006). In order to minimise the motion of a patient and its impacts, nuclear medicine specialists and engineers continue to investigate methods to reduce times of scan as faster imaging processing improve patient comfort and limits the probability of motion patient being detected (Slomka, Hung, Germano, & Berman, 2016). A review of the literature shows that motion of patient has been reported in 10%–26% of clinical SPECT myocardial perfusion studies. The artefacts created by the motion of patient in SPECT

myocardial acquisitions commonly simulate CAD and might be interpreted as ischemia (Wheat & Currie, 2004).

Furthermore, truncated artefacts may occur due to breast tissue being truncated out of the FOV. Consequently, the attenuation correction map may be inaccurate, and the image quality has decreased (Farrell, Pinson, & Dennett, 2021). Such artefacts can appear as a fixed perfusion defect or a reversible perfusion defect (Pirayesh, 2021). Truncation artefacts can be reduced using an extended FOV reconstruction of the affected region. To avoid truncation artefacts the field of view (FOV) of the protocol for AC should be the maximum diameter of the scanner.

2.11.3 Beam-Hardening Artefacts

Beam hardening occurs whenever poly-energetic X-ray beams travel through a dense medium. In a dense medium, photons with high energy are transmitted, while photons with low energy are absorbed, causing increases in the mean energy of the beam. Thus, the passage of the beam through the tissue causes a shift of the beam spectrum towards higher energy. Consequently, the number of photons that hit the detector of an X-ray is not accurately linearly correlated to the penetrated material thickness. Photon attenuation is increased with materials with a high atomic number, such as bone, iodine and implants, including some types of breast implants (silicone breast implants) (Boas & Fleischmann, 2012).

This effect is known to cause two different types of artefacts, namely cupping artefacts in the form of dark bands, and streaks between dense objects in the image. The presence of a metal object in the scan field can result in significant streaking artefacts, which arise because of a metal density extending beyond the normal range. Streak artefacts in CT images can cause attenuation profiles to be incomplete. Consequently, Algorithms are used to reduce artefacts arising from the presence of metallic implants (Schulze et al., 2011). Beam-hardening artefacts in a SPECT/CT cardiac scan may impact the CT number accuracy and, hence, impact the AC map.

2.12 Feminising Breast Surgery

Breast augmentation and reconstruction mammoplasty have been performed for decades for cosmetic improvement or breast volume and symmetry restoration. According to the American Society for Aesthetic Plastic Surgery, in the United States in 2013, breast augmentation was the second most common cosmetic surgery procedure (Govrin-Yehudain, Dvir, Preise, Govrin-Yehudain, & Govreen-Segal, 2015). In the United States, around 5% of the female population has breast implants; approximately 450,000 breast implants are done annually, while around 35 million females have breast implants worldwide (Ionescu, Vibert, Amé, & Mathelin, 2021).

In 2014, in the UK, breast augmentation was the leading cosmetic procedure performed (Govrin-Yehudain et al., 2015). According to the (Breast and Cosmetic Implant Registry (BCIR), 2021,October 06), in 2020, 10,500 patients in the UK have breast implants.

Transgender persons are estimated to represent 0.4% to 1.3% of people worldwide and a third of transgender patients underwent gender-affirming surgery (GAS). It is estimated that as many as 50–70% of transgender patients seek "top surgery"; thus, the surgical need of this patient population bears epidemiologic significance (Bekeny, Zolper, Fan, & Del Corral, 2020). There is an estimated slightly higher representation of transfeminine individuals, with 6.8 per 100,000, compared to transmasculine individuals, with 2.6 per 100,000 people (Arcelus et al., 2015). Male-to-female transsexuals (trans women) typically take anti-androgen therapy together with oral or transdermal estrogens to induce feminisation. Transwomen can be treated with cross-sex hormones to alleviate suffering and induce desirable physical changes. Transwomen are treated with antiandrogens and estrogens. This treatment causes physical changes such as breast development, decreased sperm production and changes in body hair and body composition, all of which contribute to feminisation.(Wierckx, Gooren, & T'Sjoen, 2014). Breast development is a crucial feature of feminisation and consequently important to transwomen. According to the Endocrine Society's Clinical Practice Guidelines, breast development begins three to six months after starting cross-sex hormone treatment (CHT). After 2 to 3 years of CHT, the maximal effect may be predicted (de Blok et al., 2018). Furthermore, breast size may seem smaller than the actual objectively measured volume due to anatomical differences in the male chest compared with the female chest. Therefore, 60% to 70% of transwomen want further breast augmentation in addition to CHT (Kanhai, Hage, Asscheman, & Mulder, 1999). A more recent study provides evidence that transwomen who have received breast augmentation have shown improvements in breast satisfaction, psychological and sexual well-being, demonstrating the importance of this treatment from a medical perspective (Miller, Wilson, Massie, Morrison, & Satterwhite, 2019).

There are significant differences between the chests of men and women. There are variances in the quantity of glandular tissue; in addition to differences in the quantity of glandular tissue, men have a larger breast base diameter and a shorter distance from the nip to the inframammary fold (IMF) , thus, most patients have hormone therapy before breast augmentation.(Miller et al., 2019).

Furthermore, there is evidence that transgender women receiving hormonal therapy have an increased risk of cardiac disease. Asscheman and colleagues presented that the risk for cardiac

mortality is increased in transgender women receiving long-term CHT (Asscheman, Giltay, Megens, van Trotsenburg, & Gooren, 2011). Current research suggests that anti-androgen and estrogen administration may significantly influence the cardiovascular health of trans women. Both anti-androgens and estrogens raise the risk of venous thrombosis or pulmonary embolism, and recent studies found that trans women have a greater cardiovascular mortality rate than the normal population (Streed Jr et al., 2017). Clinicians must regularly monitor transgender women with an increased cardiovascular risk who are receiving CHT, regardless of the use duration of CHT. Reducing cardiovascular risk factors (such as hypertension, diabetes, and cigarette use) is essential for preventing cardiovascular disease in transgender populations (Streed Jr et al., 2017).

2.13 Breast Reconstruction surgery

The objective of breast reconstruction surgery is to replace the excised breast tissue with something comparable in size, shape, and texture that can establish symmetry with the contralateral breast or function as a substitute for that lost in bilateral mastectomies (Ahmed, Snelling, Bains, & Whitworth, 2005). The available kinds of surgical reconstruction include implant-based reconstruction and autologous-based reconstruction.

Autologous breast reconstruction can be defined as using the patient's own tissue to rebuild the breast mound. The most common donor site for autologous is the abdomen because a sufficient quantity of tissue is often available, and its skin colour and consistency are similar to breast tissue. In addition, for large pendulous breasts, abdominal tissue can be readily reshaped to match the contralateral breast shape(Schmauss, Machens, & Harder, 2016) . In 1895 Vincent Czerny attempted to reconstruct a breast using autologous tissue for the first time. The researcher used a lipoma from the patient's lumbar area for reconstruction. The researcher discovered that transplanting tissue from one region of the body to a place of defect is possible, and the result is permanent (Champaneria, Wong, Hill, & Gupta, 2012). However, breast reconstruction using the patient's own tissue is inappropriate for every patient (Jeevan, 2020). Although autologous breast reconstruction has been determined to be more cost-effective than implant-based breast reconstruction, not all patients are optimal for autologous reconstruction due to body habitus or personal preference (Miseré et al., 2021).

Although the frequency of procedures is now declining, autologous reconstruction has some advantages, such as a more natural appearance, less revision surgery and avoiding implant-associated complications. However, it also has disadvantages such as longer operation and recovery time, more extended hospital stay, donor site morbidity and muscle weakness (Sawyer, Franke, Scaife, Sommer, & Neumeister, 2022).

2.14 Breast fillers

A breast augmentation without invasive surgery might be an appropriate solution for reconstructive or cosmetic purposes (Pienaar, McWilliams, Wilding, & Perera, 2011). Due to this, several breast augmentation fillers materials for less invasive procedures have been developed. For several decades, breast augmentation with different injectable materials, including paraffin, mineral oil, liquid silicone, and polyacrylamide hydrogel, has been performed. However, all of these fillers have resulted in severe consequences, including infection, unexpected migration, nodule formation, and pain. Due to the ease of usage, numerous local clinics worldwide continue to use filler materials for breast augmentation, despite the fact that some nations have banned their use. Hydrophilic gel and hyaluronic acid are the most often utilised fillers (Park, Park, & Chang, 2021).

A hydrophilic gel called Aquafilling comprises 98% sodium chloride solution and 2% polyimide. It was created in the Czech Republic for facial contouring in 2005 (Ozcan, Ulus, & Kucukcelebi, 2019). In addition to Aquafilling, many comparable products have been commercialised under the names Los Deline and Aqualift. Shin et al. 2015, reported using Aquafilling/Los Deline injections to address modest breast deformity following silicone implant breast augmentation (Shin, Suh, & Yang, 2015). However, its safety remains controversial. Complications, including breast pain, gel migration, inflammation, infection, and nodular lesions, have been reported (Son, Ko, Jung, Koh, & Park, 2018). The Korean Academic Society of Aesthetic and Reconstructive Breast Surgery revealed in 2016 that the copolyimide in Aquafilling/Los Deline is poly (acrylamide-co-N, N'-methylene-bisacrylamide), indicating it has the same composition as polyacrylamide gel (PAAG) fillers, which have been found to produce severe adverse effects when used for breast augmentation such as deformity, infection, and gel migration, inability to breastfeed (Roh, 2016). Furthermore, Unokovych et al. described 45 Ukrainian women who had surgery to treat polyacrylamide gel (PAAG) complications, such as pain, breast hardness and deformity, between 1998 and 2009. The average time between injection and occurrence of the complications was 6.1 years (Unukovych et al., 2012).

Hyaluronic acid fillers, called Macrolane, are a NASHA-based (non-animal stabilised hyaluronic acid) medical implant that has been studied for breast and buttock augmentation. It plays a role in delivering adipocyte precursor cells and supports adipose tissue formation (von Heimburg, Zachariah, Low, & Pallua, 2001). Hyaluronic acid provides several advantages, including being non-invasive, reversible, and having rapid outcomes. High crosslinking is a feature of hyaluronic acid filler, which increases its duration in tissues prior to absorption. As the product degrades, the remaining hyaluronic acid binds additional water to keep the total

volume constant (Park et al., 2021). Due to these properties, the duration of the product is limited, and when Macrolane degrades, it can diffuse into the gland and most likely leave the breasts via the lymphatic system.

Trignano et al. 2020 revealed that after injecting Macrolane into the breast, asymmetrical volume loss with lump creation was noticed. Furthermore, after surgery, there was lymph node enlargement in the right axilla, and a biopsy revealed a high concentration of hyaluronic acid (Trignano, Baccari, Pili, Serra, & Rubino, 2020). From the radiological point of view, hyaluronic acid represents a diagnostic challenge, not only because of its current usage but also because it interferes with image interpretation. Macrolane often identifies an increase in the breast parenchyma radiodensity at mammography, which may be either generalised or seen as multiple radiodense lesions (Criado, Braojos, Torres, & Muniz, 2012). The result correlates to several predominantly anechoic collections with internal echoes of varying sizes and echogenicities in ultrasonography. Hyaluronic acid collections appear as well-defined regions with hyperintensity on T2-weighted images and hypointensity on T1-weighted images on magnetic resonance imaging (Pienaar et al., 2011). Macrolane collections may occasionally be associated with fibrotic capsules, assuming a more concerning radiological appearance.

However, new hyaluronic fillers for volume restoration treatments, such as breast augmentation, may become available after safety investigations and cost-effectiveness.

Injectable fillers are commonly utilised in soft tissue augmentation and reconstruction. Natural and synthetic biomaterials are the two types of injectable materials. Natural fillers provide the benefit of biocompatibility and degradation over time. However, natural fillers have disadvantages, such as high absorption rates and a minimal filling effect. On the other hand, synthetic fillers have limited biocompatibility with varying mechanical strengths (Park et al., 2021). The appropriate filler material may be produced, and current limitations such as migration, nodule formation, and foreign body reaction might be avoided.

2.15 Normal Breast Tissue and Its Impact on MPI SPECT/CT Imaging

In adults, the breast lies on the anterior of the chest wall, between the second rib, inferiorly above the sixth rib, medial to the sternal edge and lateral to the mid-auxiliary line (Hogg, Kelly, & Mercer, 2015). Female breasts consist of glandular, fibrous and adipose tissue. The amount of adipose tissue determines the size of the breast (McGuire, 2016). Commonly, females who are younger tend to have denser glandular tissue compared to older females, who tend to have less glandular tissue.

Breast size, position, configuration and density differ among women. Thus, an artefact from breast tissue attenuation can vary considerably in its appearance. Anterior and lateral artefacts are more common, while inferior artefacts can occur in females with large breasts (Mannarino et al., 2019). True perfusion defects can be difficult to distinguish from these artefacts (Chawla et al., 2011). Thus, for women with large breasts, the accurate diagnosis of anterior wall defects may be challenging (Gimelli et al., 2013).

During scanning, a female patient lies in a supine position in most commercially available SPECT/CT scanners. The left female breast overlies the anterolateral wall of the heart in the normal female body. Larger pendulous breasts lie close to the lateral chest wall and contribute to a lateral attenuation artefact. Moreover, for females with very large breasts, the entire LV might be covered (Taneja et al., 2008; Heston, 2011). Qutbi & Soltanshahi (2018) evaluated the MPI in two protocols (stress and rest) for females who had chest discomfort for several months. This study found that breast attenuation can cause false-positive defects. The stress and rest images illustrated a perfusion defect in the anterior wall of the LV (Qutbi & Soltanshahi, 2018). Abnormal perfusion defects were highlighted because of breast attenuation artefacts. Using binders over the left breast decreased the soft-tissue attenuation and caused the images to show normal perfusion (Qutbi & Soltanshahi, 2018). A binder is utilised to flatten the breasts against the chest wall, and this procedure might be useful in decreasing breast thickness. However, there is typically a degree of uncertainty about the actual position of the breast under the binder. Furthermore, precise repositioning of the breast under the binder is challenging in stress and rest scans. In a recent study binders were used to flatten the breast onto the chest and resulted in more uniform attenuation and reducing breast attenuation artefacts (Qutbi & Soltanshahi, 2018).

Applying CTAC to address soft-tissue artefacts in MPI for women patients who have CAD may support physicians in diagnosing patients more accurately. DePuey et al. (2019) analysed MPI images for a female patient with CTAC and without CTAC. The study found that, before applying CTAC, breast attenuation artefacts could mimic an ischaemia defect. However, with AC, to reduce soft-tissue attenuation artefacts, the SPECT images were revised, and the images were normal (DePuey, Morley, & Leykekhman, 2019).

Płachcińska et al. (2016) evaluated whether visual, semiquantitative analysis of attenuation-corrected (SPECT/CT) MPI is advantageous over non-corrected images. The study applied CTAC to evaluate images of 107 patients (56 males and 42 females) with CAD. Two experienced nuclear medicine specialists analysed images (comparing corrected to

uncorrected) by applying a semiquantitative visual method. Płachcińska et al. found that CTAC increased the specificity of detecting CAD in male and female patients from 63% to 86%. CTAC removes soft attenuation artefacts produced by breast tissue in females and by the diaphragm in male patients (Płachcińska et al., 2016).

Raza et al. (2016) compared images of NAC and attenuation-corrected myocardial perfusion SPECT/CT. The study found that activity uptake decreased within the anterior wall of the myocardium in NAC images, whereas a normal tracer distribution was seen with attenuation-corrected images. This study showed that CT-based attenuation-corrected SPECT MPI significantly improved SPECT MPI specificity compared with NAC.

Soft-tissue attenuation is the most common cause of artefacts in the SPECT/CT myocardium due to the different tissue densities and attenuation coefficients surrounding the heart. AC has been adequately addressed by the invention of hybrid SPECT/CT systems. Still, hybrid SPECT/CT technology remains expensive, and CTAC is recommended for routine clinical use (Van den Wyngaert et al., 2020).

2.16 Definition and Types of Breast Implants

The term "breast implant" refers to a prosthesis utilised to change a woman's breast size and shape for aesthetic purposes, such as congenital chest wall abnormality correction and breast reconstruction after mastectomy. The most common plastic surgery procedure carried out in the UK in 2017 was breast augmentation. In 2017, 8,238 breast augmentations were performed, with the number of operations increasing 7% from the previous year (Surgeons, 2019, March 27). The most recent National Mastectomy and Breast Reconstruction Audit, conducted in 2011, found that 16,458 females had a mastectomy; 21% (3,389) of these had immediate reconstruction surgery, and the remaining 10% (1,731) underwent delayed reconstructive breast surgery (Davis & Jyothirmayi, 2017).

Breast implants are available with two types of fillers: silicone and saline. In 1961, the first silicone gel implants were produced. This type of implant has since been improved (Spear & Jespersen, 2010). Silicone gel implants are popular because of their natural weight and feel. Moreover, these implants are available in various shapes (Park et al., 2021). If a young woman opts for silicone gel implants for breast reconstruction, she will likely need to replace the implants in the future. Breast implants do not have an expiration date; however, an exchange is usually required owing to general complications. A meta-analysis found that silicone gel implants had a median lifetime of 16.4 years (Goodman, Cohen, Thornby, & Netscher, 1998).

Silicone is commonly used because its toxicity is low, it is biologically stable, and it can be easily shaped and moulded. In 1963, the Dow Corning Corporation introduced the first silicone-gel-filled implant. This implant consisted of gum filled with amorphous silica. The shell of this implant was thick, and the surface of the implant was smooth with seams. The disadvantage of the first implant was that it was prone to leakage and capsular contracture (Peters, 2002). In the second generation, implant shells changed from a thick to thinner shell to minimise the incidence of capsular contracture. Polyurethane foam was used to coat the shells of the implants, but this coating caused inflammation, which in turn caused the formation of fibrous tissue around the capsule, followed by pain, infection and fluid accumulation (Barr & Bayat, 2011). In the third-generation implants, bleeding, deflation and rupture occurred less often, as they had a thick shell with barrier layers and textured surfaces. The silicone gel implants in the fourth generation were the same as in the third, but with a textured surface. In contrast, the fifth generation featured cohesive silicone gel-filled implants (G. P. Maxwell & Gabriel, 2017).

The first usage of saline-filled breast implants was reported in 1965; however, clinical studies to assess this implant were conducted less than a decade later. It was not widely used initially (Kaoutzanis, Winocour, Unger, Gabriel, & Maxwell, 2019). In the 1970s, when incidences of capsular contracture with silicone implants were recorded, saline implants rose in importance. Saline-filled breast implants include a silicone outer shell filled with a sterile saltwater (saline) solution. Saline implants were produced in the 1950s, but the early category was limited by high deflation rates (Spear & Jespersen, 2010). Breast implants with saline were popularised in North America during the 1990s because silicone implants were banned due to safety problems, including an association with connective tissue diseases. The greatest benefit of the saline implant for breast augmentation was that it could be introduced through a small incision since it could be inserted prior to inflation (Park et al., 2021). After the implant was inserted, liquid saline was used to inflate it, and adjustments in the volume were possible within a specific range. However, the saline implant had many drawbacks. First, the early saline-filled implant had a significant deflation rate due to underdeveloped shells and valves. Second, the post-filling procedure had some pitfalls (Young & Watson, 2001). Underfilling with saline led to higher deflation rates and noticeable surface wrinkles, whereas overfilling resulted in unexpected shape deformations and unnatural firmness (Spear & Jespersen, 2010). Most importantly, the implant did not feel like natural breast tissue when palpated after insertion into the breast. Because of the limitations of saline implants, there was an increased demand for a more natural and consistent implant material.

Breast saline implants continue to be used but have disadvantages, including a firm consistency and greater possibility for observable deflation and resultant re-operation. In contrast, breast saline implants have advantages, including fill volumes larger than those offered with silicone implants and lower costs than silicone (G. Maxwell, Baker, & Gabriel, 2006).

The sizes of implants typically range from 80 to 800 cm^3 in volume, and 1000 cm^3 have been used on occasion. Diameters range from 7.5 to 16.8 cm, and the depth from the chest wall to the nipple varies from 1.5 to 7.5 cm. The implant diameter must be adequate to cover the natural breast size diameter without extension too far towards the cleavage and underarm (Herdman, Ernster, & Bondurant, 2000).

Various artefacts can degrade the quality of reconstructed SPECT/CT images. One of the primary sources of artefacts is the existence of high-density objects, such as breast implants. The materials used in breast implants have a higher atomic number than human breast tissue and therefore may have a more significant impact on attenuation in SPECT imaging of cardiac structures. Silicone contains the heavier element silicon (atomic number ($Z = 14$), which is a higher density than soft tissues, which predominantly contains lighter elements (hydrogen $Z = 1$, carbon $Z = 6$, and oxygen $Z = 8$), leading to more attenuated photons and beam hardening when the photons transverse through silicone implant materials (Glazebrook et al., 2019). In addition, the density of breast implants is greater than that of normal breast tissue.

This may lead to incorrect CT HU values and an incorrect attenuation map, affecting the diagnostic accuracy.

2.17 Breast Implants – Implications for SPECT/CT Imaging

As discussed in Section 2.12.1, natural breasts may produce artefacts, which is one of the key limitations of SPECT/CT MPI. These artefacts are mainly based on the size of the breast and breast location, and they can be difficult to distinguish from true perfusion defects. Furthermore, because breast implants are denser than normal breast tissue, they are predicted to produce more marked attenuation compared to normal breast tissue during MPI. This may cause more marked false-positive defects. Thus, there is the potential for an increase in unnecessary invasive cardiac procedures in females undergoing MPI who are suspected of having CAD.

Due to notable increases in recent cosmetic surgery rates, the number of women with breast implants who undergo SPECT MPI will increase (Stinis, Lizotte, & Movahed, 2006). The existence of high object densities that can overlay the anterior wall of the heart might markedly

increase attenuation artefacts. Depending on the partial or complete coverage of cardiac structures by breast implants within the image acquisition at stress or rest imaging, partial or completely reversible defects can be seen.

Caner et al. (1999) investigated the impact of breast implants on MPI. The researchers examined a patient with small breast implants (227 ± 30.9 cc) and a variety of breast implant sizes (80–800 cc). Thallium (^{201}TI) was used as the radiotracer, which is now not commonly used due to its low photon energy (67 keV) and the risk of attenuation by the patient's organs, resulting in a reduction in the count at the detector/gamma camera (perfusion defect; (Caner et al., 1999). In this study, 29 women who had breast implants and 14 females in a control group (normal breasts without implants) were studied in a resting condition. The results demonstrated that the count density of the myocardial wall in women with implants was reduced compared to the count density of the myocardial wall in the control group (Caner et al., 1999). The size, location and type of the breast implant determined the severity and position of the perfusion defect (Caner et al., 1999). It should be noted that AC was not carried out in this study (Caner et al., 1999).

Meine et al. (2005) studied the SPECT myocardial perfusion images of a female patient who presented with chest pain and had undergone a left mastectomy and breast reconstruction with silicone. The study found that a silicone breast implant on the left side interfered with nuclear imaging of the myocardium. The study found that the silicone breast presented a large fixed anterior wall perfusion defect with normal anterior wall motion marked in the SPECT image. A woman's coronary SPECT imaging revealed widespread infarction in the anterolateral, inferior, and posterolateral walls and mixed ischemia/infarction in the anterior wall. Following cardiac MRI, only the anterolateral and inferolateral infarcts were shown. The anterior wall was completely viable. MR imaging also revealed a left breast implant overlaying the anterior cardiac wall (Meine et al., 2005).

Movahed (2007) studied SPECT the myocardial perfusion images of a 46-year-old woman who presented with atypical chest pain and had undergone breast reconstruction with saline breast implants. The study found that a large breast implant shadow could be detected in the raw images; significant attenuation of the anterior wall produced by the implant could be observed in the SPECT image (Movahed, 2007).

Stinis et al., (2006) reported two cases of impaired myocardial SPECT imaging in a female with breast implants. As breast implants often compress natural breast tissue, the radiotracer

uptake through myocardial SPECT imaging by compressed breast tissue may seem to increase. Binders might be used to bind the large breast in a rest scan. However, large breast implants may cause more attenuation due to both the size of the breast implant and the fact that silicone that has a higher density than normal breast tissue (Stinis et al., 2006). Also, there is usually a degree of uncertainty about the true location of the breast under the binder. Furthermore, precise repositioning the breast under the binder in stress and rest scans is difficult. Depending on the heart's partial or complete coverage by breast implants through the acquisition of the image at rest or stress, a defect could be marked as partial or completely reversible. This can cause further difficulty in the interpretation of SPECT images for breast implant patients. Breast implants can create significant attenuation artefacts through SPECT imaging, which can make CAD diagnosis in females more challenging.

In a recent study, Ramos et al. (2020) studied breast implant attenuation artefacts in supine and prone positions. The authors reported that perfusion uptake increased with prone positions for all breast implant sizes, mostly in the anterior and inferior LV segments in the short axis. This may have been due to the tissue of the breast flattening when the phantom was set in this position, decreasing the thickness of the tissue that the radiation needed to pass through (Ramos et al., 2020). The study showed that very large breast implants impacted photon counts compared to all other breast implant sizes. The photon counts were decreased more in the anterior wall region for very large implants compared to the different breast sizes, and there is an added risk of artefacts from breast implant attenuation, which could compromise the MPI results (Ramos, Glavam, de Brito, Kubo, Tukamoto, Sampaio, & de Sá, 2020).

Attenuation maps must be accurate; otherwise, they could cause over- or undercorrection of the emission data. A severe impact can be found in a patient who has metal implants, for instance. This can cause a high overestimation of the attenuation coefficient. Therefore, reviewing images with attenuation-corrected and NAC emissions is important for increasing accuracy performance (Baert, 2006).

In 2014, breast augmentation was the leading cosmetic procedure that was performed in the United Kingdom (UK) (Govrin-Yehudain et al., 2015). According to the Breast and Cosmetic Implant Registry (BCIR), in 2020, 10,500 patients in the UK had undergone a breast implant procedure (Breast and Cosmetic Implant Registry (BCIR), 2021,October 06).

During single-photon emission computed tomography myocardial perfusion imaging (SPECT MPI), photons are absorbed by the heart, thus, that organ becomes the source of photons

detected by the gamma camera. However, the patient's size and the amount of tissue between the heart and the detector can lead to attenuation artefacts that impact the image of the heart. Photons emitted by the radiotracer interact with tissue and other organs as they pass through the body. Photons emitted by the radiotracer can undergo photoelectric interactions where they are either completely absorbed or they interact and undergo Compton scattering.

Different artefacts can reduce the image quality of the reconstructed computed tomography (CT) slices. One of the primary sources for artefacts is the presence of high-density objects such as breast implants. Due to different physical effects, such as scattering, beam hardening, noise or total absorption, projections that pass through a high-density object can become useless in terms of reconstructing the scanned object. This leads to incorrectly reproduced CT HU values. Furthermore, breast implants can prevent the meaningful estimation of myocardial perfusion by a SPECT gamma camera because their presence can create significant artefacts (Farag & Heo, 2015; Henzlova & Duvall, 2019).

CT is used to generate attenuation correction maps to compensate for the soft tissue artefacts that may be present in the SPECT MPI. Furthermore, high-density objects, such as breast implants, can degrade the quality of the reconstructed CT images. Silicone implants are denser than normal breast tissue, leading to the risk of attenuation artefacts. The density of saline implants is equal to that of water, whereas silicone implants are made of a material with a higher density. This may lead to incorrect CT numbers, which would affect the diagnostic accuracy, leading to a false-positive diagnosis that could result in unnecessary cardiac diagnostic tests, such as invasive coronary angiography, which come with an increased risk of complications.

To date, no previous research study has examined the impact of different sizes of breast implants (silicone gel or saline) on the accuracy of attenuation correction maps for the CT component of SPECT MPI.

2.18 Thesis Aims and Objectives

2.18.1 Aims

1- To evaluate the changes in CT number values within the CTAC map of the myocardium region when silicone breast implants of varying sizes are added to an anthropomorphic phantom during MPI SPECT/CT.

2- To evaluate the effects of the tube current on CT number accuracy within the myocardium region in a phantom.

2.18.2 Objectives

1- To develop and test an image acquisition method to evaluate the impact of adding different sized silicone breast implants on CT number accuracy.

2- To develop a reliable and repeatable image analysis method that illustrates the impact of breast implants on the measured CT numbers associated with the myocardium region.

3- Where there is a change in the CT numbers, determine the required changes in tube current mA to compensate for the breast implants' impact.

2.19 Research Question

What impact do breast implants have on the CT numbers attributed to the myocardium region within the CTAC map for SPECT/CT myocardium perfusion imaging? a phantom-based study.

2.20 Experimental Study Aims

The purpose of the experimental study described in this thesis was to evaluate the effect of breast implants on the CT numbers attributed to the myocardium region within the CTAC map for SPECT/CT myocardium perfusion imaging. The research was a phantom-based study using MPI SPECT/CT.

Three experiments were carried out. Recognising the pressure on access to clinical facilities, the first experiment used a diagnostic CT scanner at the university of Salford to design the method to be used in the clinical centre. The experiment evaluated the impact of three different breast implants on the accuracy of CT HUs when three different tube currents were used.

The second experiment was carried out in the clinical centre (Manchester Saint Mary's Hospital) using the CT components in a SPECT/CT scanner to assess the impact of three different breast implants on CT number accuracy when CTAC is applied in SPECT/CT MPI. Any errors in CT numbers were considered errors in the radiotracer's estimated attenuation coefficients that would impact the attenuation-corrected SPECT data. This means that CT

number inaccuracies were recognised as leading to inaccuracies in the corrected SPECT data, which could degrade the image quality of SPECT/CT.

The last experiment used a clinical SPECT/CT scanner and used ^{99m}TC as a radiotracer to mimic the actual MPI scan. In this experiment, the local clinical protocol was used to assess the impact of breast implants on cardiac corrected counts, the values used in diagnosis.

Chapter 3: First Experiment: An Assessment of the Effect of DIFFERENT BREAST IMPLANT SIZES on CT Number Accuracy Within the Cardiac Region: Phantom Study

Accurate diagnosis of CAD can reduce cardiac disease complications or the need for further risky procedures, such as angiography. However, the accuracy of the diagnosis might be affected by CT artefacts, such as beam-hardening artefacts. Beam hardening is one of the most frequently encountered CT artefacts (Lamba et al., 2014). Beam hardening may change CT HUs, leading to incorrectly lowered HU measurements. Because breast implants have a higher density than normal breast tissue, the probability of beam hardening increases.

The first experiment was designed to establish and test an image analysis technique before carrying it out in the SPEC/CT scanner at the clinical centre. It was done to support a reproducible and reliable methodological approach. The experiment assessed the impact of breast implants on CT HU accuracy within the ROIs of the cardiac region of the phantom. The experiment was conducted in the university lab using a diagnostic CT scanner to optimise the experiment process and minimise the time required for the clinical experiment.

This experiment was designed to validate a method for discovering a way to properly assess the impact of silicone breast implants and tube currents on CT HU accuracy within the cardiac region of an anthropomorphic chest phantom from CT scans across a range of scanning parameters. In doing so, this experiment assessed cardiac CT HU variations due to changes in tube current and silicone breast implant size. The study involved the use of anthropomorphic phantoms. Measurements were made using ImageJ to obtain and record the cardiac CT (HUs), noise (standard deviation [SD] of HUs) and range (minimum and maximum HUs).

3.1 Aims

To determine a suitable image analysis technique for assessing the impact of breast implants on CT HUs in a simulated cardiac region with different CT acquisition parameters for different breast implant sizes.

To assess the impact of a different tube currents on the accuracy of CT HUs in the cardiac region.

3.2 Objectives

- To establish a baseline image data set for each tube current without breast implants.

- To evaluate the impact of breast implant size on the accuracy of CT HUs in the cardiac region.

- To identify a suitable image analysis method for assessing the impact of breast implants on the CT HUs accuracy of the simulated cardiac region.

3.3 Materials and Equipment

Data were acquired using three different tools: a CT scanner, a LUNGMAN phantom and three different sizes of silicone breast implants.

3.3.1 CT Scanner

The CT scanner used throughout this experiment was a Toshiba Aquilion 16 CT scanner (Toshiba Medical Systems, Tokyo, Japan), a third generation multislice CT scanner. A full specification of the Toshiba Aquilion 16-slice CT scanner is given in Appendix I. Before data collection commenced, the CT scanner was warmed up and air calibrated, following the manufacturer's daily warm-up procedure, to check that the CT scanner was working within tolerance. The scanner is subjected to checks at regular intervals by the engineering team from Toshiba and a Medical Physicist from The Christie Hospital in the Northwest of England. The checks ensure that system performance falls within tolerances recommended by the manufacturer.

The quality control (QC) process employed in this study was based on the recommendations and references set out by the American Association of Physicists in Medicine (AAPM, 2006), the Institute of Physics and Engineering in Medicine (IPEM) and the American College of Radiology (ACR, 2017). The daily QC checks were recommended by the ACR (2017) and included image noise monitoring, the accuracy of CT numbers using water and the presence of artefacts. According to the HU definition, the CT number for air should be -1000 HU and water should be 0 HU. These two values present two calibration points that impact the CT numbers of all other materials. The tolerance CT number is ± 4 HU for water and ± 10 HU for air (Kuttner et al., 2013). In this experiment, the QC procedure was conducted using a TOS phantom, which is a CT QC phantom (Toshiba Medical, Tokyo, Japan). The TOS phantom is a cylindrical shape utilised to mimic the scanning of the head and body. This phantom has five circular objects made from different materials – polypropylene, nylon, acrylic, Delrin and air (-100, 100, 125,

340 and -990 HU, respectively, at 120kVp) – and the TOS phantom is filled with water (0 HU;(Kayugawa et al., 2015). The results recorded for all QC procedures were within acceptable levels according to the recommendations of the radiation protection legislation by the ICRP (2007) and Toshiba (2014). See (table 2).

Table 2 for details. The nylon material within the TOS phantom has a CT number (HUs) similar to that of the breast implants that were used in this experiment. The variations in the CT number (HUs) of the nylon for this CT scanner were within ± 2 HU when the QC check was performed (table 2).

Table 2: List of materials and measurements used in the daily QC for the TOS phantom

Quality check for CT TOS phantom						
Insert	Material	Actual HUs	Range	Measured HUs	Difference in measured HUs from actual HUs	Acceptance
A	Air	-990	-1015 to -975	-984.4	5.6	accepted
B	Delrin	340	330 to 350	330.7	-9.3	accepted
C	Acrylic	125	120 to 140	133.3	8.3	accepted
D	Nylon	100	90 to 110	102.2	2.2	accepted
E	Polypropylene	-100	-115 to -95	-104.2	-4.2	accepted
F	Water	0.0	-5 to 5	-0.8	-0.8	accepted

3.3.2 Anthropomorphic Phantom

A phantom study is commonly used in experimental radiation, instead of the patient, to avoid the patient receiving unnecessary radiation. Imaging phantoms are essential tools for optimising and balancing the radiation dose and image quality in CT examinations. Imaging phantoms are fixed objects that can be scanned repeatedly. A standard phantom is used to create optimal protocols. It should be stable, have precisely defined properties to allow scanner performance monitoring and have accurate image-based measurements (Stupic et al., 2021).

The LUNGMAN (Kyoto Kagaku, Kyoto, Japan, 2015) used in this experiment allowed the researcher to try multiple breast implant sizes and acquire the parameters. The drawbacks of this phantom are that it does not have the same anatomical and body composition as humans and respiratory motion cannot be replicated. In addition, the phantom is only one size and cannot represent a range of patient body habitus. However, the phantom can be used for both radiography and CT imaging.

The inner components of the phantom consist of the chest wall, mediastinum (including heart and trachea), pulmonary vessel structure and abdomen (diaphragm) block (Figure 6). The materials used as soft-tissue substitutes have X-ray attenuation/transmission properties similar to human tissue, and the ratio of bone absorption is extremely close to that of human tissue. The substitute materials are polyurethane (gravity 1.06) for soft tissue and epoxy resin, and calcium carbonate for bone. The circumference measurement around the chest of the LUNGMAN is 94 cm, and it is 43 cm wide, 40 cm deep and 48 cm high. The weight of the phantom represents a 70 kg male. The LUNGMAN represents a normal-sized adult male chest. The phantom's internal structures are easily removed to be added to represent clinical tasks.
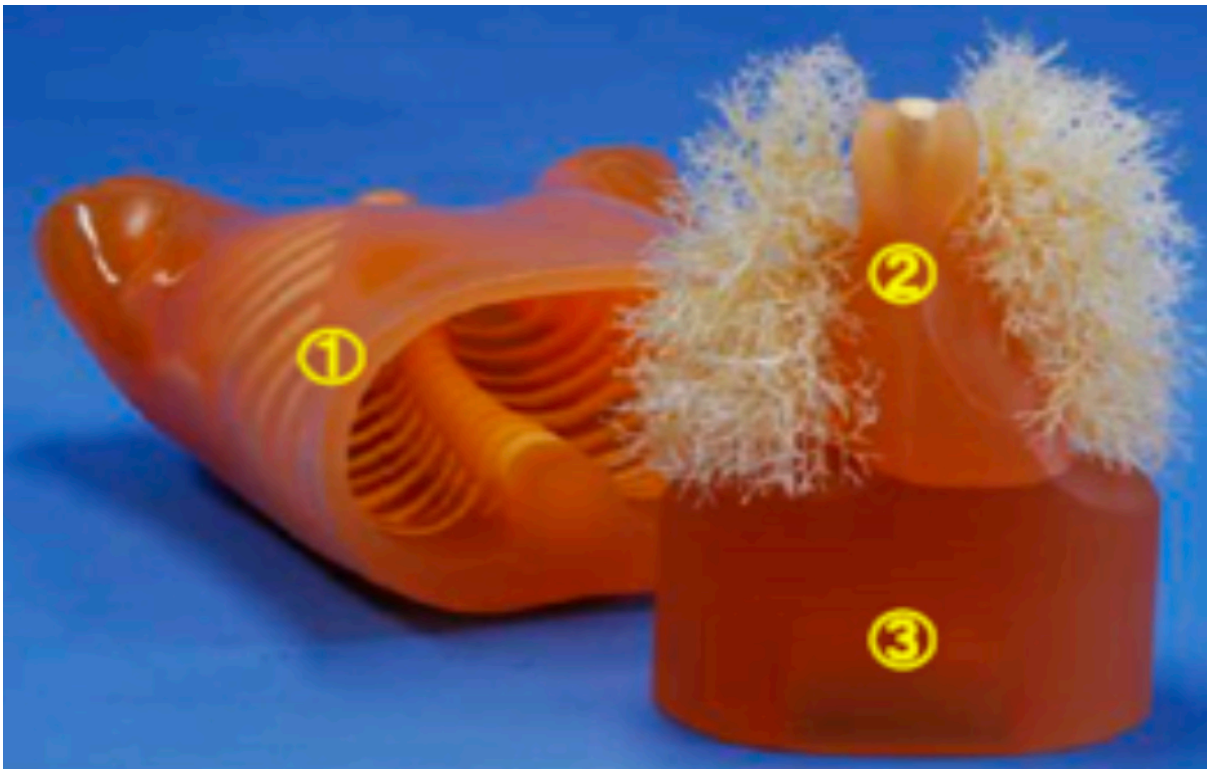
Figure 6: A multipurpose anthropomorphic adult chest phantom (LUNGMAN, Kyoto Kagaku, Kyoto, Japan). 1) Main body (chest wall); 2) mediastinum (heart and trachea included); 3) abdomen (diaphragm).

3.3.3 Breast Implants

Three different breast implant sizes (small 240 g, medium 490 g and large 685 g), corresponding to the UK cup sizes A–C, were used with the adult LUNGMAN chest phantom in this experiment (Table 3). Commercially, there are two types of implants that are approved by the Medicines & Health Care Products Regulatory Agency: silicone gel and saline. Although saline implants are the most common in the United States (COLEMAN, 2011), silicone gel implants are the most commonly used in the UK. Silicone breast implants also have a higher density than saline breast implants (Hsieh, Miroshnik, & Lam, 2013), and thus, they are anticipated to have a greater effect. Therefore, silicone implants were used in this study. This type of implant also offers an appearance and feel that more closely mimics natural breast tissue (Spear & Jespersen, 2010). If silicone was found to have a large impact on the CT numbers, saline evaluations could be performed as a further work.

The same specifications of silicone breast implants for three different sizes were attached to the phantom to assess the impact of breast implants on HU accuracy when tube current was increased. The breast implants used in this study were supplied by the Allergan Global Company (Markham, Ontario, Canada). The breast implants consisted of a rubber-like low-diffusion silicone elastomer envelope (shell), which differed in thickness from 0.075 to 0.75 mm. In adult females, the breast lies on the anterior chest wall, below the second rib and above and the sixth rib inferiorly, and from the sternal edge medially to the mid-axillary line laterally (Pandya & Moore, 2011). The breast implant was placed in the same position below the second rib and above the sixth rib.

Table 3: Characterisation of breast implant sizes

Cup volume	UK bra size	Breast size	Breast implant size used
240 cc	32 A	Small	240 g
480 cc	36 B	Medium	490 g
710 cc	38 C	Large	685 g

3.4 CT Acquisitions

The experiment was carried out on a non-clinically based diagnostic CT system. According to the literature review, both fixed tube current (FTC) and automatic tube current modulation techniques can be utilised in the nuclear medicine department to apply CTAC. However, the most frequently used technique in MPI for carrying out CTAC is the FTC technique

(Shcherbinin, Celler, Belhocine, Vanderwerf, & Driedger, 2008; Yada & Onishi, 2016). CTAC scans should only be performed at the lowest possible settings. Because it is normal to smooth the CT data before using AC, the noise has a minimal impact; therefore, the image quality can be kept low to decrease the radiation exposure to the patient. Therefore, according to the manufacturer's instructions, a low tube current (10–20 mA) is recommended to decrease radiation exposure to the patient (Camoni, Santos, Attard, Mada, Pietrzak, Rac, Rep, Terwinghe, & Costa, 2020). Therefore, the FTC technique was used in this experiment. One main protocol was used in this study, and this protocol was used for each condition (i.e. no breast implant, small, medium and large breast implants), as illustrated in table 4. The lowest two tube currents used in this experiment (10 and 20 mA) were based on the literature review, while 30 mA was also used to compensate for photon attenuation by breast implants. Changing parameters (mA) for cardiac examinations represent the range of tube currents typically employed for CTAC and allow for assessing the increasing tube current to overcome breast implant attenuation. This increased tube current technique is used to compensate for attenuation by thick tissues and preserves the number of detected photons (Inoue, Nagahara, Kudo, & Itoh, 2018).

The value of the CT tube voltage in a hybrid scanner is typically between 70 and 140 kV, and it must be adjusted based on the size of the patient. (Camoni et al., 2020). SPECT/CT can be used with a range of kVp settings . 120 kVp is used when the images might be potentially used diagnostically, because it gives a better contrast resolution. However, if the image is to be used for AC only, 140 kVp is usually used due to the energy match with ^{99m}Tc radiopharmaceutical, which is 140 keV. This study used 120 kVp because it used a diagnostic SPECT/CT scanner. Fukami et al. (2020) used low-dose CT scans for AC with the following parameters: 120 kVp, 10 mA and 1 s rotation time. Furthermore, Joseph Lee and Delaney (2021) used 120 kVp as the tube voltage and 20 mA as the tube current. Details of the CT scan protocol parameters are shown in Table 4. The CT acquisitions used by Toshiba Aquilion 16 slices are as follows: 120 kV, using combinations of tube current (mA) from 10 to 30 (10, 20 and 30 mA) and rotation times of 1.0 s and a FOV of 50 cm. A standard (0.75) pitch was used.

Table 4: Cardiac scan parameters used during CT

Protocol no.	kVp	Tube current (mA)	Rotation time (s)	Pitch	FOV (cm)	Slice thickness mm	Reconstructed slices mm
1	120	10	1	0.75	50	5	5
2	120	20	1	0.75	50	5	5
3	120	30	1	0.75	50	5	5

3.5 Experimental Set-Up

According to the clinical positioning used to scan patients and previous studies of scanning phantoms for simulating cardiac examinations, the anthropomorphic phantom (adult chest phantom) was placed in the supine position, with its head first towards the gantry according to typical protocols for MPI (Fukami, Tamura, Nakamura, Nakatsukasa, & Sasaki, 2020; Joseph Lee & Delaney, 2021). Three sizes of breast implants were attached to the adult LUNGMAN chest phantom. The scan began at the level of the sternal notch, which is above the first rib, and ended at the second lumbar spine vertebrae to include all the cardiac and breast areas. The scan range was 300 mm. The CT laser was utilised to aid positioning, and adhesive surgical tape (with location markers made using a marker pen) was placed on the surface of the phantom to enable precise repositioning and consistency.

3.5.1 Procedures for Acquiring Images

The LUNGMAN phantom was scanned under four conditions for each protocol:

1. without any breast implants as a reference using a range of tube currents (10, 20 and 30 mA);

2. with left and right small breast implants attached, with a range of tube currents (10, 20 and 30 mA);

3. with left and right medium breast implants attached with a range of tube currents (10, 20 and 30 mA); and

4. with left and right large breast implants attached with a range of tube currents (10, 20 and 30 mA).

3.5.2 Image Analysis and Region of Interest (ROI) Selection

ROIs can be used to define specific parts of an image that should be processed independently or measured; therefore, only pixels within the ROIs are included within any calculations. An assessment of CT HUs was applied using two image analysis techniques, with and without using the subtraction method, as discussed below.

3.5.2.1 Analysing ROIs of Cardiac CT Image Without the Subtraction Technique

The aim of the ROI analysis is to define the average CT HUs or sum in a region of the image. According to the literature, suitable positioning of ROIs in the cardiac region ensures coverage of the entire cardiac region or involves the LV (Hirano & Tsumoto, 2005; Mory et al., 2014; Salih, Hamid, Bakar, Yahya, & Dewi; Tautz, Friman, Hennemuth, Seeger, & Peitgen, 2011). To determine the ROI, CT-axis images were used to draw the ROI inside the cardiac cavity that represents or mimics the LV (see Figure 7). This method involved drawing the ROI for the LV region to simulate the heart chamber's location, which represents the anterior wall.

In this experiment, the cardiac region of the phantom was examined, starting from the top of the aortic arch and ending with the diaphragm. The HUs of nine cardiac slices were measured. The same ROI was applied to the equivalent slice for each protocol. The mean HUs, SD of HUs and range (minimum and maximum values of the HUs) in the cardiac ROIs were measured using ImageJ software version 1.51 (National Institute for Health, Bethesda, MD, USA). This NIH-Image software can assess each pixel density, and through advances in the NIH-ImageJ software package, the density measurements were calibrated to reflect the actual HU values (Irving et al., 2007).

Reference images, which had no breast implants attached, were compared with images of different sized breast implants. The ROI was defined on the reference images of the phantom to ensure that any influence caused by the breast implants was removed. Thus, a reference image without breast implants using a 10 mA tube current was compared with images of the three different sized implants also using a 10 mA tube current; a reference image without implants using a 20 mA tube current was compared to images with the three different sized implants also using a 20 mA tube current; and finally, a reference image without breast implants using a 30 mA tube current was compared with images of the three different sized implants also using a 30 mA tube current. CT HUs, SD of HUs and range values of HUs among all breast implant attachments were compared to reference images to assess the impact of breast implant size on the accuracy of CT HUs within the cardiac structure of the phantom.

The ROIs were selected to cover all cardiac slices. The ROIs were drawn for the LV of the cardiac phantom region (Figure 7) in each slice to evaluate breast implant attenuation. In this technique, freehand drawing was used to be accurate, and no irrelevant structures were included. The reference condition – small, medium and large breast implants – were scanned under three different tube currents. Because the quality control (QC) of CT was done before the experiments, and the system was operating consistently the QC should apply consistently between acquisitions. Therefore, a single image set, rather than 3 repeated images was used for each condition. Thus, 12 image sets were acquired in this research. Then, nine slices were acquired for each image set to cover all the cardiac regions. For each cardiac region slice, the ROIs were independently drawn three times, and a mean was calculated to ensure that the measurement was reliable and to minimise reproducibility (operator) errors. The following equation calculated the $average\ CT\ HUs$ within ROIs:

$$Average\ CT\ HUs = \frac{R1+R2+R3}{3}, \qquad (1)$$

where:

R_1 = the CT HU value measured from the first ROI

R_2 = the CT HU value measured from the second ROI

R_3 = the CT HU value measured from the third ROI
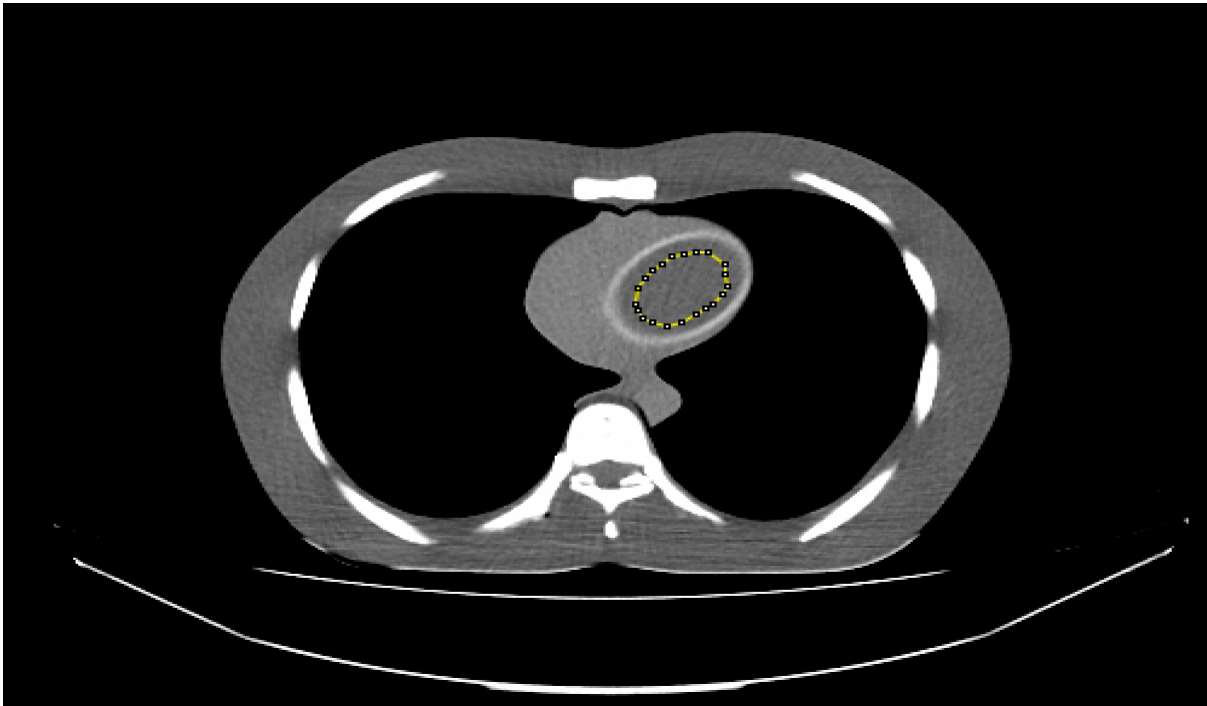
Figure 7: ROI for the LV of the cardiac phantom region with the 30 mA tube current.

3.5.2.2 Thresholding vs Manual ROI

To select the region within the phantom that represents the cardiac region, automatic selection or manual selection can be used. Thresholding (known as the "magic wand") can be used to automatically select ROIs in ImageJ software. However, this uses the HU values to choose the edges of a region. As the introduction of the implant may cause a change in the HUs, using thresholding would exclude the data of interest due to the change, depending on the threshold set. Additionally, the thresholding method selects any HUs corrected to the ROI within the threshold range and does not discriminate between anatomical structures. As a consequence, irrelevant anatomy might be selected, along with inconsistent ROIs. Therefore, in a complex region, it is impossible to correctly threshold and isolate the cardiac region accurately (Figure 8). Due to these issues, it was decided that the ROIs should be drawn manually.
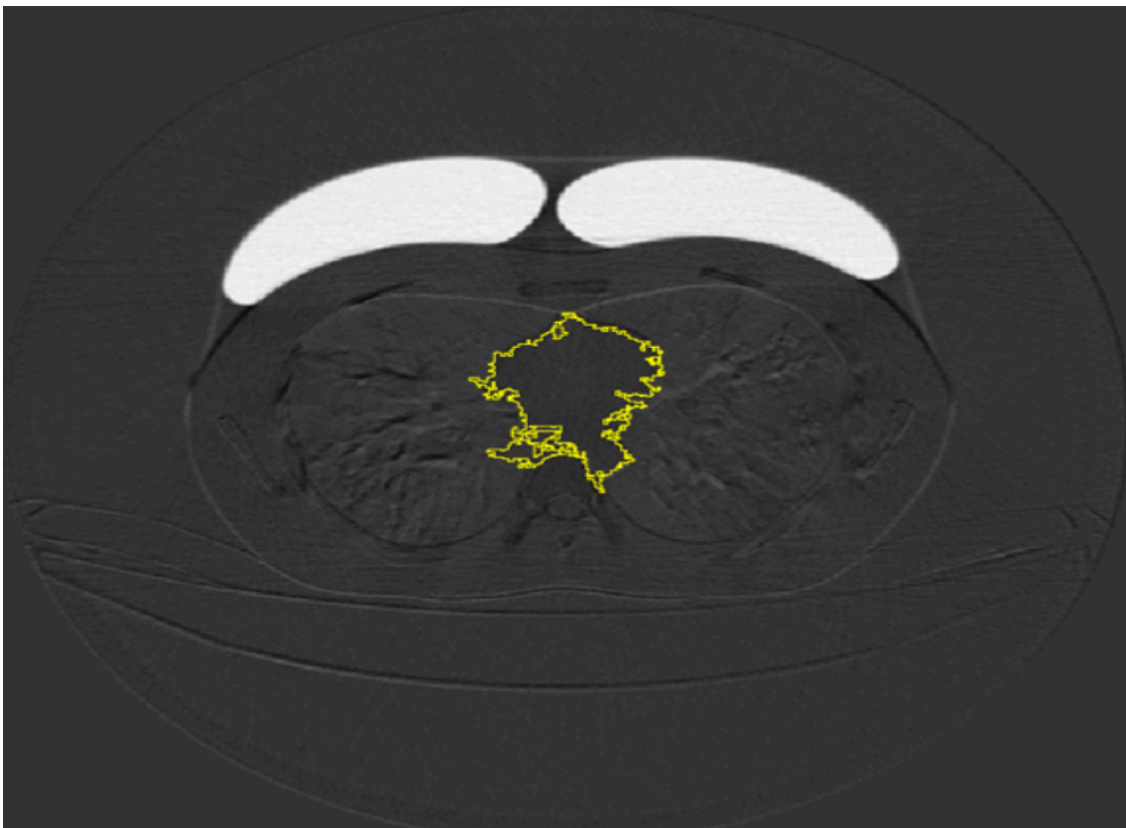
Figure 8: Thresholding method. Cardiac tissue and adjacent tissues were included.

3.5.2.3 Analysing ROIs of Subtraction Cardiac CT Image

The presence of a foreign object, such as silicone breast implants overlying the anterior wall of the cardiac region, can increase attenuation and can impact the image quality (Stinis et al.,

2006). A subtraction method was also used to investigate any small CT HU inaccuracies, as explained below. This study selected the LV of the phantom.

Image subtraction is a process that uses the digital conversion of an image to perform subtraction of the pixel values between two different images. The subtraction technique performs subtraction calculation processing between the experimental condition images (when breast implants were attached) and the reference images (no breast implants attached) for each tube current. The subtraction technique involves subtracting images with breast implants from their baseline (no added breast implants) to measure differences in CT HU between the two conditions (with and without breast implants). When the subtraction technique is used, any other variables that could impact image quality, such as slice thickness and pitch, were kept constant. Thus, this technique is a useful analysis technique to measure a change in CT HUs because all other variables that can impact the image are controlled. According to the literature review, the subtraction technique can improve the subtle changes between the CT images. To calculate the overall change in the CT HUs between the reference and the corresponding image that included an implant, the image subtraction method available in ImageJ was used. The small, medium and large breast implant images were subtracted from the reference images, as seen in Figure 9. The differences represent the change in CT HUs per slice between the reference image and the image containing the breast implants. Therefore, the range indicates the change in the CT HU value due to the silicone gel breast implants.

The nine-image set was acquired because three different tube currents were used for each breast implant condition. Then, nine slices were acquired for each image set to cover all cardiac regions. The ROIs were independently drawn three times for each cardiac region slice, and a mean CT HU was calculated to ensure that the measurement was reliable and to reduce reproducibility (operator) errors.

For each subtracted slice, the mean CT HU, noise (SD in HUs) and range values of CT HUs within ROIs were measured using ROIs in ImageJ; these values were calculated from the resultant subtracted image. The ROIs were drawn three times for each image; then, the CT HUs, noise and range were recorded within each ROI within the cardiac slices. The data were then averaged for all measurements within the ROIs in the cardiac region.

The ROIs were applied across all subtracted image sets for consistency. The ROI manager function within ImageJ was used to save and apply the ROIs to improve the reliability of the results. An ROI manager was used to save the ROIs to improve the reliability of the results

(Bhosale et al., 2015; Lança et al., 2017; Manson et al., 2016). An ROI manager is a tool for working with various selections. The selections can be from different locations on an image or from different stack slices.

For each ROI, the CT HUs, noise (the SD in HUs) and range values of CT HUs within the ROIs were recorded per slice. The data were then averaged across all slices within the cardiac region for each subtracted image set. These variables were measured to assess the impact of breast implant size on the accuracy of CT HUs.
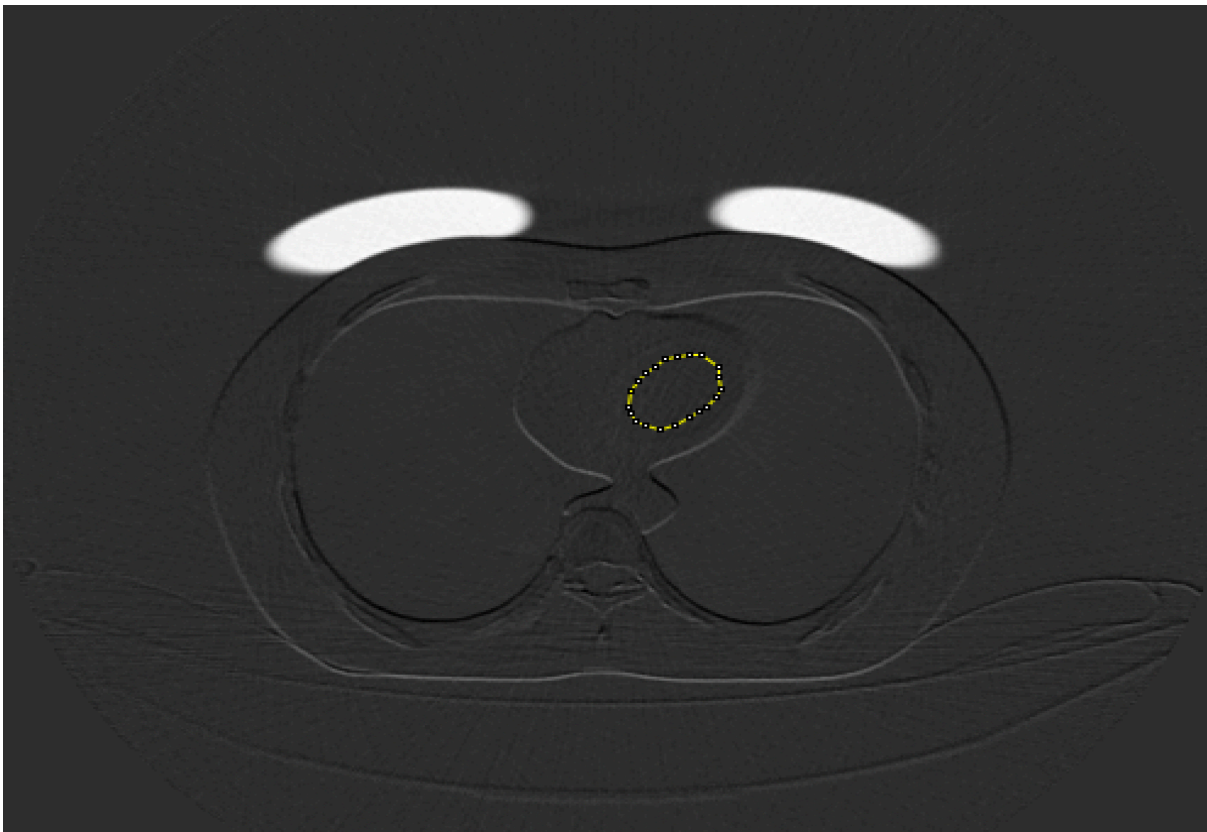
Figure 9: Subtraction image. The result of a subtraction between the reference image and an image with a large breast with a 30 mA tube current.

The CT HUs for each ROI in the cardiac tissue slices were recorded from the reference image. In this technique, the ROI was placed away from the cardiac slice edges to avoid the partial volume effect caused by objects of varying density. The partial volume effect impacts the true linear attenuation coefficient measurement, as some X-rays penetrate other parts of the object.

The accuracy in CT HUs was calculated using the following equation:

$$I_X - A = 0, \hspace{3cm} (2)$$

where:

I: average CT (HUs) in the ROIs for breast implants

X: small, medium and large breast implants

A: average CT HUs in the ROIs for no breast implants (reference)

0: CT HUs

3.6 Quantitative Assessment of Image Quality

Quantitative analysis was performed on the same workstation. Mean CT HUs, noise (computed as the SD of the CT HUs) and range (computed as the minimum and maximum of the CT HUs). Range is defined as the difference between the maximum and minimum value within ROIs and was calculated for the cardiac region of the phantom under three conditions: no breast implant attachment as a reference image; small, medium and large breast implant attachment at different tube currents; and placing a defined ROI on the LV of the cardiac region of the phantom. The mean CT HUs, noise and range were calculated for cardiac structure by averaging the values derived from all slices of the cardiac CT under study.

3.6.1 Statistical Analysis

Two pieces of software were used to evaluate the data: SPSS Version 23 (IBM Corp, Armonk, NY) and Excel 2013 (Microsoft Inc, Redmond, WA). Statistical testing was conducted using SPSS, and the tables and graphs were created in Excel and GraphPad to illustrate and describe the results that were collected. Inferential statistical analysis was performed using an independent t-test. P-values of less than 0.05 were considered statistically significant. According to Kent State University (2019), the independent t-test compares two means from different individuals. Thus, independent sample t-tests were performed to find significant differences between the reference image (no breast implant attachment) and the small, medium and large breast implant attachments, respectively, when the three different tube currents were used.

However, as the subtraction method was used, the data had already been compared to the reference. Therefore, inferential statistics were not possible. Although comparisons could be

made between small, medium or large breast implants, this was not deemed appropriate, as clinically, individual patients would not have different implant sizes.

3.6.2 Reproducibility

Reproducibility refers to the difference in measurements taken on a subject under changing conditions (Bartlett & Frost, 2008). It can be mathematically defined as the variability of the average values acquired by one observer while measuring the exact item under different conditions, such as the item's location (Slezák & Waczulíková, 2011). It is the SD of the multiple repeatability test results, where the measurement conditions have been altered. In this experiment, the reproducibly was conducted by analysing the cardiac CT images of the phantom (image without subtraction technique) of the reference. When the small, medium and large breast implants were attached, the twelve-image set was acquired, and then, the nine slices were acquired for each image set to cover all the cardiac regions. The ROIs were drawn once for each image, and then the ROI manager was used to transfer the ROIs to the other images. The ROIs were independently drawn three times for each cardiac slice, and a mean CT HU was calculated to ensure that the measurement was reliable and to reduce reproducibility errors (see Table 5 and Table 6).

The SD of three different ROI measurements was recorded to represent the reproducibility error or operator error (see Equation 3). Figure 10 and Table 5 show the error bars representing the reproducibility error of three ROI measurements for each cardiac CT slice when the different breast implants were attached to the phantom and when no breast implant was attached (reference). The following equation calculates the re*producability error* within ROIs:

$$Reproducability\ error = \frac{Sd1 + Sd2 + Sd3}{3}, \qquad (3)$$

where:

Sd_1 = the standard deviation value measured from the first ROI

Sd_2 = the standard deviation value measured from the second ROI

Sd_3 = the standard deviation value measured from the third ROI

Table 5: The size of ROIs for all cardiac slices

Cardiac slices	Size of ROIs		
	Number of pixels		
	ROI$_1$	ROI$_2$	ROI$_3$
1	228.62	225.76	232.43
2	484.86	488.67	442.95
3	641.08	716.34	710.62
4	823.98	967.82	873.51
5	871.61	976.39	945.91
6	913.52	903.99	888.75
7	821.12	767.78	688.71
8	718.24	696.33	702.05
9	682.04	615.36	606.79

Table 6: Representation of the reproducibility error of the three ROI measurements for each cardiac CT slice

Breast implant size	Average whole cardiac slice (9 slices) CT HUs	Reproducibility error
Reference	1.63	0.90
Small	1.39	0.92
Medium	-2.02	0.58
Large	-3.12	0.56
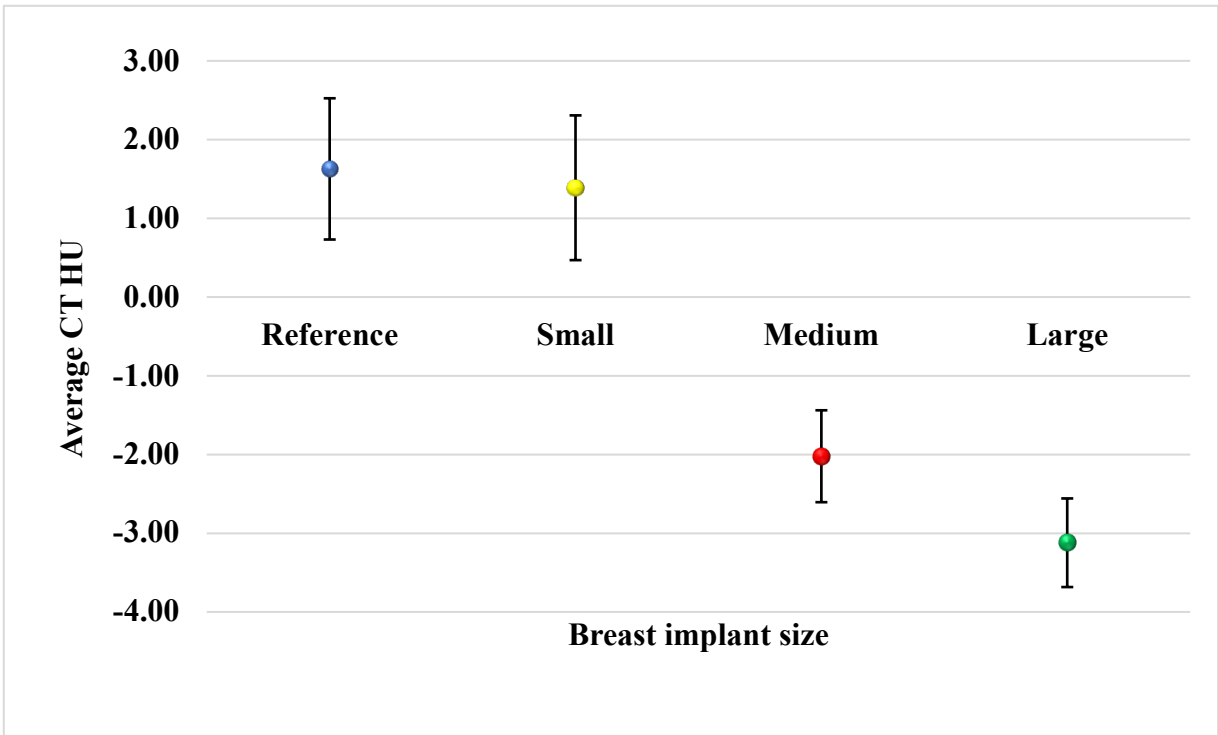
Figure 10: The reproducibility errors (operator errors) for each cardiac CT image for the reference and when the different breast implants are attached to the phantom.

3.7 Results of the Experiment

The results presented in this chapter focus on physical measures for image quality. The CT HUs, noise (SD of HUs) and the range of HU values of anthropomorphic LUNGMAN phantom CT images were measured using an ImageJ software analyser. The data demonstrate the effect of breast implant size on CT HU accuracy for the myocardium (LV) and the subsequent impact of the tube current (mA). Table 7 shows the mean CT HU, noise and range values in the cardiac ROI between the reference and small, medium and large breast implants of the cardiac region of the phantom at different tube currents.

Paired t-tests were performed to determine the statistical significance between the two subsets of the reference and individual breast implant size conditions. Charts were used to illustrate the differences between breast implant sizes in terms of the CT (HUs).

Table 7 shows the cardiac CT HU values among the images of all three breast implant sizes and the reference image when different tube currents were used. The highest CT HU value for the cardiac region was recorded for a reference image (1.64 HU), while the lowest CT HU was recorded for the large breast implant (-3.12 HU) with the 10 mA tube current.

Table 7: The measured cardiac CT HU values of the reference image for small, medium and large breast implants at 10, 20 and 30 mA and the values for statistical differences

Tube current (mA)	Measured cardiac CT HUs within ROIs when different breast implant sizes were attached						
	Reference	Small breast implants	Medium breast implants	Large breast implants	P-values (compared between reference and different breast implant sizes)		
					Small	Medium	Large
10	1.64	1.39	-2.02	-3.12	0.85	0.004	0.001
20	1.63	1.53	-1.85	-2.91	0.93	0.007	0.001
30	1.53	1.49	-1.75	-2.69	0.97	0.011	0.002

Statistically, no significant differences ($p > .05$) were found in cardiac CT HU values between when small breast implants were attached and the reference images for all three tube currents. However, significant differences ($p < .05$) were in cardiac CT HU values between when medium and large breast implants were attached and the reference images for all three different tube currents (see Table 7). The size of the breast implants was observed to have an impact on cardiac CT HU values, with the large breast implants having impact.

Figure 11 shows the cardiac CT HU values among the images of all three different breast implants and the reference image when the different tube currents were used. The line graph in Figure 11 shows a consistent trend, with cardiac CT HUs decreasing with increasing breast implant size. When the small, medium and large breast implants were attached, the cardiac CT HU values were 1.39, -2.02 and -3.12 HU, respectively, compared to 1.64 HU in the reference image with the low tube current (10 mA). Furthermore, with the highest tube current (30 mA), the small breast implant had the most negligible impact on cardiac CT HU values (1.49 HU) compared to the medium and large breast implants (-1.75 and -2.69 HU, respectively) and the reference image (1.53 HU; see Figure 11).

However, comparing the impact of different tube currents on cardiac CT HU values shows that increasing the tube current did not impact cardiac CT HU values when different breast implants were used (Figure 11). The line chart shows that the cardiac CT HU values when large breast implants were attached were at -3.12 HU at low tube currents (10 mA) and at -2.69 HU at the

highest tube current (30 mA). In addition, the cardiac CT HU values when the small breast implants were attached were 1.49 HU at the highest tube current and 1.39 HU at the lowest tube current. This shows that increasing the tube current did not impact cardiac CT HU (see Figure 11).There was a decrease in cardiac CT HUs for all other breast implant sizes relative to the reference.
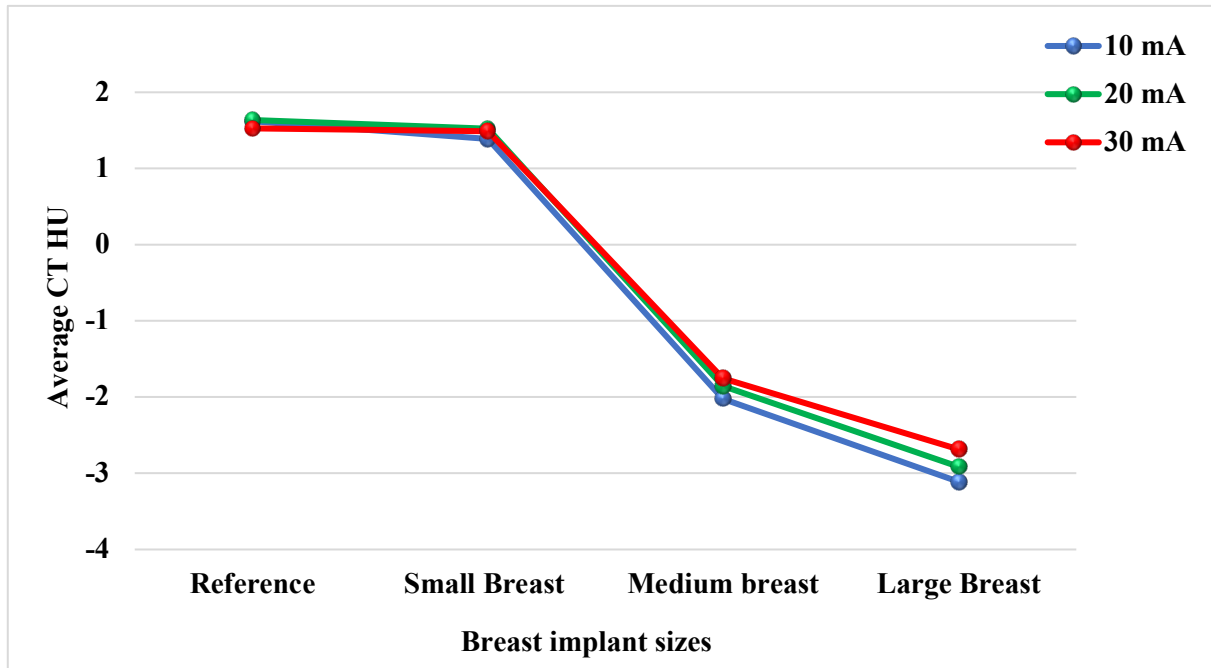
Figure 11: Cardiac CT HU values for reference images and attached breast implant images at three different tube currents.

Table 8 demonstrates the noise values within the cardiac region among all images for the three different breast implants and the reference when different tube currents were used. The highest noise values for the cardiac region were recorded for large breast implant images (12.03) at the low tube current (10 mA), while the lowest noise was recorded for the reference images (5.22) with the high tube current (30 mA).

Table 8: The measured noise values within the cardiac region of the reference image and when small, medium and large breast implants were attached at 10, 20 and 30 mA tube currents and statistical difference values

Tube current (mA)	Measured noise within ROIs						
	Reference	Small	Medium	Large	P-value (compared between reference and different breast implant sizes)		
					Small	Medium	Large
10	8.79	8.93	11.25	12.03	0.63	0.001	0.001
20	6.28	6.38	8.29	9.02	0.16	0.001	0.001
30	5.22	5.25	7.10	7.77	0.62	0.001	0.001

Looking at Figure 12, it is apparent that the noise value within the cardiac region of the reference image was the lowest and that large breast implants had the highest noise value compared to the reference images. The line graph in Figure 12 illustrates a consistent trend, with the noise values within the cardiac region increasing with increased breast implant size. By comparing the impact of the three different breast implant sizes on noise values within the cardiac region, the small breast implant had the least impact on noise values compared to the medium and large breast implants. The noise values within the cardiac region when the small, medium and large breast implants were attached were 8.93, 11.25 and 12.03, respectively, with the low tube current (10 mA), and high noise values were observed when the large breast implants were attached. Furthermore, with the highest tube current (30 mA), the small breast implants had the least impact on noise values (5.25) within the cardiac region compared to the medium (7.10) and large (7.70) breast implants (Figure 12).

Statistically, there was no evidence that the small breast implants had an influence on the noise values within the cardiac region, compared to the reference image for all three tube currents ($p < .05$; see Table 8). None of these differences were statistically significant. The noise value within the cardiac region when the small breast implants were attached at the low tube current (10 mA) was 8.93, whereas increasing the tube current to 20 or 30 mA decreased the noise to 6.38 and 5.25, respectively. However, there was a significant difference in the noise values within the cardiac region between the reference images and the medium and large breast implants for all tube currents ($p > .05$). The noise within the cardiac region when the large

breast implants were attached in the low tube current was 12.03, while the highest tube current was 7.77. There was a reduction in the noise value within the cardiac region when the tube current increased from 10 mA to 30 mA. The noise values within the cardiac region of the reference image showed the lowest noise for all tube currents, whereas the large breast implants had the highest noise values within the cardiac region. These findings illustrate that increasing tube current reduces image noise when all parameters, such as slice thickness and tube voltage, are constant. Furthermore, there was increased noise within the cardiac region when all three breast implants were attached relative to the reference.

However, the line graph shows an expected trend. Increasing the tube current reduced the noise values for all breast implant sizes. The noise values within the cardiac region of the phantom across the three breast implant sizes and the reference for the different tube currents are represented graphically in Figure 12.

Figure 12: The noise values within the cardiac region in scans with the reference and small, medium and large breast implants when using different tube currents.

Table 9 demonstrates the range (HU) values within the cardiac region among images for all three breast implants and the reference image when the different tube currents were used. The highest range (HU) value for the cardiac region was recorded for the large breast implant images (76 HU) with the low tube current (10 mA), while the lowest range (HU) was recorded for the reference images (33 HU) with the high tube current (30 mA).

Table 9: The measured range (HU) values for the reference image and the small, medium and large breast implants at 10, 20 and 30 mA tube currents

Breast implant size	Tube currents (mA)								
	10			20			30		
	Min	Max	Range	Min	Max	Range	Min	Max	Range
Reference	-28	30	58	-19	22	41	-15	18	33
Small	-28	33	61	-18	23	41	-16	19	3
Medium	-39	34	73	-27	23	51	-23	21	44
Large	-42	35	76	-33	24	58	-24	20	45

Figure 13 provides the range values of the CT HUs in the cardiac region among the reference images and the images for all three breast implant sizes when the different tube currents were used. There was an increase in range values of the CT HUs for all breast implant sizes. The graphs 13 illustrate an increase in range values with increased breast implant size compared to the reference. The large breast implant had the highest impact on range values within the cardiac region compared to the small and medium breast implants. The range (HU) values within the cardiac region when the small, medium and large breast implants were attached were 61, 73 and 76 HU, respectively, compared to the range (HU) values within the cardiac region of the reference image (58 HU) with the low tube current (10 mA). Furthermore, within the highest tube current (30 mA), the small breast implant attached had the most negligible impact on the range (HU) values within the cardiac region (35 HU) compared to the range (HU) values when the medium and large breast implants were attached (44 and 45 HU, respectively).

However, the line graph in figure 13 shows that, when the tube current increased, the range (HU) values within the cardiac region for all three breast implants decreased. The range (HU) value within the cardiac region when the small breast implants were attached at the lowest tube current (10 mA) was 61 HU, whereas increasing the tube current to 20 or 30 mA decreased the range (HU) value to 41 and 35, respectively. The range (HU) values within the cardiac region of the phantom across the three breast implant sizes and the reference for the different tube currents are represented graphically in Figure 13.
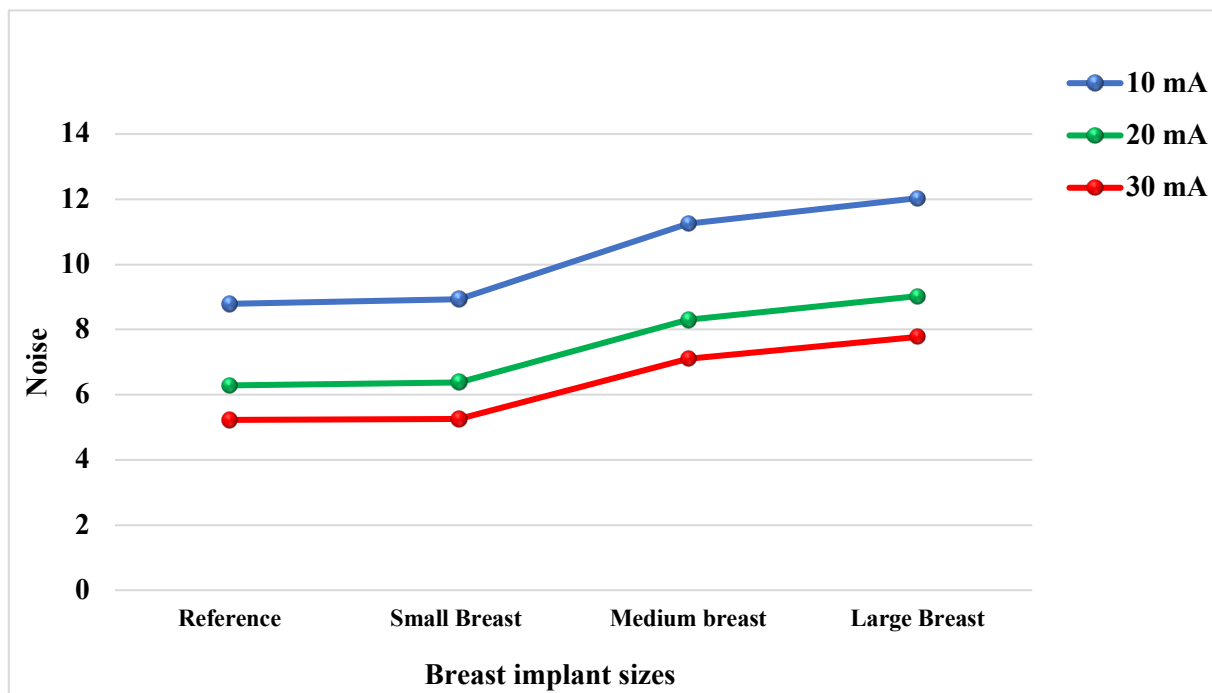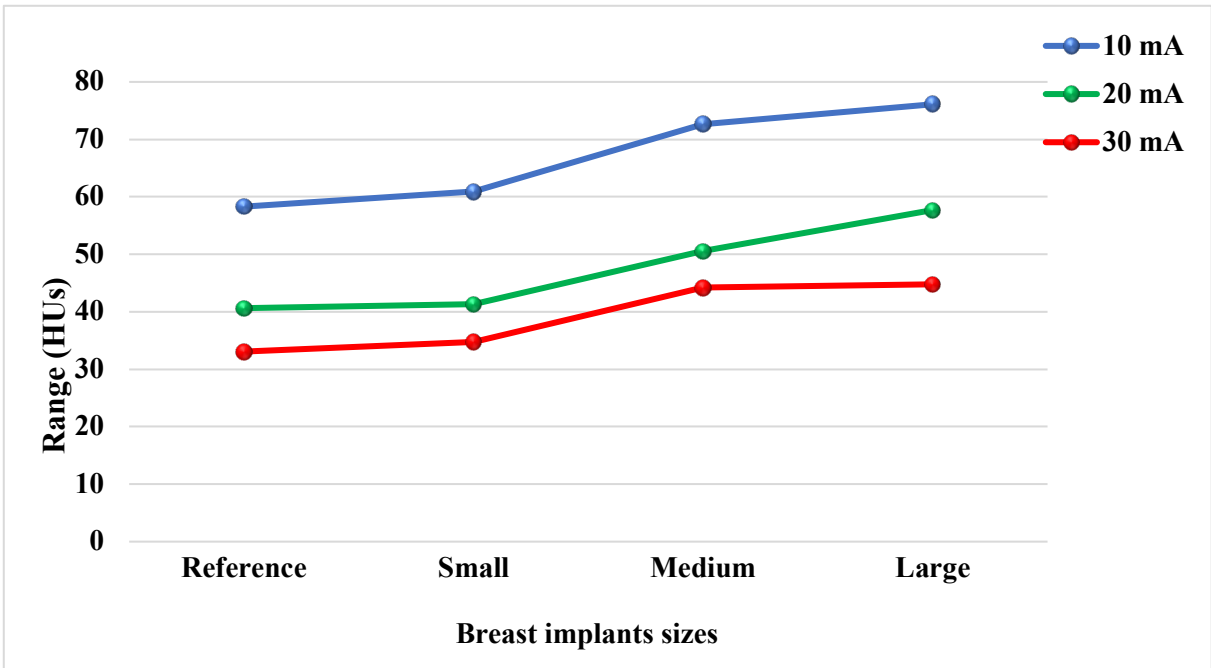
Figure 13: The range (HU) values within the cardiac region for the reference and small, medium and large breast implant images using different tube currents.

3.8 Assessment of the Impact of Different Breast Implant Sizes and Increased Tube Current on Accuracy of CT HUs Within the Cardiac Region of CT Images Using the Subtraction Technique

The average subtracted CT HU subtracted noise and range of subtracted CT HU values of anthropomorphic LUNGMAN phantom CT images were measured physically using the subtraction function within an ImageJ software analyser (Table 10).

Table 10: Mean differences in CT HUs, differences in noise and differences in range values in the cardiac ROI among the small, medium and large breast implants subtracted from reference images of the cardiac region of the phantom at different tube currents

Tube current (mA)	Subtraction (Breast implant size subtract reference)	Measurements		
		Difference in HUs	Noise	Range CT (HUs)
10	Small subtract reference	0.24	12.21	79
10	Medium subtract reference	3.65	13.83	88
10	Large subtract reference	4.75	14.81	95
20	Small subtract reference	0.11	8.800	57
20	Medium subtract reference	3.49	10.09	66
20	Large subtract reference	4.55	10.65	66
30	Small subtract reference	0.04	7.08	47
30	Medium subtract reference	3.28	8.25	51
30	Large subtract reference	4.21	8.92	53

Figure 14 illustrates the data showing the cardiac CT HU values of the phantom between the reference image data set and the images of the three different breast implant sizes by subtracting the images of the different breast implant sizes from the reference images when the tube currents were increased. The line in graph 14 shows a consistent trend, with an increase in the differences in cardiac HUs with increased breast implant size and decreasing tube current. The large breast implant had a greater difference in cardiac CT HUs from the reference image compared to the small and medium breast implants for all different tube currents. For the three tube currents, the differences in cardiac CT HUs within ROIs when the large breast implants

were attached were 4.75, 4.55 and 4.21, respectively, compared to when the small breast implants were attached (0.24, 0.11 and 0.04 HU, respectively) and when the medium breast implants were attached (3.65 and 3.49 and 3.28 HU, respectively). The difference in cardiac CT HUs within ROIs when the small breast implants were attached within the low tube current was 0.24 HU, compared to 3.65 and 4.75 HU, respectively, when medium and large breast implants were attached. Furthermore, within the highest tube current, the difference in cardiac CT HUs within ROIs when the small breast implant was attached was the least difference from the reference image (0.04 HU) compared to the medium and large breast implants (3.28 and 4.21 HU, respectively). An increasing trend in the difference in HUs from the reference image for breast implant sizes relative to size was demonstrated. For the CT number accuracy for water, the AAPM Task Group defined a tolerance of 5 HU. When this tolerance was applied to the experiment results, the mean CT numbers within the ROIs of the cardiac region when the three different breast implants were attached were all accurate, as the largest significant mean CT number difference was 4.75 HU at a low tube current (10 mA).

However, further analysis showed that an increase in the tube current led to a decreased difference in CT HUs within ROIs for all breast implant sizes. The line in chart 14 illustrates that, when the large breast implants were attached with low tube currents (10 mA), the difference in cardiac CT HUs within ROIs from the reference image was 4.75 HU, whereas it was 4.21 HU with the highest tube current (30 mA). However, when the small breast implants were attached and when the low tube current (10 mA) was used, the difference from the reference image in cardiac HUs within ROIs was 0.24 HU, while it was 0.04 HU when the highest tube current (30 mA) was used.
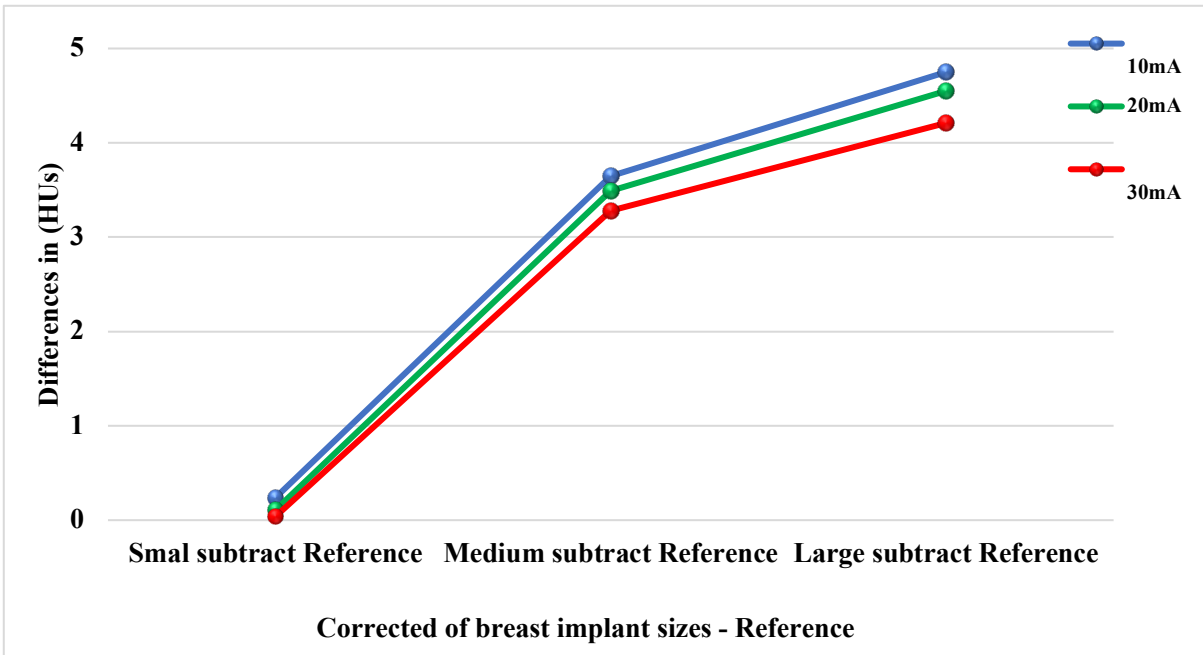
Figure 14: The average difference from the reference image in cardiac HUs within the ROIs for the reference image versus images with small, medium and large breast implants attached when using the three different tube currents.

Figure 15 demonstrates the average differences in noise within the ROIs of cardiac images when subtracting all three different breast implant images from the reference images when different tube currents were used. There was an increased difference in the noise within ROIs of the cardiac region for all breast implant sizes. When the breast implant size increased, the differences in noise also increased. The value of differences in noise was increased when the large breast implants were attached compared to differences in the noise value when the small and medium breast implants were attached. As shown in Figure 15, the results indicate an increase in differences in noise within ROIs of the cardiac region when different breast implant sizes were attached. The differences in noise within images when the small breast implants were attached showed the least differences in noise values compared to differences in noise within images of the medium and large breast implants, whereas the large breast implants showed the highest differences in noise values compared to the other breast implant sizes. The difference in noise within the ROIs when the large breast implants were attached and the low tube current was used was 14.81, while it was 8.92 with the highest tube current. There was an increase in differences in noise within ROIs when all breast implants were attached and a decreased noise value with increased tube currents. The differences in noise values within ROIs of the small breast implant images showed the least differences in noise for all tube currents,

whereas the large breast implants had the highest differences in noise values within ROIs. The graphs(15) show that increasing the tube current reduced the differences in noise values for all breast implant sizes.
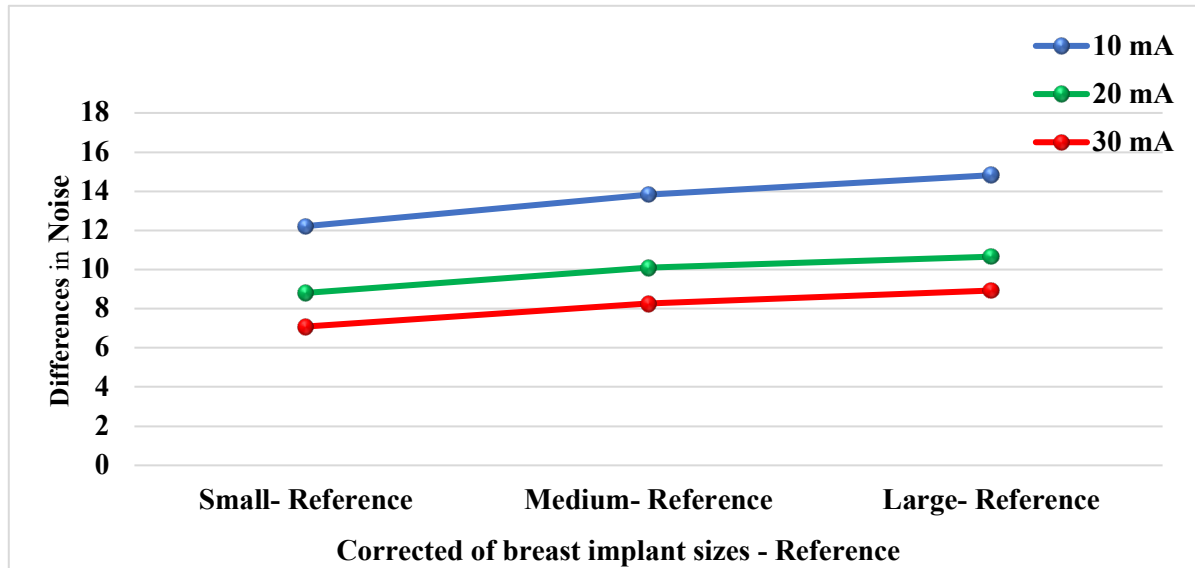
Figure 15: Average differences in noise within ROIs of cardiac images when all three different breast implant images were subtracted from the reference images when using different tube currents.

Figure 16 demonstrates the range of subtracted CT HUs within ROIs of cardiac images when all three different breast implant images were subtracted from the reference images and the different tube currents were used. The large breast implants had a greater difference in the range of subtracted CT HUs than the reference image compared to the small and medium breast implants for all tube currents. As can be seen in Figure 16, the difference in range within ROIs was 79 HU when the small breast implants were attached at the lowest tube current, whereas the differences were 88 and 95 HU, respectively, when the medium and large breast implants were attached. The difference in range within ROIs was 53 HU when the large breast implants were attached at the highest tube current (30 mA), whereas decreasing the breast implant size to small or medium decreased the difference in the range to 47 and 51 HU, respectively (Table 11).

Figure 16 shows that increasing the tube current reduced the differences in the range values within ROIs for all breast implant sizes. The differences in range value within ROIs when the small breast implants were attached at the lowest tube current (10 mA) was 79 HU, whereas increasing the tube current to 20 or 30 mA decreased the difference in the range to 57 and 47 HU, respectively.

Table 11: Measured range (HU) values when subtracting images of all three breast implant sizes from the reference images at tube currents 10, 20 and 30 mA

Subtraction (Breast implant size subtract reference)	Tube currents (mA)								
	10			20			30		
	Min	Max	Range	Min	Max	Range	Min	Max	Range
Small subtract reference	-39	40	79	-27	30	57	-23	24	47
Medium subtract reference	-50	38	88	-38	28	66	-28	23	51
Large subtract reference	-53	42	95	-37	29	66	-30	23	53

The mean differences in the range (HUs) within the ROIs of the cardiac region of the phantom across the three breast implant sizes and the reference for different tube currents are represented graphically in Figure 16.
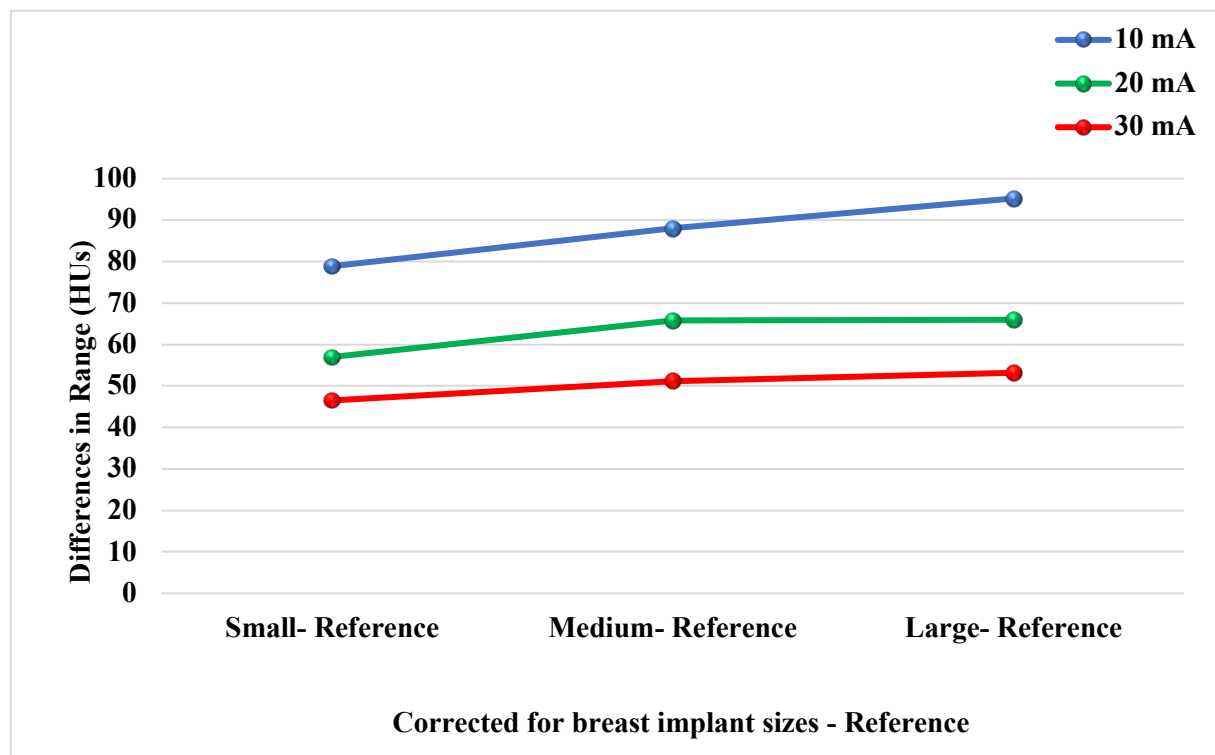
Figure 16: The differences in the range of the subtracted HU values in the cardiac ROIs when images of small, medium and large breast implants are subtracted from reference images when using different tube currents.

3.9 Discussion

If an implant is present in the region to be scanned, artefacts can be produced. Artefacts can be defined as any distortion or error in the image that can cause a decrease in image quality. Some of these artefacts are created because of a phenomenon referred to as beam hardening. This phenomenon can be produced when the X-ray beam travels through an object and the low-energy photons are absorbed more than the high-energy photons. High-density objects can generate beam hardening (Esmaeili, Johari, Haddadi, & Vatankhah, 2012)**.**

The current study shows that adding breast implants can impact CT HU within the cardiac region. The effect of different breast implant sizes on the CT HU values within the cardiac region of the phantom was found to be statistically significant for medium and large breast implants ($P < 0.05$), but not for small breast implants ($P \geq 0.05$) when compared to the reference images. The average CT HU of the cardiac region within the ROIs when small breast implants were attached was not statistically significant compared to the mean CT HU within ROIs of the reference ($P = 0.85$, $P = 0.93$; $P = 0.97$, respectively) using three different tube currents (Table 7).

Furthermore, when the subtraction technique was used, the results showed that the large breast implants had a greater difference in cardiac CT HUs from the reference image compared to the small and medium breast implants for all tube currents. The differences in cardiac CT HUs within ROIs when the large breast implants were attached were 4.75, 4.55 and 4.21 HU, respectively, while the values for the small breast implants were 0.24, 0.11 and 0.04 HU, respectively, and for the medium breast implants were 88 and 66 and 51 HU, respectively, for all three tube currents. Because the position of large breast implants might cover more of the cardiac region that the photon travels, it will be attenuated more than small breast implants.

The size of an object can impact CT HU accuracy. Beam hardening can impact CT numbers and lead to CT attenuation value shifts. The results of this study indicate that the size of the breast implants decreases CT HUs. When the high tube current (30 mA) was used, the CT HUs within the cardiac region were 1.49 and -2.69 HU, respectively, when large breast implants and small breast implants were attached, compared to 1.53 HU for the reference (Figure 11). However, Figure 14 demonstrates that, when the large breast implants were attached, the CT HU differences were 4.21 HU at 30 mA, compared to 0.04 HU when small breast implants were attached. The results show that breast implants can impact CT HUs, which, in turn, impact the CT images.

The current results are in agreement with Stinis et al.'s (2006) findings showing that breast implants cause increased attenuation artefacts. Stinis et al. analysed SPECT images for three female patients with breast implants. The results showed that breast implants cause a moderate anterior wall perfusion defect. Depending on the partial or complete coverage of the cardiac region by breast implants during image acquisition, a defect can be seen as partial or completely reversible. Silicone breast implants can create significant attenuation artefacts during SPECT imaging, making the diagnosis of CAD in females more challenging (Stinis et al., 2006).

Different implants used in clinics to treat patients, such as pacemakers, can cause artefacts and might obscure essential diagnostic information in CT images (Boas & Fleischmann, 2011). Pacemakers have lead, which tends to produce streak artefacts (Kikuchi et al., 2020). Pacemakers can cause beam-hardening artefacts in CT cardiac imaging, which can limit diagnostic evaluation. The pacemaker is commonly made of titanium with atomic number 22, which is higher than silicone atomic number 14. Thus, materials with high atomic numbers can cause strong metal artefacts in CT. DiFilippo and Brunken (2005) evaluated images of 15 patients who had cardiac devices, such as a pacemaker. The results revealed that pacemakers prevented a valid interpretation of images in up to half of the patients. Streak artefacts occurred by the pacemaker near the myocardium (DiFilippo & Brunken, 2005).

Overall, the current study found that there was no large variation of average CT HU values of the cardiac region between the reference and various breast implant sizes within the cardiac phantom. In addition, it can be noted that the CT HU values of the cardiac region decrease when breast implants are attached. Because the breast implants are made of silicone with atomic number 14, beam hardening can happen when the X-ray travels between the tube and detector when the phantom is scanned with attached breast implants. Thus, the beam becomes harder and causes a reduction in attenuation, leading to a decrease in the CT HUs. The average CT HU values of the cardiac region show that there is a significant difference between both medium and large breast implant sizes compared to the reference, whereas small breast implant sizes do not show significant differences in CT HU values compared to the reference. However, the differences were less than 5 HU.

This study reveals that increasing the tube current can decrease CT HUs for large breast implants. When large breast implants were attached, the CT HUs within the cardiac region were -3.12 HU with the low tube current and -2.69 HU with the high tube current (see Figure 11). However, Figure 12 demonstrates that the noise values decreased among all three breast implants when the tube current increased. When large breast implants were attached, the noise value was 12.3 with the low tube current and 7.7 with the high tube current. Furthermore, when

small breast implants were attached, the noise value was 8.93 with the low tube current and 5.25 with the high tube current. In accordance with the present results, previous studies have demonstrated that an increase in tube current decreases the noise value but does not impact CT HUs. Tang et al. (2012) studied the impact of an increased tube current on CT HUs and noise. The study found a significant impact of increased tube current from 150 to 300 mA on phantom image noise; the noise was reduced by almost 30% in phantom image noise values when the tube current was doubled (5.10 and 3.61 HUs, respectively). Using a low tube current increased image noise caused by the reduced photon flux. However, the value of CT HUs was not impacted when the tube current was increased; there was no large variation in phantom CT HUs when the tube current increased by double (56.12 and 56.76 HU, respectively; (Tang et al., 2012).

Among the noise artefacts, beam-hardening artefacts were identified as the most noticeable artefacts caused by high-density objects in the beam. CT noise is based on detector efficiency and the number of photon incidents on the detector. CT image noise increased with phantom size. Because the phantom does not have the same anatomical and body composition as humans, the phantom's noise is less than the noise in real patients. Figure 12 shows that attached large breast implants increased the noise compared to small and medium breast implants. The current study found that increased breast implant size led to increased noise values. The noise value when the large breast implants were attached was 12.3 with the low tube current, whereas the noise value when the small breast implants were attached was 8.93 with the same low tube current values. These results agree with the findings of other studies, which have found that increasing the diameter of a phantom's water size from 3 to 7 inches leads to increased noise from 3 to 8, respectively. However, the current study also illustrated that increasing tube current leads to decreased noise Figure 12. These results are consistent with those of Hilts and Duzenli (2004), who found that increasing the tube current from 100 mA to 200 mA reduced the noise from 6 to 4(Hilts & Duzenli, 2004).

3.10 Conclusion

Experimentation at this stage was carried out on a non-clinically based diagnostic CT system. This was done to allow the method to be tested and refined before being used on a clinical SPECT-CT system, which is in high demand in clinical settings. Measurements were taken using two image analysis methods: LV cardiac as ROIs in images without the subtraction technique and LV cardiac as ROIs in images after using the subtraction technique. The outcome

of the study will determine whether there are differences in the CT HUs of the selected cardiac region between the three different breast implant sizes.

Comparing the results of the two techniques illustrates that the subtraction approach is more sensitive to detecting differences in CT HUs within ROIs of the cardiac region. The CT HUs of the cardiac region when the large breast implants were attached with the high tube current was -3 HU, whereases the differences in HUs from the reference of the same cardiac region when the large breast implants were attached with the high tube current was 4 HU. However, the results for the cardiac region range of HUs using the technique without subtraction when the large breast implants were attached with the highest tube current was 45 HU, while after carrying out the subtraction approach, the cardiac range of HUs when the large breast implants were attached with the highest tube current was 53 HU.

This experiment shows that the large breast implants had a higher range of HUs within ROIs in the cardiac region than small and medium breast implants compared to the reference when the three different tube currents were used. The findings showed that large breast implants had 4 HU in differences within ROIs of the cardiac region compared to the reference when the different tube currents were used, whereas the small and medium breast implants had 1 HU and 3 HU, respectively, compared to the reference when the three different tube currents were used.

Data collected within this experiment revealed no significant differences in the CT HU values of the cardiac region within ROIs between the reference and the three different breast implants for all tube currents. Statistically, there was a non-significant difference in the average CT HU values between the three tube currents ($P>0.5$). The findings show that increasing the tube current improves the CT HUs accuracy; however, increasing the tube current above 20 mA does not impact the accuracy. Thus, a tube current above 20 mA will increase the patient dose without improving CT HUs accuracy. However, the large breast implants had a greater difference in range of subtracted CT HUs of the cardiac region of the phantom within ROIs when the three tube currents were used within both image analytical techniques.

The findings led to testing the method within the clinical SPECT-CT system to assess the impact of breast implants (with three different sizes) and increasing tube currents on the CT HU accuracy of the CT attenuation map. Inaccuracy of the CT attenuation map leads to inaccurate SPECT image diagnosis or interpretation due to incorrect absolute activity of the tracer.

Chapter 4: Second Experiment: Evaluation of the Impact of Breast Implants on the Accuracy of the CT Numbers of the Myocardium in the CT Attenuation Map in SPECT/CT Scanner: A Phantom Study

The first experiment found that the subtraction method was sensitive enough to demonstrate CT HU changes and showed that breast implants can have an effect on CT HUs, with the largest implants having the biggest impact. The next experiment demonstrated whether this finding could be reproduced clinically using a SPECT/CT scanner.

The experiment using the SPECT/CT scanner took place at Manchester Royal Infirmary using a SPECT/CT scanner (Discovery NM/CT 640, GE Healthcare, Milwaukee, Wisconsin, USA) and a LUNGMAN phantom. This experiment aimed to investigate the impact of breast implants and different tube currents on CT number accuracy on the CT attenuation map produced by the CT component of the SPECT/CT scanner. To achieve this aim, the following objectives were devised:

- To establish a reference image data set without breast implants at each tube current (10, 20 and 30 mA).

- To assess the impact of breast implant size on the accuracy of CT numbers on the CT attenuation map within the cardiac region of the LUNGMAN phantom.

- To assess the impact of the increased tube current on the accuracy of CT numbers within the cardiac region in the CT attenuation map produced by the CT component of the SPECT/CT scanner.

4.1 Materials and Equipment

Data were acquired using three different tools: the CT component of a clinically used SPECT/CT scanner, a LUNGMAN phantom and three different sizes of silicone breast implants (small, medium and large).

4.1.2 CT Component in SPECT/CT Equipment

This study was performed using a SPECT/CT dual-head system (Discovery NM/CT 640, GE Healthcare, Milwaukee, Wisconsin, USA). The CT component of the SPECT/CT scanner specifications is described in Appendix II. The standard protocol with the one-bed position was used with three different tube currents (10, 20 and 30 mA) to acquire data. The CT attenuation

map data were acquired with the controlled parameters to mimic local clinical protocol, shown in Table 12.

Table 12: Scan parameters used during CTAC protocols

Protocol	CT Parameters
kVp	120
Tube Current (mA)	10, 20 and 30
Rotation time (s)	1.00
Pitch	0.75
Image thickness (mm)	5
Field of view (FOV)	4.9 cm
Scan length (mm)	400

The CT attenuation map was reconstructed with the controlled parameters, as listed in Table 13.

Table 13: Scan parameters used, reconstructed in the CT attenuation map

Protocol	Reconstruction parameters
Matrix size	64×64
Number of slices	64
Reconstructed slice thickness (mm)	5
Reconstruction algorithms	Iterative reconstruction (IR)

The local clinical protocol in the centre where the experiment was done was used 30 mA, and the literature review shows that protocols can vary, but it is recommended to use 10 or 20 mA for acquiring CT a attenuation map within MPI (Camoni, Santos, Attard, Mada, Pietrzak, Rac, Rep, Terwinghe, & Costa, 2020).So three different tube currents (10, 20 and 30 mA) were used to assess the impact of tube current on the accuracy of the CT attenuation map. A standard clinical imaging protocol was used; the phantom was in the supine bed position with feet first, while the height of the table was 90 cm. CTAC was used to compensate for the attenuated photons and anatomic localisation. Using a high tube current may improve CT image quality, but the radiation dose to the patient will be increased because of an increasing number of photon flux. However, high-quality anatomic details are not required in myocardial perfusion SPECT imaging; thus, there is no need to increase the tube current for this purpose. CT noise increases linearly as the tube current decreases, but the increase in noise does not change the diagnostic information of the CT attenuation image (Kumar, Pandey, Sharma, Malhotra, & Kumar, 2012).

Furthermore, the literature review recommends using the 10 or 20 mA tube current for AC to decrease radiation exposure to the patient (Dorbala et al., 2018b).

4.1.3 Anthropomorphic Phantom and Breast implants

The same anthropomorphic phantom and three different implants (small 240 g, medium 490 g and large 685 g) that were used in Experiment 1 were used in this experiment (see Sections 3.3.2 and 3.3.3).

4.1.4 Experimental Set-up

The adult chest phantom (LUNGMAN) was placed in the supine position in the centre of the SPECT/CT gantry according to standard protocols for MPI. Three sizes of breast implants were used with the adult LUNGMAN chest phantom, which were the same breast implants as those used in the first experiment. The breast implant was placed on the anterior thoracic wall of the phantom, corresponding to the space between the second rib and above the sixth rib. Immediately, local clinical protocols for CTAC were performed on the same system.

4.2 Procedures for Acquiring the Images

The LUNGMAN phantom was scanned under the following conditions:

- without a breast implant as a reference using a range of tube currents (10, 20 and 30 mA);

- with left and right small breast implants attached using a range of tube currents (10, 20 and 30 mA);

- with left and right medium breast implants attached using a range of tube currents (10, 20 and 30 mA); and

- with left and right large breast implants attached using a range of tube currents (10, 20 and 30 mA).

4.3 Image Analysis – Subtraction Technique

The subtraction method was applied to assess the CT number inaccuracy that may arise due to the introduction of breast implants within CTAC images of the cardiac region of the phantom. The subtraction technique involves a subtraction calculation between the experimental condition images (when breast implants were attached with different sizes) and the reference images (no breast implants attached) for each tube current.

There were three reference images, one for each tube current; then, small, medium and large breast implants were compared to the reference at each tube current. The differences in HUs, differences in noise and differences in range values of HUs among all breast implants were measured from the resultant subtracted images to assess the impact of breast implant sizes on the accuracy of the CT number within the cardiac region of the phantom.

4.4 Full-Width Half Maximum (FWHM) Method

In this experiment, the cardiac CT images were reconstructed using the CTAC protocol, and a matrix size of 64 x 64 was used to match the SPECT data that are usually acquired. The matrix size of 64 x 64 (compared to 512 x 512 of the data set in Experiment 1) meant there was poor spatial resolution, and therefore, the edges of the ROI could not be defined accurately from the images. In practice, it was not clear whether the pixels were within the LV region because large pixels within the matrix size lead to a loss of anatomical detail. The identification of the LV within these images was challenging and led to significant errors and poor reproducibility. To overcome the problem of large pixels, the full width half maximum (FWHM) method was used to define the ROI edges. FWHM is a method utilised to define the measurement of the width of an object in an image that does not have sharp edges.

FWHM values were obtained using ImageJ software to plot a horizontal line profile across the centre of the cardiac region of the non-subtracted images (Figure 17). The plot profiles measured all the voxel values along the plotted line.

The following equation was then used to calculate the FWHM values for each slice that included the cardiac region in each set of images:

$$FWHM = \frac{Max - Min}{2}, \quad\quad\quad (3)$$

where:

FWHM = full width half maximum to define the edge of the cardiac region within the phantom

Max = the maximum voxel value measured from the line profile

Min = the minimum voxel value measured from the line profile
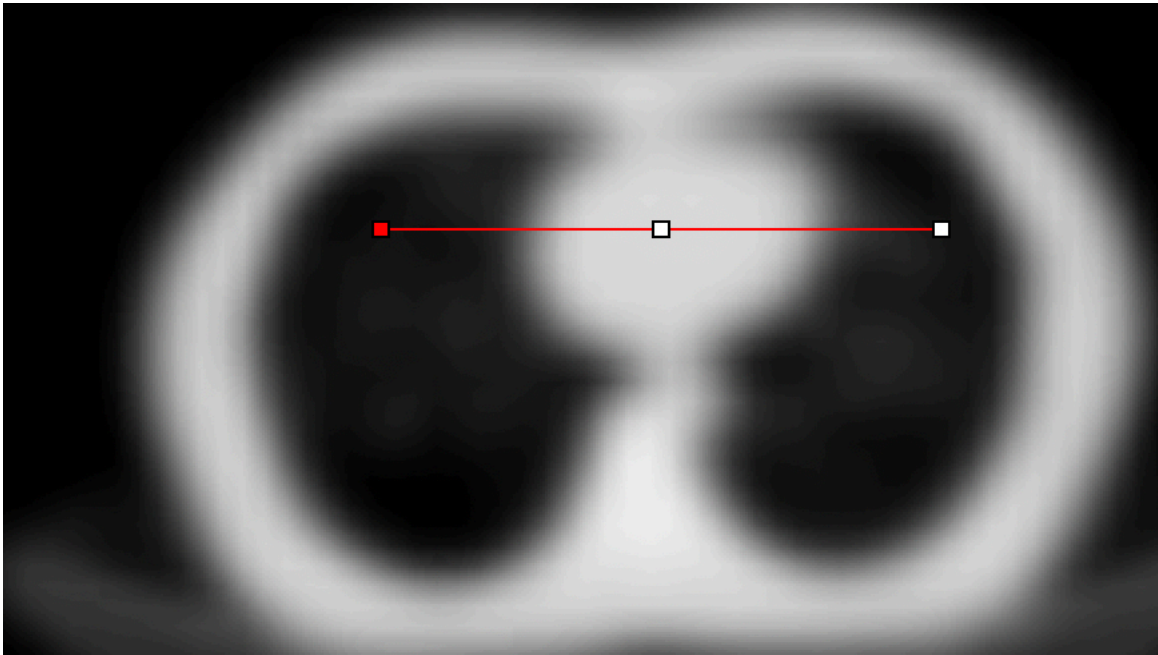
Figure 17: Line profile drawing for the whole cardiac region

The FWHM value was used as a threshold value to define the edges of the ROI. Any voxels less than FWHM values were not included within the ROIl therefore, the edges were defined. The ROIs were drawn based on the threshold voxel value. The ROI was defined once for each slice on each of the three reference image sets from the phantom to ensure that any influence caused by the breast implants was removed. Then, the ROIs were applied across all the subtracted image sets for consistency. The ROI manager function within ImageJ was used to save and apply the ROIs to improve the reliability of the results.

For each ROI, the differences in the CT number, differences in noise (SD in HUs) and differences in range values of HUs within ROIs were measured per slice. The data were then averaged across all slices within the cardiac region for each subtracted image set. These variables were measured to assess the impact of breast implant size on the accuracy of the CT number.
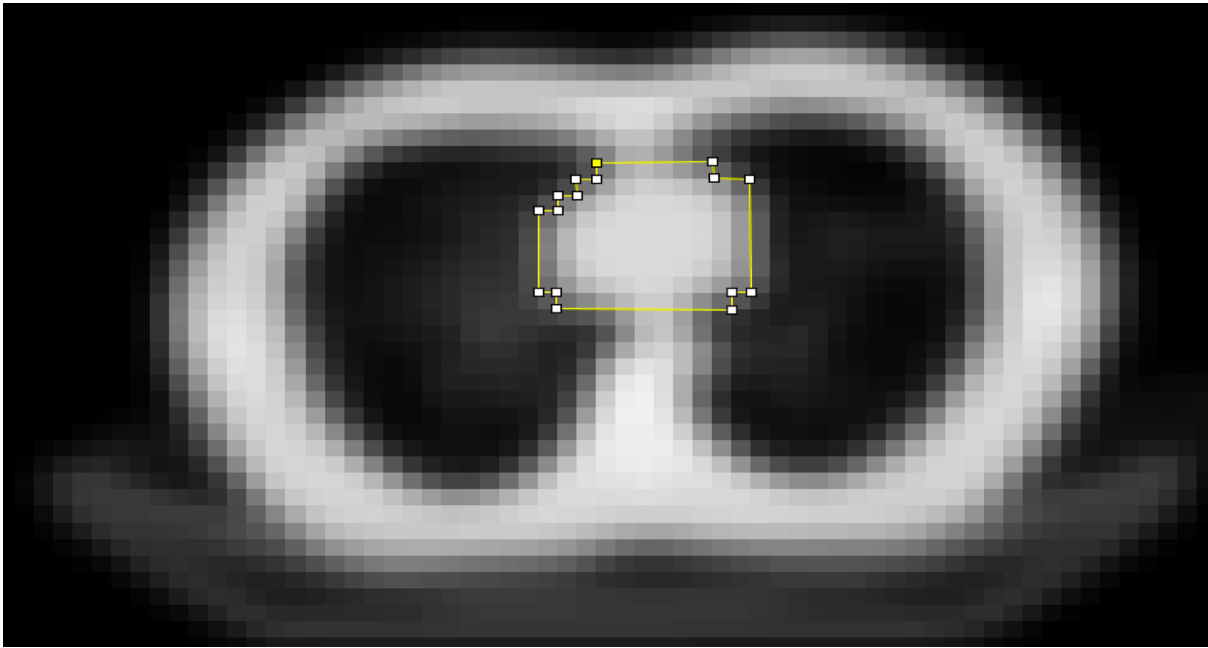
Figure 18: The ROI drawing for the entire cardiac region.

4.5 Results

Excel 2013 (Microsoft Inc, Redmond, WA) was used to evaluate the data. The descriptive statistics were analysed using Excel; the graphs were also created in Excel to illustrate and describe the collected results. Differences in CT number, differences in noise and differences in the range of HUs were measured from the resultant subtracted images. However, as the subtraction method was used, the data had already been compared to the reference. Therefore, inferential statistics were not possible. Although comparisons could be made between small, medium or large breast implants, this was not deemed appropriate, as clinically, individual patients would not have different implant sizes.

Table 14: The measured difference in CT number values when images of all three breast implant images were subtracted from reference images using all tube currents (10, 20 and 30 mA)

Subtraction (Breast implant size subtract reference)	Tube currents (mA)		
	Difference in CT numbers		
	10	20	30
Small subtract reference	0.18	0.15	0.12
Medium subtract reference	0.38	0.27	0.22
Large subtract reference	0.46	0.33	0.27

Figure 19 illustrates the data, showing the differences in cardiac CT number values of the phantom when subtracting the images of all three breast implant sizes from the reference images and the three different tube currents were used. Figure 19 shows the consistent trend of increased differences in cardiac CT numbers within ROIs when breast implant size increased and tube current decreased. The findings showed that, using all three tube currents, there was a bigger difference in CT numbers with large breast implants, whereas the least difference in CT numbers was found with small breast implants (see Table 14). The differences in cardiac CT numbers within ROIs when the large breast implants were attached were 0.46, 0.33 and 0.27 HU, respectively, among all three tube currents (10, 20 and 30 mA), compared to when the small breast implants were attached (0.18, 0.15 and 0.12 HU, respectively) and when medium breast implants were attached (0.38, 0.27 and 0.22 HU, respectively).. However, the graph 19 shows that the increase in the tube current leads to a decreased difference in CT number within ROIs in the cardiac region when the different breast implant sizes are attached. The line chart 19 shows that the difference in cardiac CT number within ROIs when the large breast implants were attached with the low tube current (10 mA) was 0.46 HU, whereas it was 0.27 HU with the high tube current (30 mA). In addition, the difference in cardiac CT number within ROIs when the small breast implants were attached was 0.12 HU with the high tube and was 0.18 HU with the low tube current.
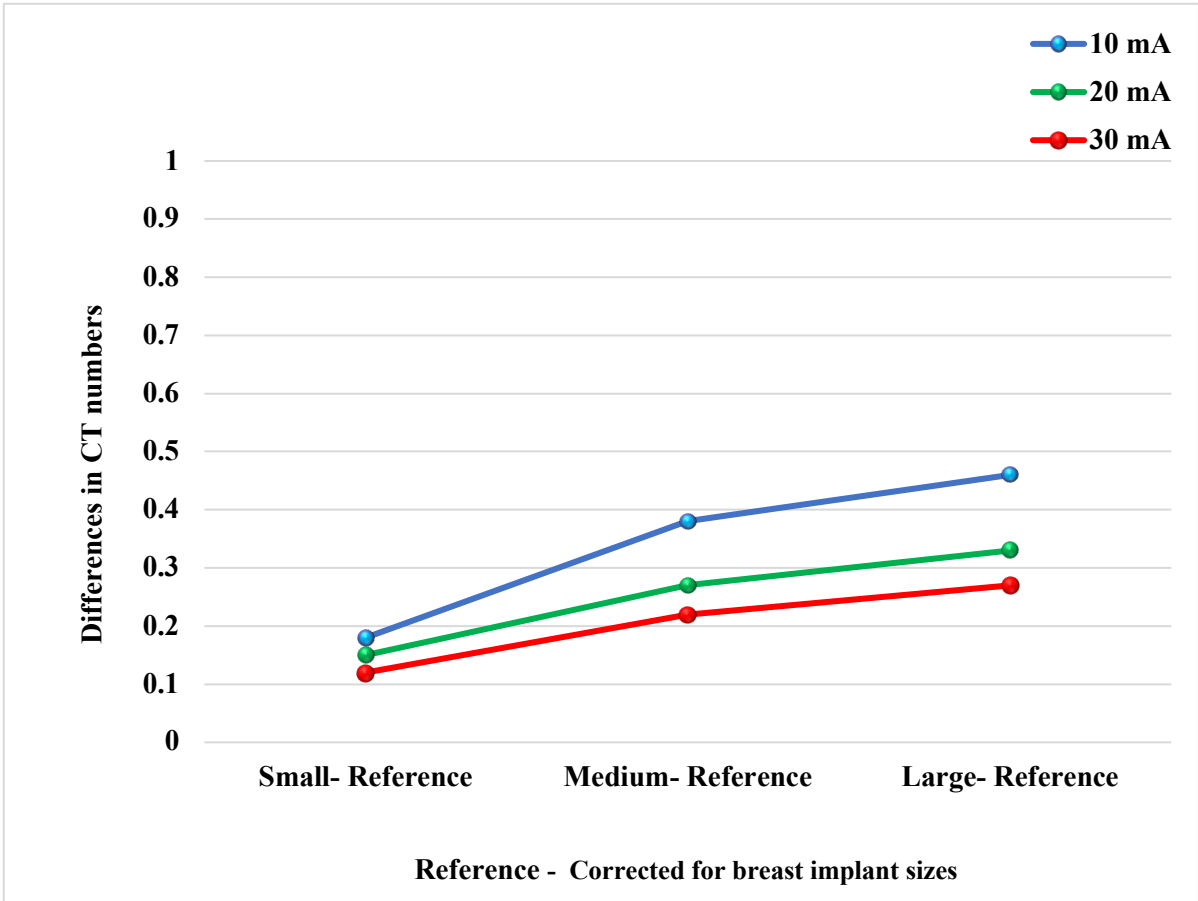
Figure 19: The average of differences in subtracted CT number within ROIs in scans with reference image with no breast implant versus small, medium and large breast implants (subtracting breast implant image from reference) when using the three different tube currents.

Table 15: The measured difference in noise values when subtracting images of all three breast implant sizes from reference images with all tube currents (10, 20 and 30 mA)

Subtraction (Breast implant size subtract reference)	Tube currents (mA)		
	Difference in SD HU		
	10	20	30
Small subtract reference	0.94	0.78	0.70
Medium subtract reference	1.12	0.98	0.92
Large subtract reference	1.40	1.2	1.1

Figure 20 demonstrates the data showing the average difference in noise in the cardiac region between the reference image data set and the different breast implant size images by subtracting the images of all three different breast implant sizes from the reference images

when the three different tube currents were used. There was an increase in difference in noise within ROIs when the different breast implant sizes were attached (see Figure 20 and Table 15).

The difference in noise value within ROIs when the small breast implants were attached in the low tube current (10 mA) was 0.94, whereas increasing the tube current to 20 or 30 mA decreased the difference in noise to 0.78 and 0.70, respectively. Furthermore, the difference in noise within the ROIs was 1.4 when the large breast implants were attached and the low tube current was used, while the same value was 1.1 when the large breast implants were attached and the high tube current was used. Figure 20 shows that increasing the tube current reduced the noise values within the ROIs. The difference in noise within the ROIs when the small breast implants were attached showed the lowest values (0.94) compared to medium and large breast implant images (1.12 and 1.40, respectively, while the difference in noise within the ROIs when the large breast implants were attached showed the highest values (1.4) when the low tube current was used. In addition, the large breast implants had the maximum difference in noise values within ROIs (1.1) in the highest tube current compared to the medium and small breast implants (0.92 and 0.7, respectively). Figure 20 shows that increasing the tube current reduced the difference in noise values within ROIs for all breast implant sizes.

Figure 20: The average difference in subtracted noise values in cardiac ROIs in scans where images of small, medium and large breast implants are subtracted from references images when using different tube currents.

Table 16: The measured average differences in the range of CT number values when images of all three breast implant sizes were subtracted from reference images using (10, 20 and 30 mA) tube currents.

Subtraction (Breast implant size subtract reference)	Tube currents (mA)								
	10			20			30		
	Min	Max	Range	Min	Max	Range	Min	Max	Range
Small subtract reference	-2.44	1.56	3.60	-1.78	1.22	3.00	-1.56	1.33	2.89
Medium subtract reference	-3.33	1.44	4.30	-1.89	2.00	3.89	-1.67	1.89	3.56
Large subtract reference	-3.89	2.44	6.33	-3.22	2.11	5.33	-2.89	1.89	4.78

Figure 21 demonstrates the range of CT numbers in cardiac ROIs among all three breast implants images subtracted from the reference image. There was an increase in the range of CT numbers when different breast implant sizes were attached. The line graph 21 illustrates that the range of the CT number increased within the ROIs as the breast implant size increased. From this data, we can see that differences in the range of the CT number within ROIs when the small breast implants were attached resulted in the lowest value of difference (3.6 HU) compared to medium or large breast implants (4.3 and 6.3 HU, respectively) when the lowest tube current was used. Moreover, the data show that the difference in the range of CT numbers within ROIs when small breast implants were attached had the minimum difference in the range of subtracted CT numbers (2.89 HU) when the highest tube current was used compared to the difference in the range of subtracted CT numbers of medium or large breast implants (3.56 and 4.78 HU, respectively) in the same tube current.

Also, the graph 21 shows that increasing the tube current reduced the difference in the range of the CT number within the ROIs when the different breast implants were attached. The difference in range of CT numbers within ROIs when the large breast implants were attached in the low tube current was 6.3 HU, whereas it was 4.78 HU in the highest tube current. The mean difference in range of CT numbers in the cardiac region of ROIs of the phantom across

the three breast implant sizes (small, medium and large implants) subtracted from the reference for different tube currents are represented graphically in Figure 21.
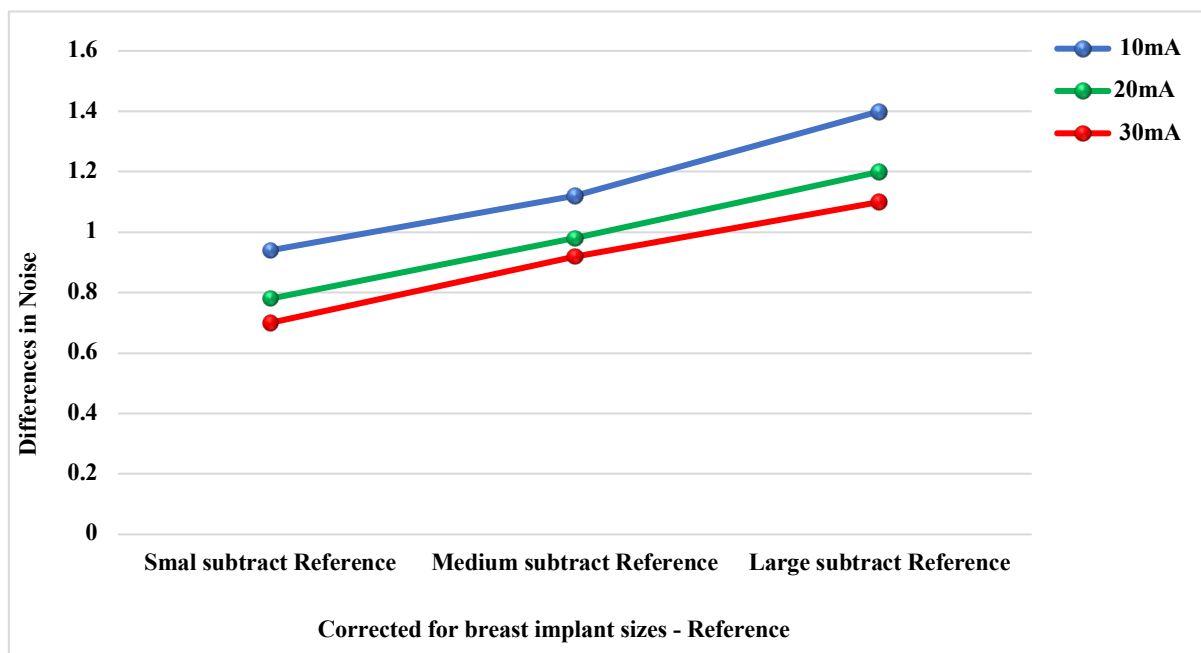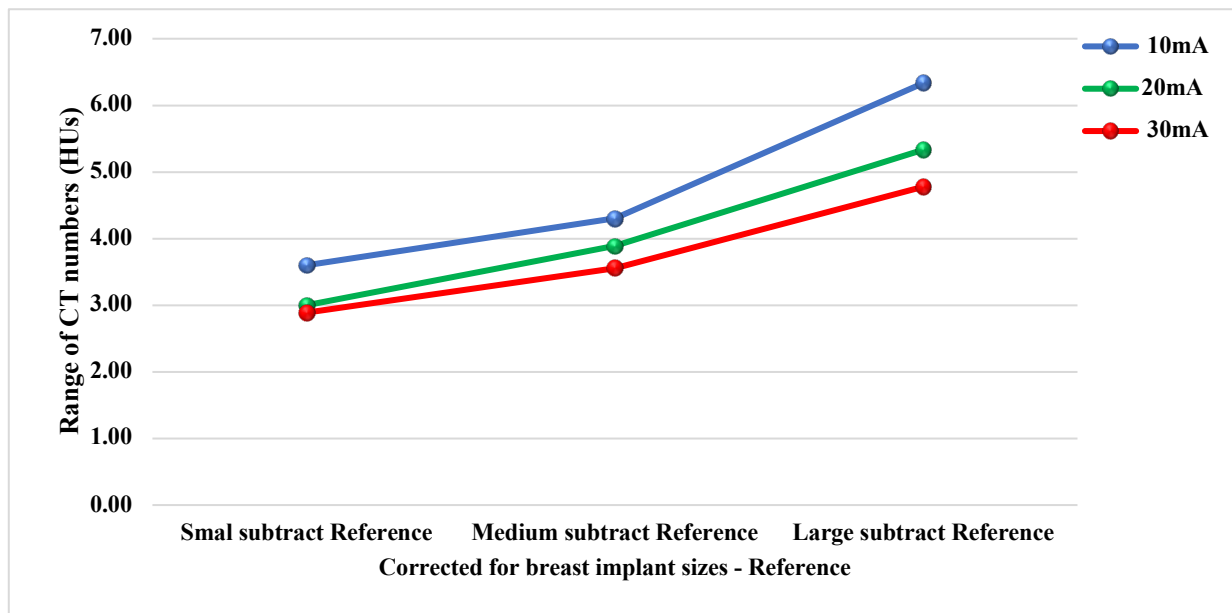

Figure 21: The average differences in the range of subtracted CT numbers in cardiac ROIs in scans where images of small, medium and large breast implants are subtracted from references images when using different tube currents.

4.6 Discussion

CTAC can lead to overcorrection caused by implants. Due to the presence of highly attenuating objects, such as implants, the photoelectric absorption of X-rays occurs, and streak artefacts in reconstructed CT images can be seen (Abdoli, Ay, Ahmadian, & Zaidi, 2010). These may be associated with incorrect HUs and, hence, the estimated attenuation map (μ-map) and reconstructed SPECT/CT images might also be impacted (Zaidi, Montandon, & Alavi, 2007). Attenuation maps must be accurate; otherwise, they could over- or undercorrect the emission data. However, the variation of the CT numbers from specified values within the CT scanner component in SPECT/CT scanner is ± 10 HU for water and ± 20 HU for other materials (Rep, Attard, Camoni, & Santos, 2017).

The present study was designed to determine the effect of breast implants with three different sizes and a different tube current on the accuracy of CT number on the CT attenuation map produced by the CT component of the SPECT/CT scanner. The current study found that the mean differences in subtracted CT numbers for three breast implants from reference images were 0.18, 0.38 and 0.46 HU for small, medium and large implants, respectively, for the low tube current and 0.12, 0.22 and 0.27 HU, respectively, for the high tube current (see Figure 19).

The mean differences in subtracted CT numbers within ROIs in this study did not significantly impact CTAC images.

An image subtraction technique was used to analyse the data within the ROIs. Figure 19 illustrates the average difference in subtracted CT numbers of cardiac within ROIs for three different breast implant sizes across all tests (different tube currents). The results show that the CT number for ROIs is decreased for each of three different breast implant sizes compared to the reference, while the differences in cardiac CT numbers among the three different breast implant sizes compared to the reference across various tube currents were within (± 5 HU; see Table 14). These results seem to be consistent with other research that has found that implant artefacts can influence CT attenuation maps. In a study investigating the impact of implant artefacts due to pacemakers and implantable cardioverter-defibrillator (ICD) leads on myocardial SPECT/CT imaging and CT attenuation maps, Etemadi et al. (2018) reported that pacemaker and ICD leads overestimate CT numbers within CTAC images. Furthermore, the study found that the overestimation in the corrected images due to the pacemaker was less than the ICD due to the lower atomic number (Etemadi et al., 2018). However, both Etamadi et al.'s (2018) and the current study have found that any material implants can impact the CT attenuation map, but the intensity of the impact is based on the atomic number of the implant materials. When materials with high atomic numbers are used, for example, ICD leads made of titanium with atomic number 22, the CT number overestimation will increase due to implant artefacts. However, breast implants are commonly made of silicone with atomic number 14, and the impact of these implants is less than that of a pacemaker or ICD lead due to their atomic number. Therefore, the influence on CT number changes was not significant when CTAC was applied. Finally, beam hardening caused by changes in the energy spectrum of the X-ray beam can shift the CT number in an image; the CT number can also be shifted because of photon starvation from highly attenuating materials, such as bone or metal.

Overall, it was found that there was no large variation of differences in subtracted CT number values of the cardiac region between the various breast implant sizes. The changes in average CT numbers between the different breast implant sizes compared to the reference were not significant. The differences within the average CT numbers values were less than ± 5 HU compared to the reference for all tested breast implants.

The subtracted CT number in this experiment shows that the range of the CT number is a small variation compared to the range of CT HUs in the diagnostic CT scanner, and therefore, the magnitude is different because the CT number is used to create the attenuation map and its

scaling is less than the CT HU scaling of the diagnostic CT scanner. The range of the subtracted CT number findings illustrate that large breast implants had bigger differences than small and medium breast implants. Table 16 demonstrates the range of the subtracted CT numbers among three different breast implants when the three different tube currents were used. The difference in the range of the CT number when the large breast implants were attached was 6.33, 5.33 and 4.78 HU, respectively, and 3.60, 3.00, and 2.89 HU, respectively, when the small breast implants were attached were, respectively, for the three tube currents (10, 20 and 30 mA). The range of the subtracted CT number almost doubled when the large breast implants were attached for all tube currents.

However, one of the aims of this study was to assess the impact of an increase in the tube current on the accuracy of the CT number for the CT attenuation map produced by the CT component of the SPECT/CT scanner. The data in Figure 19 show the impact of the increased tube current on differences in the CT numbers of the cardiac region between the three different breast implant sizes and the reference. Statistically, there was no significant difference in the average differences in CT numbers of cardiac tissue between the three different tube currents when small, medium and large breast implants were attached ($P = 0.75$, 0.90 and 0.78, respectively). The largest difference in CT numbers of the cardiac region reference images was 0.46 HU when the large breast implants were attached, with the 10 mA tube current, while the least difference was 0.27 HU for large breast implants, with the largest tube current (30 mA). There were decreases in differences in the CT numbers when the tube current was increased.

This finding is consistent with that of Thompson et al. (2013), who revealed no statistically significant variations in CT numbers changes among four different tube currents. The study confirms that differences in tube current have no effect on tissue attenuation and CT numbers. Thus, the attenuation map is independent of tube current (mA). This finding also shows that CT numbers accuracy was not affected by increasing mA in the SPECT/CT scanner. Consequently, the linear attenuation coefficients that generate the attenuation map should also be unaffected (Thompson et al., 2013). These results reflect those of Preuss et al. (2008), who also found that the maximum differences in attenuation coefficients of the heart were within a range of 5%, with no significant differences found when reviewing a range of the tube currents ($p > 0.05$). The author evaluated both phantom and patient images using two different tube current acquisitions (2.5 and 1 mA). Three materials were studied in the phantom, and the study found that the differences between the mean values were statistically insignificant. For example, the linear attenuation coefficient μ of water was 0.152909 ± 0.000250 and

0.152889 ± 0.000419 for 2.5 and 1 mA tube currents, respectively (P > 0.05). Also, the data of the patient (ROIs in the heart) illustrated that the maximum differences in attenuation coefficients of the heart were within a range of 5%, with no significant differences for both tube currents (p > 0.05). The linear attenuation coefficients µ of the heart within the ROIs were 0.1581 ± 0.0018 and 0.1582 ± 0.0012 for 2.5 and 1 mA tube currents, respectively. Reduction of the tube current appeared to decrease radiation exposure, while still providing equal attenuation maps for SPECT (Preuss et al., 2008).

These results also reflect those of Lawson et al. (2016), who also found no noticeable variation between the reconstructed image the CT attenuation map when the tube currents were increased from 8 to 80 mA. This study used five CT acquisitions (8, 12, 15, 40 and 80 mA) to create AC maps after a single SPECT acquisition and confirmed that variations in tube current did not affect tissue attenuation and the HU values. A very low-dose CT was found to be adequate for generating AC in quantitative SPECT. Thus, the attenuation map is independent of tube current (mA; (Lawson, Avram, Dewaraja, & Ackermann, 2016b). The findings of this thesis show that the accuracy of the AC map was not affected by increasing mA in the SPECT/CT scanner. Although the decreased tube current led to an increase in noise, noise is not a main factor that impacts AC.

Using a high tube current led to improved CT image quality, but the radiation dose to the patient would be increased due to the increased photon flux. Consequently, more tube current reduction could be possible without deteriorating the attenuation map. However, high-quality anatomic details are not required in myocardial perfusion SPECT imaging with a matrix of 64 × 64; this is not essential to increasing the tube current for this purpose.

4.7 Conclusion

The experiment was conducted using a clinical SPECT/CT scanner, and the findings showed the differences in cardiac CT numbers within ROIs when the different breast implant sizes were attached. When the size of the breast implants were increased, the differences in the cardiac CT number (HUs) within the ROIs also increased. The range values show that the large breast implants can impact CT number accuracy, with a range value of more than ± 6 HU. The findings also illustrate that large breast implants impact the accuracy of the CT number more than small and medium breast implants, respectively, resulting in lower CT numbers and underestimated µ-values. The findings show that increasing the tube current improves the CT numbers accuracy; however, increasing the tube current above 20 mA does not impact the

accuracy. Thus, a tube current above 20 mA will increase the patient dose without improving CT numbers accuracy.

However, the breast implants can cause errors within the CT attenuation maps on attenuation-corrected images on SPECT/CT data within the cardiac region of the phantom. When the attenuation map is inaccurate, false-positive findings might occur within the MPI scan, which can degrade the image quality and the quality of reconstructed CT images.

Chapter 5: Third Experiment: Assessment of the Impact of Breast Implants on the Accuracy of Total Counts of the Cardiac Region on SPECT/CT Data: A Phantom Study

The CT scanner's performance and components significantly impact image quality and patient exposure. Routine QC tests are intended to detect defects before impacting clinical patient studies. A CT number accuracy test checks that the CT scanner is operating appropriately in accordance with its specifications. Any errors in CT numbers will be propagated as errors in the radiotracer's estimated attenuation coefficients, which will impact the attenuation-corrected SPECT data and, hence, the reconstructed SPECT/CT images (Rep et al., 2017).

The findings of the previous experiment showed that large breast implants resulted in a greater difference in CT numbers within the cardiac region. However, the differences in CT numbers were within tolerance (i.e. less than 5 HU). The findings also illustrated that large breast implants impacted the accuracy of cardiac CT numbers within ROIs more than small and medium breast implants, resulting in lower CT numbers and underestimated μ-values. The results showed that breast implants impact the attenuation map. The third experiment aimed to evaluate the impact of the error in the attenuation map on corrected counts (SPECT/CT data).

5.1 Aim

This experiment aimed to assess the impact of breast implants on corrected counts in attenuation-corrected images of the cardiac region on SPECT/CT data.

5.2 Objective

The study used local clinical protocols to assess the impact of errors within CT attenuation maps from breast implants on attenuation-corrected images on SPECT/CT data within the cardiac region of the phantom.

5.3 Methods and Materials

The third experiment was based on local clinical protocols used at Saint Mary's Hospital in Manchester. This experiment was conducted using one tube current value (30 mA) from the local clinical protocol. The literature demonstrates that clinical protocols vary, but low tube currents are recommended to reduce the patient's dose. Particularly, high-quality anatomical details in MPI are not required. This study used three different tools to acquire the data: a clinical SPECT/CT scanner, LUNGMAN phantom and three different sizes of silicone breast implants.

5.3.1 SPECT/CT

This study was performed using a SPECT/CT dual-head system (Discovery NM/CT 640, GE Healthcare, Milwaukee, Wisconsin, USA; see Appendix II) to acquire and reconstruct all phantom images.

5.3.2 LUNGMAN phantom

For further information on the LUNGMAN phantom and the breast implants used, see Sections 3.3.2 and 3.3.3. The cardiac insert of the LUNGMAN (Figure 22) has been utilised in many previous studies (Abdullah, McEntee, Reed, & Kench, 2018). However, the phantom's internal structures, such as the cardiac region and lungs, are removable and can be replaced by other phantom inserts. Thus, modifications to the cardiac insert design for cardiac studies, such as nuclear cardiology tests, are achievable. The cardiac insert used in this experiment allows it to be filled with a radioactive tracer to produce the source required to acquire SPECT images and analyse SPECT data. The insert has a cavity on the left side to mimic the LV, and the radioactive tracer can be injected into the LV structure.
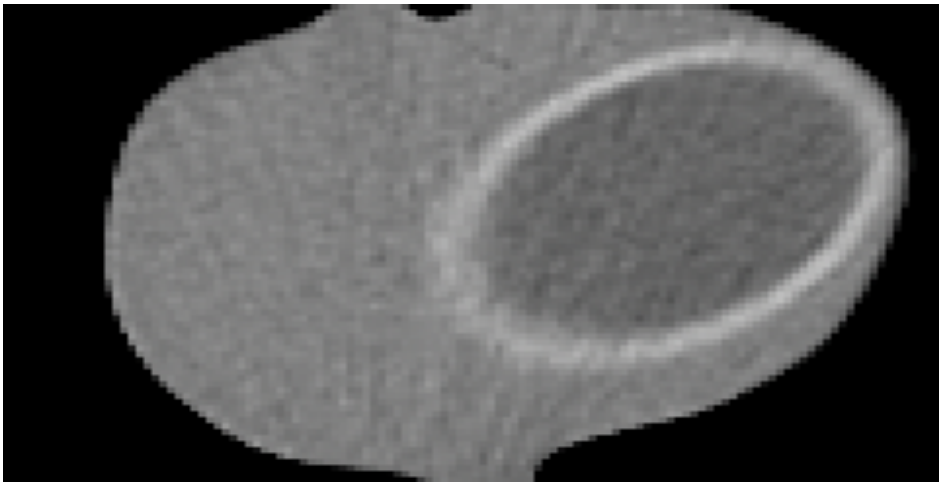
Figure 22: Phantom's cardiac insert with its cavity.

5.3.3 Radiotracer

A radiotracer can be defined as a small amount of radioactive isotope substance that is linked with a specific molecule and allows detection and measurement of the distribution of radioactive tracer molecules that can provide information about a specific biological process (Vallabhajosula, 2009). Because the experiment was based on a phantom study, technetium (^{99m}TC) was used as the radiotracer. It has good physical properties for imaging purposes. Its

half-life is 6 hours, which allows time to prepare and distribute a radiotracer, and its energy is 140 keV gamma photon, which is ideal for imaging by a gamma camera because it only emits gamma rays and its energy is easily detected by a gamma camera. In addition, it is produced relatively inexpensively.

The experiment was planned to minimise external exposure when the radiotracer was withdrawn by shielding and increasing the distance from the radiation source. Personal protective equipment, including disposable gloves, lab coats and safety glasses, was used when handling radioactive material. The [99m]TC was stored behind a thick lead shielding. Tools were used to indirectly handle unshielded sources to avoid direct contact. Sealed containers were used to carry radioactive material.

5.4 Experimental Set-Up

A SPECT/CT scanner was used. According to the Imaging Guidelines for Nuclear Cardiology Procedures (ASNC), the LEHR collimator and the L-mode, which are two heads at 90° to one another, were used. A 180° autocontouring orbit was carried out, beginning at the right anterior oblique and moving through the anterior to the left posterior in 3° steps (Dorbala et al., 2018b). The FOV of the camera was 40.9 x 40.9 cm. The low-dose CT images were performed immediately after the emission data on the same system. The main protocol used in this study was the local clinical CTAC protocol, and this protocol was used for each condition (i.e. no breast implant and small, medium and large breast implants). For AC images, a low-dose CT was used. The CT data were acquired using the following controlled parameters (Table 17). However, the SPECT data were reconstructed with the following controlled parameters to mimic local clinical protocol (Table 18).

Table 17: Scan parameters used during CTAC protocols

Protocol	CT Parameters
Phantom	LUNGMAN
kVp	120
Tube Current (mA)	30
Rotation Time(s)	1.00
Pitch	0.75
Image thickness(mm)	5
Reconstructed slice thickness (mm)	5
Matrix size	64×64
Field of view (FOV)	4.9 cm

The SPECT data were reconstructed with the controlled parameters, as listed in Table 18.

Table 18: Scan parameters used to reconstruct SPECT/CT

Protocol	Reconstruction parameters
Number of slices	64
Reconstructed slice thickness (mm)	5
Pixels size (mm)	6.8
Reconstruction algorithms	Iterative reconstruction (IR)
Iterations	16
Subset	6
FWHM	12 mm Gaussian Filter

According to the guidelines of the UK Administration of Radioactive Substances Advisory Committee, the recommended amount for the administered dose for an average weight (70 kg) adult patient for a one-day protocol is 800 MBq (Arumugam et al., 2013), with approximately 1.2% of the injected dose being taken up by the myocardium (Verberne et al., 2018). In accordance with the literature review, the activity distribution and activity quantities were selected to be comparable to the patient imaging conditions. Elkamhawy and Chandna (2001) used an 11 MBq injected dose that was approximately 1% of the patient dose within a cardiac phantom to define the minimum thickness of a defect inserted into the myocardial wall. Moreover, Purser et al. (2008) used a phantom to investigate the cause of an apparent apical defect of the cardiac region, and the researcher used 10 MBq as the injected dose(Purser,

Armstrong, Williams, Tonge, & Lawson, 2008). The cardiac region of the LUNGMAN phantom, with a cavity to simulate the LV, was therefore inserted and filled with 10 MBq ^{99m}TC, which was uniformly distributed throughout the 80 ml myocardial volume using a large syringe. To avoid any air bubbles left in the myocardium, the cardiac insert was carefully filled. When the cardiac insert was filled with 10 MBq ^{99m}TC, it was attached to the LUNGMAN phantom. The LUNGMAN phantom was then placed in the supine position in the centre of the gantry in the x and y planes, according to typical protocols for MPI. The breast implant was placed on the anterior thoracic wall of the phantom, corresponding to the space between the second rib and above the sixth rib. Three different sizes of breast implants (small 240 g, medium 490 g and large 685 g) were used with the LUNGMAN phantom.

The LUNGMAN phantom was scanned under four conditions. In all cases, the tube current was 30 mA. The four conditions were as follows:

- without a breast implant as a reference;

- with left and right small breast implants attached;

- with left and right medium breast implants attached; and

- with left and right large breast implants.

5.5 Image Analysis

The subtraction method was applied to assess the corrected count accuracy that may arise due to the introduction of breast implants within corrected SPECT/CT images of the cardiac region of the phantom. The experiment used one reference image, which was the image of a phantom without breast implants using the 30 mA tube current. Then, the images of small, medium and large breast implants were compared to the reference image using the 30 mA tube current.

The FWHM values were obtained using ImageJ software to plot a horizontal line profile across the centre of the cardiac region of the non-subtracted images. The plot profiles measured all the corrected count values along the plotted line. The FWHM method defined the ROI edges. The ROIs used throughout the experiment was defined on the reference image of the phantom without breast implants attached.

The following equation was then used to calculate the FWHM values for each individual slice that included the cardiac region in each set of images:

$$FWHM = \frac{Max - Min}{2}, \tag{4}$$

where:

FWHM = full-width half maximum to define the edge of the cardiac region within the phantom

Max = the maximum corrected counts value measured from the line profile

Min = the minimum corrected counts value measured from the line profile

The FWHM value was used as a threshold value to define the ROI. Any corrected counts less than the FWHM values were not included within the ROI; therefore, the edges were defined. The ROI was defined on the reference images of the phantom to ensure that any influence caused by breast implants was removed. ROIs were drawn once for each slice within the cardiac region of the phantom on each of the reference image sets. Then, the ROIs were applied across all subtracted image sets for consistency, and the ROI manager function in the ImageJ software was used to save and apply the ROIs to improve the reliability of the results. The corrected counts, noise and range values were measured from the resultant subtracted image to assess the impact of breast implant size on the accuracy of the corrected counts within the cardiac region of the phantom.
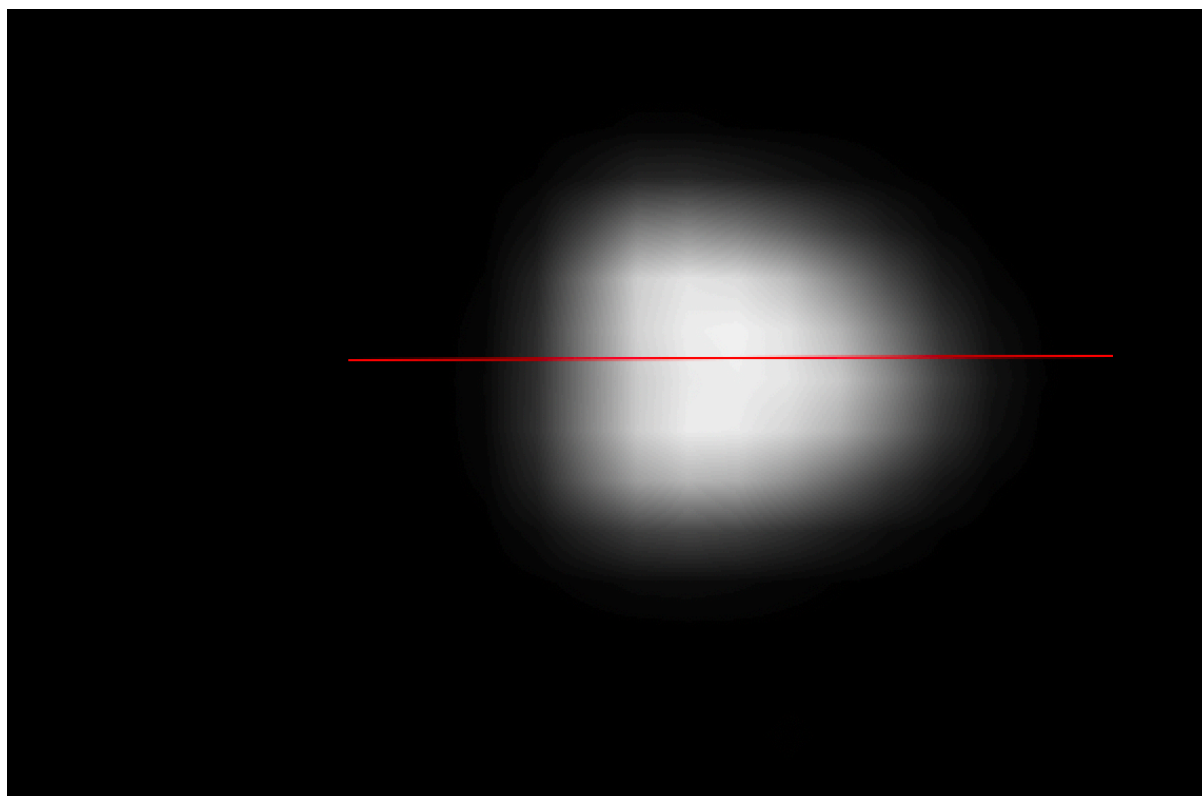
Figure 23: Line profile drawing for corrected SPECT image for the entire cardiac region/

The small, medium and large breast implant images were subtracted from the reference images. For each subtracted slice, the corrected counts, noise and range values of the corrected counts within the ROIs were measured per slice between the reference image and the images containing breast implants using ImageJ software. The data were then averaged across all slices within the cardiac region for each subtracted image set.

5.6 Decay Correction

Decay correction can be defined as a technique for calculating the amount of radioactive decay acquired at two different time points in a single data set (Mettler Jr & Guiberteau, 2012).

Because ^{99m}Tc was used as a radiopharmaceutical, the activity when the reference time was acquired differed from activity when the small, medium and large breast implants were attached due to radioactive decay. In addition, because ^{99m}TC was used as the radiotracer, a decay correction was applied to measure the radioactivity of the small, medium and large breast implants over the scans' durations. Equations 5 and 6 illustrate the radioactivity decay and decay correction, respectively:

$$\text{Radioactivity Decay} = A_t = A_0\ e^{-\lambda t}\ , \qquad\qquad (5)$$

where:

A_t = Activity at a specified time t ,

A_0 = Original Activity, activity at t = 0 time,

e = Euler's number constant, the base of natural logarithms,

λ = decay constant,

t = Elapsed time,

T = half-life,

$$\text{Decay Correction} = e^{\frac{(-0.693\ \times\ t)}{T1/_2}} \qquad (6)$$

5.7 Results

Excel 2013 was used to present the data. The graphs were also created in Excel to illustrate and describe the collected results. Mean differences in subtracted corrected counts, differences in subtracted noise and differences in range of the subtracted corrected counts were measured for the cardiac region of the phantom under three conditions. As the subtraction method was used, the data had already been compared to the baseline. Therefore, inferential statistics were not

possible. Although comparisons could be made between small, medium or large implants, this was not deemed appropriate, as clinically, individual patients would not have different implant sizes.

Table 19 shows the mean differences in subtracted corrected counts, differences in subtracted noise and differences in the range of subtracted corrected counts values in the cardiac ROI when images of the small, medium and large breast implants were subtracted from reference images for the cardiac region of the phantom using the 30mA tube current.

Table 20 : The measured average differences in the corrected counts, noise, and range when images of all three breast implant sizes were subtracted from reference images using 30 mA tube current.

Tube current (mA)	Subtraction (Breast implant size subtract reference)	Measurements				
		Differences subtracted in corrected counts within ROIs	Differences subtracted in noise	Min	Max	Differences subtracted in range (counts)
30	Small subtract reference	271.44	240.60	-553	289	892
30	Medium subtract reference	723.85	302.04	-842	104	1014
30	Large subtract reference	859.58	338.91	-1070	84	1056

The results obtained from the preliminary analysis of the average differences in decay and the attenuation-corrected count values of the cardiac region between the reference and the three different breast implant sizes are displayed in Figure 24. The scatter graph in Figure 24 shows a consistent trend in which the differences in subtracted corrected counts increase when breast implant sizes increase. As seen in Table 19, the highest difference in subtracted cardiac corrected counts within ROIs from the reference image among all breast implant sizes was 859.58 counts for large breast implants, and the least was 271.44 counts for the small breast implants. This value for the medium breast implants was 723.85 counts.

Figure 24: The differences in subtracted corrected counts in cardiac ROIs in scans where images of small, medium and large breast implants are subtracted from references images when using the 30 mA tube current

Figure 25 depicts the data showing the average differences in noise in the cardiac region by subtracting the images of all three breast implant sizes from the reference images when 30 mA tube currents were used. The scatter graph in Figure 25 shows the expected trend that, when noise increases, breast implant size increases. The difference in subtracted noise value within ROIs when small breast implant sizes were attached was 240.60, and increasing the breast implant size led to an increase in the differences in subtracted noise within ROIs to 302.04 and 338.91, respectively, when medium and large breast implant sizes were attached.

The difference in subtracted noise within ROIs when the small breast implants were attached showed the least difference (240.60) from the reference image, compared to medium and large breast implant images, whereas the large breast implants showed the highest noise difference (338.91) compared to other breast implant sizes. The findings show that there is a bigger difference in subtracted noise with the large breast implants, while the least difference in subtracted noise was found with small breast implants (Table 19).
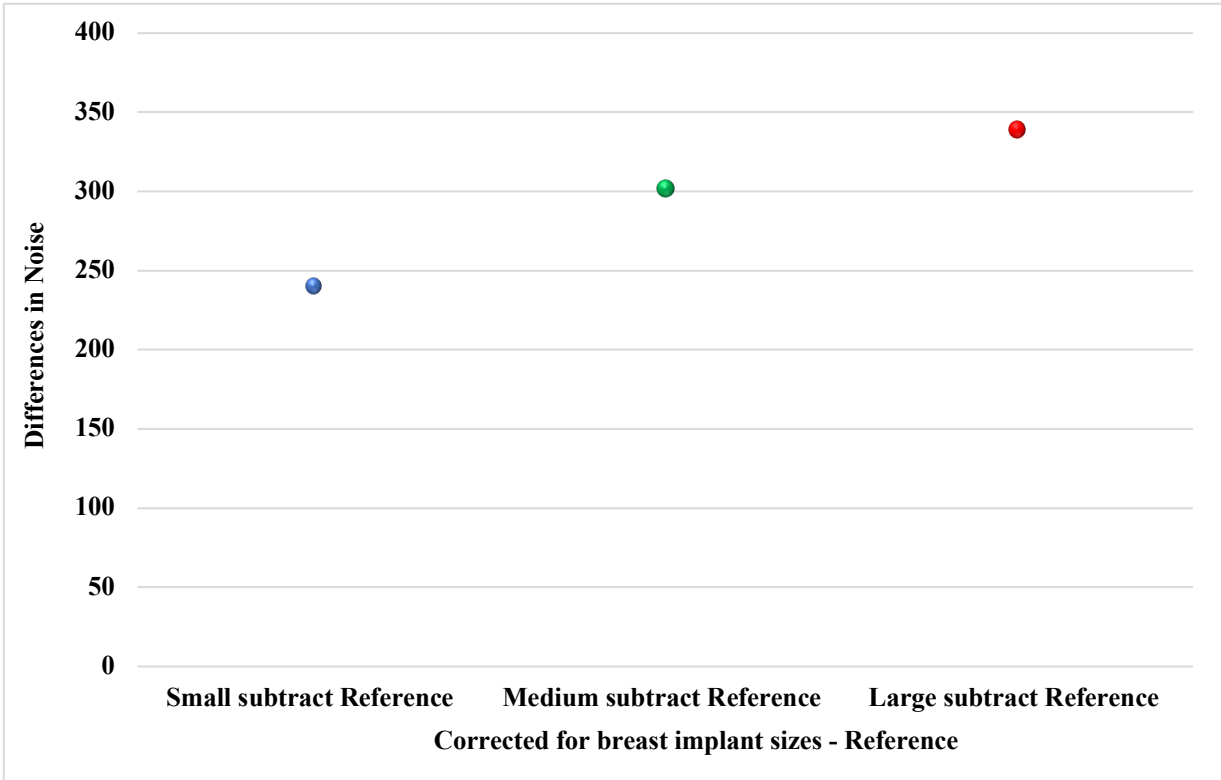
Figure 25: The differences in subtracted noise values in cardiac ROIs in scans where images of small, medium and large breast implants are subtracted from references images when using the 30 mA tube current

Figure 26 illustrates the difference in the range of subtracted corrected counts in cardiac ROIs among all three breast implant images subtracted from the reference image. There was an increased difference in range of subtracted corrected counts in the cardiac region for all breast implant sizes. The scatter graph in Figure 26 illustrates that increases in differences in the range of subtracted corrected counts values occurred along with increased breast implant size. As seen in Table 19, the small breast implants resulted in the least value difference (892) from the reference image in terms of the range of subtracted corrected counts, compared to the medium and large breast implants (1014 and 1056 counts, respectively).
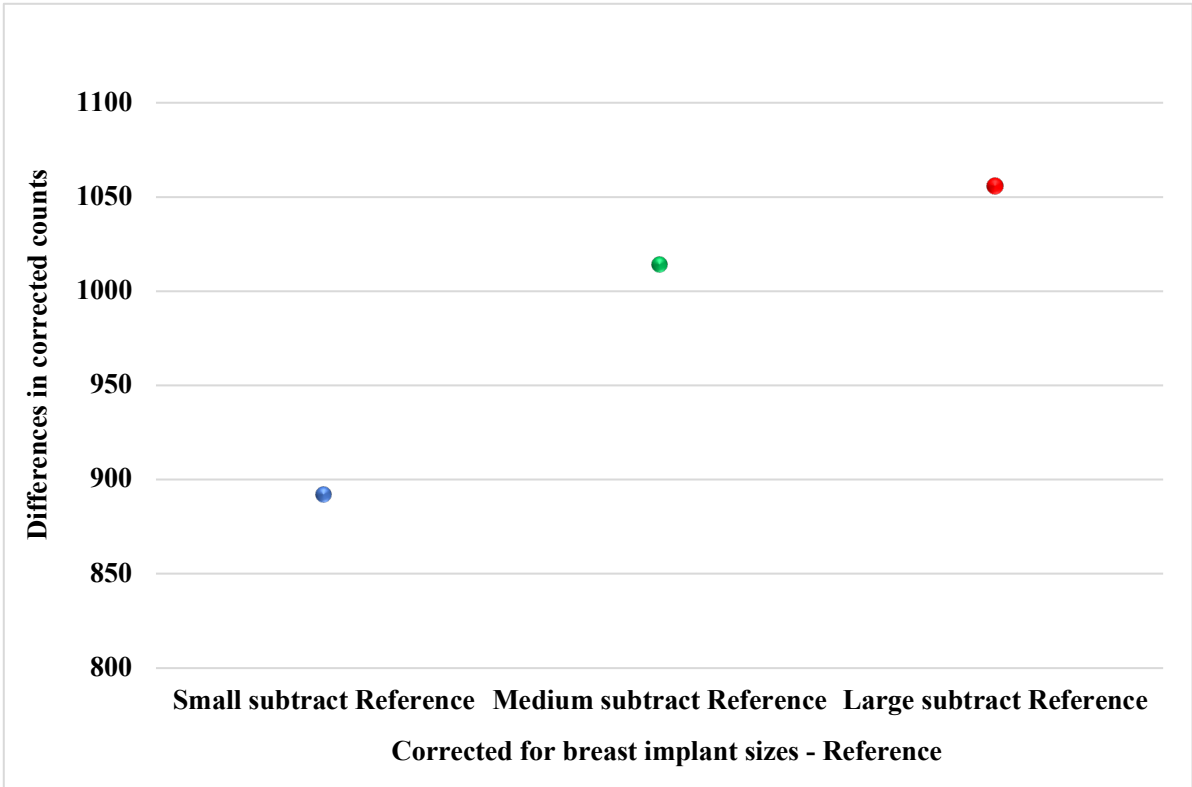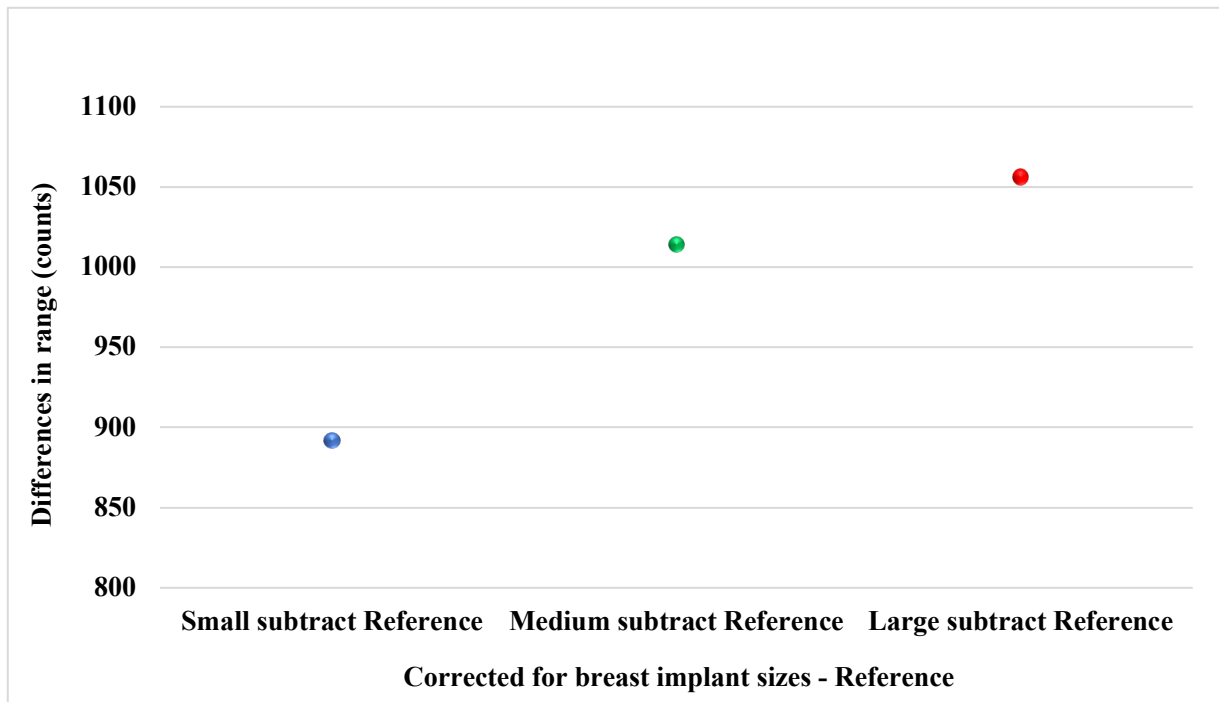
Figure 26: The differences in range of subtracted corrected counts in cardiac ROIs in scans where images of small, medium and large breast implants are subtracted from references images when using the 30 mA tube current

5.8 Discussion

The accuracy in the diagnosis of perfusion defects and, hence, vessel obstructions is affected by some factors that can degrade MPI SPECT images. One of these factors is soft-tissue attenuation artefacts. Natural breasts may produce artefacts, and the accuracy of CAD diagnosis can also be decreased as a result. These artefacts are mainly based on the size of the breast and the breast location, and they can be difficult to distinguish from true perfusion defects. This is especially true for lesions within the anterior wall of the heart, and errors are more obvious in females with large breasts. Furthermore, because breast implants have a higher density than normal breast tissue, they are predicted to produce more marked attenuation than normal breast tissue during MPI. Breast implants might cause a reduction in myocardial SPECT counts at the anteroseptal wall in female patients; thus, the probability of a false-positive defect increases. Breast attenuation artefacts are common artefacts that decrease photon counts in the anterior myocardial wall. However, large breasts lead to decreased counts, thus creating noise and, therefore, might impact the diagnostic image (Dvorak, Brown, & Corbett, 2011).

In this part of the study, the local clinical protocol was used for LUNGMAN phantoms to mimic the real acquisition of patients with CAD or suspected CAD. This work was performed on a clinical SPECT-CT scanner. This element of the project was conducted to establish whether

small changes highlighted by the subtraction method in the count values would impact the corrected SPECT data.

The corrected counts of cardiac tissue within the ROIs were subtracted to evaluate any changes or differences between the reference (control), and breast implants of different sizes were added. The results obtained from the preliminary analysis of the average corrected counts of cardiac tissue among the three different breast implant sizes are displayed in Figure 24.

The maximum difference from the reference image between all sizes was 859.58 counts for large breast implants, and the minimum was 271.44 counts for small breast implants. This finding appears to be consistent with other research that found that counts of the myocardial wall in women with implants were reduced compared with the count of the myocardial wall in the control group; this was due to the impact of the breast implants, namely in the anterior wall (Caner et al., 1999). Moreover, these results seem to be consistent with other research that found that silicone breast implants presented a large fixed anterior wall perfusion defect with normal anterior wall motion marked on the SPECT study (Meine et al., 2005).

The findings of the current study found that the larger the breast implant, the greater the overcorrection. There is a larger difference in counts with the larger breast implant within the cardiac region. The results show that increased breast implant size can impact the accuracy of the corrected SPECT data. The larger the breast implant, the greater the impact on the overcorrection and, therefore, the accuracy of the corrected SPECT images. However, any small changes or impacts on CTAC accuracy may affect the image interpretation of the MPI. These results suggest that breast implant size has an effect on corrected counts when compared to the reference image. Furthermore, the results of this study showed there was a greater effect of breast implant size on corrected SPECT data. This finding suggests that the accuracy of the corrected SPECT images is impacted when breast size is increased. This can be explained by the fact that larger implants can cover more area of a patient's chest, and gamma photons will be attenuated more before reaching the gamma detectors. In contrast, counts of small breast implants almost do not have a greater count difference compared to the reference, as the comparison between images found a roughly 271.44 count reduction. The gamma photons travel through the chest structures and penetrate organs and tissues before reaching the gamma detectors. The images are degraded less because photon attenuation is decreased. Large breast implants attenuate more photons, with around an 859.58 count reduction compared to the reference, and AC accuracy is affected because of the need to compensate for this. Comparing attenuation counts between the reference (no breast implants) and large breast implants was

performed by analysing SPECT/CT images of the cardiac region of the phantom with AC. This is done because the reference does not have any soft tissue or high-density tissue that can attenuate photons, whereas large breast implants attenuate photons, and AC compensates for these photons. The current study found that AC accuracy can be affected when large or medium breast implants are imaged; thus, diagnostic accuracy might be decreased.

These results are in line with those of previous studies that compared the impact of breast implant attenuation with different breast implant sizes between two different positions. Ramos et al. (2020) studied breast implant attenuation artefact behaviour in the supine and prone positions. The results compared breast implant attenuation improvement between the two positions of the left ventricular segments when different breast implants were attached to the phantom. The authors reported that photon counts increased with prone positions for all breast implant sizes, mostly in the anterior and inferior LV segments in the short axis. This may be due to the flattening of the tissue of the breast implants when the phantom was set in this position, which decreases the thickness of the tissue that the radiation needs to pass through. The study showed that large breasts behave differently than all other breast implant sizes. The photon counts decreased more in the apex region for the large breast implants compared to the different breast implant sizes, and there is an added risk of artefacts from breast implant attenuation, which could compromise the MPI results (Ramos, Glavam, de Brito, Kubo, Tukamoto, Sampaio, & de Sa, 2020)

The current study shows that small breast implants had the least difference in range of subtracted corrected counts (892 counts), whereas the large breast implants had the greatest (1056 counts). In addition, the large breast implants overcorrect the counts.

Patients with large breast implants can see more AC impact than those with small and medium breast implants. Small breast implants produced a moderate effect on the AC, but this was not a large impact. The impact of the large breast implants can be explained by the cardiac location and breast distribution over the patient's chest. The covering of the cardiac tissue by large breast tissue causes more attenuation of photons, and these photons should be corrected.

5.9 Conclusion

Since there have been notable increases in recent cosmetic surgery rates, the number of women with breast implants who undergo SPECT MPI will increase (Stinis et al., 2006). The current study found that large breast implants had a greater difference in corrected counts of the cardiac region. The study also showed that small or medium breast implants had the least difference in

corrected counts within the cardiac region compared to large breast implants. The existence of high object densities that can overlay the anterior wall of the cardiac region might markedly increase attenuation artefacts. Depending on the partial or complete coverage of cardiac structures by breast implants during MPI imaging, partial or completely reversible defects can be seen.

5.10 Potential Changes to Clinical Practice:

It is crucial to remember that the prevalence of coronary artery disease (CAD) beyond the seventh decade of life is comparable in men and women, but the prognosis is worse for women once CAD is diagnosed. Myocardial perfusion scintigraphy (MPS) is a non-invasive imaging technique that is crucial in diagnosing and managing coronary artery disease (CAD), and it has been thoroughly validated in clinical practice for both men and women (Ramos, Glavam, Kubo, & Sá, 2014). A gamma camera and a radiopharmaceutical are used in this nuclear medicine imaging approach. Although it has been a routine procedure for more than two decades, there is still debate about the most suitable acquisition and reconstruction parameters to reduce the effects of attenuation artefacts (Farrell et al., 2021).

Single-photon emission computed tomography-computed tomography (SPECT-CT) systems combine a SPECT gamma camera and a CT system. Both emission and transmission data sets are used in hybrid imaging to improve diagnostic performance, decrease the number of equivocal findings, and contribute to the image information. Using such an integrated system has certain advantages; the transmission images can be used for transmission correction and anatomic co-registration when the anatomic localisation of a lesion is challenging(Farrell et al., 2021).

As we know, in SPECT imaging, photons are emitted out of the patient and detected by gamma cameras. As photons traverse through the body, they undergo attenuation. If the source was perfectly at the centre of a homogenous body, and they all underwent equal attenuation there would be no need for attenuation correction. However, the human body is not homogenous in tissue densities and emissions do not originate from a single source. So, for correction of the attenuation of the photons, CT is used. CT data is a representation of the attenuation of the photons as they go through tissue; it is an attenuation map. By combining accurate information from the emission and transmission approaches, we can get attenuation corrected images. Clearly, accurate CT attenuation mapping is essential.

Due to the CT component being added to nuclear medicine, hybrid imaging has increased radiation exposure; therefore, it has become essential to assess the clinical purpose of the CT

scan. The wide range of radiation exposure associated with various acquisition protocols and clinical purposes has underlined the necessity for hybrid imaging optimisation (Camoni, Santos, Attard, Mada, Pietrzak, Rac, Rep, Terwinghe, & Fragoso Costa, 2020).

Reduced radiation exposure in CT reduces detectable photons and, as a result, increases image noise, potentially resulting in diminished diagnostic performance. Imaging conditions should be optimised by balancing potential risks associated with radiation exposure and clinical advantages (Inoue et al., 2018).

CT-based attenuation correction is one of the most widely utilised approaches for managing SPECT photon attenuation in the body. Photon attenuation in the body degrades image contrast affecting quantification of activity and relative perfusion distribution, leading to a reduction in image quality. Because of the significant photon attenuation, CT-based attenuation correction is required in cardiac PET, although it is recommended in SPECT, according to European Association of Nuclear Medicine (EANM) guidelines (Verberne et al., 2015).

Each manufacturer has developed an AC protocol, and the company's handbook should be the first reference for anyone new to the technology. CT scans performed just for attenuation correction should be performed at the lowest possible settings. Depending on the manufacturer, the tube voltage will typically range between 70 and 140 kVp and must be adjusted according to the patient's size. Because it is common practice to smooth CT data before using it for attenuation correction, noise has a minimal impact; hence image quality can be optimised to reduce the patient's effective dose. Therefore, the manufacturer recommends a low tube current (10-20 mA) combined with a relatively high pitch to reduce radiation exposure (Camoni, Santos, Attard, Mada, Pietrzak, Rac, Rep, Terwinghe, & Fragoso Costa, 2020).

Because CT is utilised for correction rather than diagnosis, low tube currents are typically used for attenuation correction. Therefore, breast implants with a higher density than normal breasts might attenuate the photons more, and we need to compensate for this attenuation. However, increasing the tube current used for CT attenuation correction to a value greater than 30 mA to compensate for the impact of breast implants will not improve CT attenuation map accuracy, and hence is unnecessary. Therefore, when designing the CT attenuation correction protocol for a patient with silicone breast implants, the tube current should not exceed 30 mA.

Nuclear cardiology is still developing within nuclear medicine applications. Furthermore, understanding each patient's features and conditions enables the nuclear medicine team to modify the protocol, bringing significant benefits to each patient. In addition, a careful and knowledge-based choice of CT parameters minimises the effective dose for the patient while keeping acceptable image quality.

Therefore, the nuclear medicine team must have comprehensive knowledge of the CT acquisition settings and protocols and an understanding of the differences across CT scanners to ensure that the patient receives the optimal examination in terms of diagnostic quality and effective dose.

Chapter 6: Conclusion

6.1 Conclusion

This experimental work was designed to determine the effect of breast implants on CT AC by testing the effect of three different breast implant sizes on MPI SPECT/CT scanning. In this thesis, the main findings from the literature review regarding AC and diagnostic performance were that there is variability in MPI procedures among women. Also, within the literature, no explanations were given for the impact of breast implants of different sizes during the procedures, which may also affect AC accuracy. A review of the research indicated that AC is currently widely used for diagnostic purposes and that it could increase the accuracy of SPECT data. To assess the effects of breast implants on the accuracy of AC in MPI, a phantom with different breast implants was used. The phantom was scanned using a SPECT/CT gamma camera in clinical practice, and the findings support the notion that AC can be used to decrease soft-tissue artefacts, particularly for patients with large breast implants.

The findings of the first study clearly demonstrate that different silicone breast implant sizes can impact average HUs. The subtraction method showed that there was a difference in the cardiac CT HUs between the implants and the reference, which was attributed to the breast implants' impact on CT HU accuracy. The findings for the subtraction method reported that breast implants of any size could affect CT AC accuracy. However, the findings of the corrected SPECT data showed that small breast implants did not result in large reduction differences in corrected counts compared to the reference. By contrast, large breast implants resulted in a greater reduction in corrected counts compared to the reference. The subtraction method showed differences in the corrected counts of the cardiac region, which were attributable to the breast implants' impact on AC accuracy. Breast implant attenuation might create artefacts and lead to inaccuracies in reconstructed images, which can impact diagnostic performance.

The first experiment's data, which were collected using a diagnostic CT scanner, revealed no large variations between the CT HU values of the cardiac region with no breast implants and with different breast implant sizes (less than $\pm\ 5$ HU). However, this technique was not sensitive enough to detect any small CT HU changes. As a result, a further subtraction method was used to investigate any small CT HU inaccuracies. When the subtraction technique was used, the study showed that there was no large difference in the cardiac CT HUs between the reference and the different breast implant sizes among the various tube currents.

The findings of the second experiment also illustrate that large breast implants impact the accuracy of the CT number more than small and medium breast implants, respectively, resulting in lower CT numbers and underestimated μ-values.

The last experiment used a ^{99m}TC as a radioisotope with a LUNGMAN phantom. This experiment was an example of SPECT data when local clinical protocols were used. The findings of this experiment revealed that there was a large difference in the corrected count values of the cardiac tissue with large breast implants present when compared to small breast implants. Patients will benefit from improved AC accuracy, and this should reduce the further risk of undergoing an unnecessary invasive investigation.

6.2 Limitations

The experiments were carried out under ideal conditions and using phantoms. Within the experiment described in this study, several limitations have been identified. These have arisen as a result of access restrictions in the nuclear medicine departments of the hospitals and because this thesis investigated the variation in tube current acquisitions only for the local clinical protocols. However, due to time issues, the different tube currents were not studied. The impact on the attenuation map was greater within 10 or 20 mA with large breast implants, which might impact corrected counts (SPECT/CT data). Using different exposure factors might have determined whether there were any exposure factors that could impact the accuracy of AC. This would have provided a broader range of data that could have been used as estimations of the impact of breast implants on AC quality. Using the phantoms to acquire the images in this experiment raised some problems because they are limited by their lack of movement (e.g. no respiratory motion). This meant that some factors that usually impact the AC technique (e.g. patient respiratory movement) were not considered. This can be responsible for visible artefacts (image blurring) in MPI and interfere with the detectability of perfusion defects. This motion can impact CTAC because SPECT images are acquired over a longer period of time than CT images. Anatomical variation was not present and did not reflect the nature of the human body. Therefore, the simulated pathologies in the phantoms did not mimic clinical reality.

6.3 Recommendations for Future Work

This study has shown that the AC technique in SPECT/CT scanning can be used to assess the diagnostic accuracy of MPI. Further work could be carried out in this area. In this study, only one SPECT-CT system was used; therefore, for better external validity, the method would need to be repeated across different manufacturers.

This thesis showed the impact of breast implants with one density and one type of breast implant (silicone), but there are two main types of breast implants (silicone and saline) with different densities. Further studies are needed to evaluate the differences between two different types of breast implants with different breast implant densities and to investigate the effects of increasing breast density on AC. The use of one breast density and one type of breast implant in this study concluded that large breast implants can impact SPECT data when the entire cardiac region is used as the ROI. Using different densities for different sizes might reveal that small or medium breasts can also impact the SPECT data, and thus, the quality of AC might be affected and reduce the diagnostic accuracy.

Further study is needed to compare and find any differences between non-corrected images and corrected images for a female with breast implants, as this work used only corrected breast implants images instead of both corrected and non-corrected images. However, the corrected counts in this study were decreased by 6%, 16% and 19% for small, medium and large breast implants, respectively, compared to the reference-corrected counts with a LUNGMAN phantom. Further empirical studies could establish the degree to which the count decrease causes a clinically significant defect in the SPECT data. In CT data, any HU changes within $\pm$ 5 HU will not be clinically significant, whereas in SPECT, further work should be carried out to investigate this effect. This work only used clinical exposure factors due to restricted access to nuclear medicine departments. Considerably more work will need to be done using different exposure factors to determine if there are any various exposure factors that can impact the AC quality.

Finally, there was limited availability of nuclear medicine staff to withdraw radioisotopes to be injected into the phantom. This led to using ^{99m}TC as a radiotracer rather than a different radiotracer that is a non-technetium radiopharmaceutical, such as Thallium 201. Low-energy radioisotopes can create softer tissue artefacts compared to high-energy radioisotopes.

Appendices:
Appendix I: Method for CT Scanner Quality Control (QC)

Vendors for CT scanners usually release specifications on tolerance for CT numbers. For example, the tolerance of the CT number values in General Electric (GE) for water is within $\pm$ 3 HU of zero when a specific quality assurance protocol is used. Some regulatory agencies, such as Health Canada's Safety, release specific tolerances for CT numbers. It states that CT number values must be within $\pm$ 4 HU of zero and air values within $\pm$ 10 HU of -1000 (Cropp, Seslija, Tso, & Thakur, 2013)

The following method was used for QC. The adaptor from the body armrest was inserted into the table end; then, the phantom holder was slid into the adaptor. The TOS phantom was mounted on the tube side of the phantom holder, and the phantom was inserted in a central position within the gantry. Positioning lights were used to centre the QC insert of the phantom. A new patient was created on the workstation, and the appropriate protocol was selected. The ROI tool was used to obtain an ROI that would fit each insert. The mean HU was calculated for each material contained in the TOS phantom and for the centre of the phantom; the data were recorded on a spreadsheet. The phantom was positioned in the centre of the gantry, and the parameters shown in the table below were measured. The results recorded for all QC procedures were within acceptable levels, according to the recommendations of the radiation protection legislation by ICRP (2007) and Toshiba (2014; Baseline $\pm$ 5 HU (water) or $\pm$ 10 HU).

Appendix II: Full specifications of SPECT Optima NM/CT 640 (SPECT/CT) Scanner

SPECT	Specifications
Table weight	565 kg
Maximum patient load capacity	227 kg
Table width	61 cm
Table length	280 cm
Table hight range	Minimal 59 cm, Maximal 100 cm
Gantry	**Specifications**
Depth (length)	210 cm
Width	199 cm
Hight	211 cm
Gantry bore size (diameter)	70 cm
Weight	2970 kg
Gantry orientations	90° and 180° opposing
Detector	**Specifications**
Design	59 circular PMT's
Crystal thickness	9.5 mm
Energy range	40 – 620 keV
Field of view (FOV)	54 cm
Collimator (Low Energy High Resolution)	**Specifications**
FOV	50×40 cm
Type of hole	Hexagonal
Hole Diameter	1.5 mm
Septal thickness	0.2 mm
Hole length	35 mm

Appendix III: Full specifications of CT component in SPECT Optima NM/CT 640 (SPECT/CT) Scanner

Low-dose integrated CT system	Specifications
Gantry aperture	70 cm
Scan field of view	50 cm
Rotation time	1, 2 seconds
Tube current	10–30 mA
Tube voltage	120 or 140 kV
Pitch factor	0.75, 1.25 and 1.75
Reconstructed slice thickness	2.5 or 5 mm

References

Aaronson, P. I., Ward, J. P. T., & Connolly, M. J. (2013). *The cardiovascular system at a glance.(z-lib.org).pdf*.

Aaronson, P. I., Ward, J. P., & Connolly, M. J. (2020). *The cardiovascular system at a glance*: John Wiley & Sons.

Abdoli, M., Ay, M. R., Ahmadian, A., & Zaidi, H. (2010). A virtual sinogram method to reduce dental metallic implant artefacts in computed tomography-based attenuation correction for PET. *Nuclear medicine communications, 31*(1), 22-31.

Abdullah, K. A., McEntee, M. F., Reed, W., & Kench, P. L. (2018). Development of an organ-specific insert phantom generated using a 3D printer for investigations of cardiac computed tomography protocols. *Journal of medical radiation sciences, 65*(3), 175-183.

Ades, P. A., & Savage, P. D. (2017). Obesity in coronary heart disease: An unaddressed behavioral risk factor. *Prev Med, 104*, 117-119. doi:10.1016/j.ypmed.2017.04.013

Afifi, M. B., Abdelrazek, A., Deiab, N. A., Abd El-Hafez, A., & El-Farrash, A. (2020). The effects of CT x-ray tube voltage and current variations on the relative electron density (RED) and CT number conversion curves. *Journal of Radiation Research and Applied Sciences, 13*(1), 1-11.

Ahmed, S., Snelling, A., Bains, M., & Whitworth, I. (2005). Breast reconstruction. *bmj, 330*(7497), 943-948.

Al Badarin, F. J., & Malhotra, S. (2019). Diagnosis and prognosis of coronary artery disease with SPECT and PET. *Current cardiology reports, 21*(7), 1-11.

Anagnostopoulos, C., Harbinson, M., Kelion, A., Kundley, K., Loong, C., Notghi, A., . . . Underwood, S. (2004). Procedure guidelines for radionuclide myocardial perfusion imaging. *Heart, 90*(suppl 1), i1-i10.

Apostolopoulos, D. J., & Savvopoulos, C. (2016). What is the benefit of CT-based attenuation correction in myocardial perfusion SPET. *Hell J Nucl Med, 19*(2), 89-92.

Arcelus, J., Bouman, W. P., Van Den Noortgate, W., Claes, L., Witcomb, G., & Fernandez-Aranda, F. (2015). Systematic review and meta-analysis of prevalence studies in transsexualism. *European Psychiatry, 30*(6), 807-815.

Arumugam, P., Harbinson, M., Reyes, E., Sabharwal, N., Tonge, C., Underwood, R., & Kelion, A. (2013). Procedure guidelines for radionuclide myocardial perfusion imaging with single-photon emission computed tomography. *Nuclear medicine communications, 34*(8), 813-826.

Asscheman, H., Giltay, E. J., Megens, J. A., van Trotsenburg, M. A., & Gooren, L. J. (2011). A long-term follow-up study of mortality in transsexuals receiving treatment with cross-sex hormones. *European journal of endocrinology, 164*(4), 635-642.

Baert, A. L. (2006). *Diagnostic nuclear medicine*: Springer Science & Business Media.

Bai, C., Conwell, R., Kindem, J., Babla, H., Gurley, M., De Los Santos, R., . . . Maddahi, J. (2010). Phantom evaluation of a cardiac SPECT/VCT system that uses a common set of solid-state detectors for both emission and transmission scans. *Journal of Nuclear Cardiology, 17*(3), 459-469.

Bailey, D. L., & Humm, J. (2014). *Nuclear medicine physics: a handbook for teachers and students*: Iaea.

Barr, S., & Bayat, A. (2011). Breast implant surface development: perspectives on development and manufacture. *Aesthetic surgery journal, 31*(1), 56-67.

Barrett, J. F., & Keat, N. (2004). Artifacts in CT: recognition and avoidance. *Radiographics, 24*(6), 1679-1691.

Bartlett, J., & Frost, C. (2008). Reliability, repeatability and reproducibility: analysis of measurement errors in continuous variables. *Ultrasound in Obstetrics and Gynecology: The Official Journal of the International Society of Ultrasound in Obstetrics and Gynecology, 31*(4), 466-475.

Bateman, T. M. (2012). Advantages and disadvantages of PET and SPECT in a busy clinical practice. *Journal of Nuclear Cardiology, 19*(1), 3-11.

Bekeny, J. C., Zolper, E. G., Fan, K. L., & Del Corral, G. (2020). Breast augmentation for transfeminine patients: methods, complications, and outcomes. *Gland surgery, 9*(3), 788.

Bhatnagar, P., Wickramasinghe, K., Wilkins, E., & Townsend, N. (2016). Trends in the epidemiology of cardiovascular disease in the UK. *Heart, 102*(24), 1945-1952. doi:10.1136/heartjnl-2016-309573

BHF. (2018). coronary heart disease statistics. *British Heart Foundation*.

Blake, P., Johnson, B., & VanMeter, J. W. (2003). Positron emission tomography (PET) and single photon emission computed tomography (SPECT): clinical applications. *Journal of neuro-ophthalmology, 23*(1), 34-41.

Błaszczyk, M., Adamczewski, Z., & Płachcińska, A. (2021). Capabilities of Modern Semiconductor Gamma Cameras in Radionuclide Diagnosis of Coronary Artery Disease. *Diagnostics, 11*(11), 2130.

Boas, F. E., & Fleischmann, D. (2011). Evaluation of two iterative techniques for reducing metal artifacts in computed tomography. *Radiology, 259*(3), 894-902.

Boas, F. E., & Fleischmann, D. (2012). CT artifacts: causes and reduction techniques. *Imaging Med, 4*(2), 229-240.

Borges-Neto, S., Hanson, M., Ravizzini, G., Wong, T., Hagge, R., Shaw, L., & Coleman, R. (2000). *Efficiency comparison between Tc-99m tetrofosmin and Tc-99m sestamibi myocardial perfusion studies.* Paper presented at the Journal of Nuclear Medicine.

Boyette, L. C., & Manna, B. (2019). Physiology, myocardial oxygen demand. *StatPearls [Internet]*.

Breast and Cosmetic Implant Registry (BCIR). (2021,October 06). Breast and Cosmetic Implant Registry - January 2020 to December 2020, Management Information. Retrieved from https://digital.nhs.uk/data-and-information/publications/statistical/mi-breast-and-cosmetic-implant-registry/2021

Bushberg, J. T., & Boone, J. M. (2011). *The essential physics of medical imaging*: Lippincott Williams & Wilkins.

Bybel, B., Brunken, R. C., DiFilippo, F. P., Neumann, D. R., Wu, G., & Cerqueira, M. D. (2008). SPECT/CT imaging: clinical utility of an emerging technology. *Radiographics, 28*(4), 1097-1113.

Camoni, L., Santos, A., Attard, M., Mada, M. O., Pietrzak, A. K., Rac, S., . . . Costa, P. F. (2020). Best practice for the nuclear medicine technologist in CT-based attenuation correction and calcium score for nuclear cardiology. *European Journal of Hybrid Imaging, 4*(1), 1-20.

Camoni, L., Santos, A., Attard, M., Mada, M. O., Pietrzak, A. K., Rac, S., . . . Fragoso Costa, P. (2020). Best practice for the nuclear medicine technologist in CT-based attenuation correction and calcium score for nuclear cardiology. *European Journal of Hybrid Imaging, 4*(1), 1-20.

Caner, B., Ozgur, F., Bor, D., Ulutuncel, N., Aydin, M., & Sari, O. (1999). Effect of silicone breast implants on myocardial imaging. *Annals of plastic surgery, 43*(5), 471-475.

Cassar, A., Holmes Jr, D. R., Rihal, C. S., & Gersh, B. J. (2009). *Chronic coronary artery disease: diagnosis and management.* Paper presented at the Mayo Clinic Proceedings.

Champaneria, M. C., Wong, W. W., Hill, M. E., & Gupta, S. C. (2012). The evolution of breast reconstruction: a historical perspective. *World journal of surgery, 36*(4), 730-742.

Chaturvedi, A., Oppenheimer, D., Rajiah, P., Kaproth-Joslin, K. A., & Chaturvedi, A. (2017). Contrast opacification on thoracic CT angiography: challenges and solutions. *Insights into imaging, 8*(1), 127-140.

Chawla, D., Rahaby, M., Amin, A. P., Vashistha, R., Alyousef, T., Martinez, H. X., & Doukky, R. (2011). Soft tissue attenuation patterns in stress myocardial perfusion SPECT images: a comparison between supine and upright acquisition systems. *Journal of Nuclear Cardiology, 18*(2), 281-290.

Cherry, S. R., Sorenson, J., Phelps, M. E., & Methé, B. M. (2004). Physics in nuclear medicine. *Medical physics, 31*(8), 2370-2371.

Cherry, S. R., Sorenson, J. A., & Phelps, M. E. (2012). *Physics in nuclear medicine e-Book*: Elsevier Health Sciences.

Çimen, S., Gooya, A., Grass, M., & Frangi, A. F. (2016). Reconstruction of coronary arteries from X-ray angiography: A review. *Medical image analysis, 32*, 46-68.

COLEMAN, W. P. (2011). The Art of Aesthetic Surgery: Principles and Techniques, Edited by Foad Nahai. In: LWW.

Criado, D. A. B., Braojos, F. D. C., Torres, U. d. S., & Muniz, M. P. (2012). Aesthetic breast augmentation with hyaluronic acid: imaging findings and implications for radiological assessment. *Radiologia Brasileira, 45*, 181-183.

Cropp, R. J., Seslija, P., Tso, D., & Thakur, Y. (2013). Scanner and kVp dependence of measured CT numbers in the ACR CT phantom. *Journal of applied clinical medical physics, 14*(6), 338-349.

Davis, N., & Jyothirmayi, R. (2017). A nationwide survey of UK oncologists' views on the choice of radiotherapy regime for the reconstructed chest wall in breast cancer patients. *International journal of breast cancer, 2017*.

de Blok, C. J. M., Klaver, M., Wiepjes, C. M., Nota, N. M., Heijboer, A. C., Fisher, A. D., . . . den Heijer, M. (2018). Breast development in transwomen after 1 year of cross-sex hormone therapy: results of a prospective multicenter study. *The Journal of Clinical Endocrinology & Metabolism, 103*(2), 532-538.

DePuey, E. G., Morley, J., & Leykekhman, A. (2019). Shifting breast attenuation artifact mimicking ischemia: Resolved with attenuation correction. *Journal of Nuclear Cardiology, 26*(6), 2142-2147.

Dewaraja, Y. K., Ljungberg, M., Green, A. J., Zanzonico, P. B., Frey, E. C., Bolch, W. E., . . . Howell, R. W. (2013). MIRD pamphlet no. 24: guidelines for quantitative 131I SPECT in dosimetry applications. *Journal of Nuclear Medicine, 54*(12), 2182-2188.

DiFilippo, F. P., & Brunken, R. C. (2005). Do implanted pacemaker leads and ICD leads cause metal-related artifact in cardiac PET/CT? *Journal of Nuclear Medicine, 46*(3), 436-443.

Dorbala, S., Ananthasubramaniam, K., Armstrong, I. S., Chareonthaitawee, P., DePuey, E. G., Einstein, A. J., . . . Park, M. (2018a). Single photon emission computed tomography (SPECT) myocardial perfusion imaging guidelines: instrumentation, acquisition, processing, and interpretation. *Journal of Nuclear Cardiology, 25*(5), 1784-1846.

Dorbala, S., Ananthasubramaniam, K., Armstrong, I. S., Chareonthaitawee, P., DePuey, E. G., Einstein, A. J., . . . Park, M.-A. (2018b). Single photon emission computed tomography (SPECT) myocardial perfusion imaging guidelines: instrumentation, acquisition, processing, and interpretation. *Journal of Nuclear Cardiology, 25*(5), 1784-1846.

Douglas, P. S., & Daubert, M. A. (2015). Diagnostic accuracy of noninvasive testing: necessary but insufficient. In: Am Heart Assoc.

Driessen, R. S., Raijmakers, P. G., Stuijfzand, W. J., & Knaapen, P. (2017). Myocardial perfusion imaging with PET. *The international journal of cardiovascular imaging, 33*(7), 1021-1031.

Duan, H., Ferri, V., Castaneda, P., Visser, T., Luong, K., Davidzon, G., . . . Iagaru, A. (2022). Head-to-head Comparison Of A Conventional Or CZT-based SPECT/CT With A Next Generation Multidetector CZT-based SPECT/CT System. In: Soc Nuclear Med.

Dvorak, R. A., Brown, R. K., & Corbett, J. R. (2011). Interpretation of SPECT/CT myocardial perfusion images: common artifacts and quality control techniques. *Radiographics, 31*(7), 2041-2057.

Engbers, E. M., Timmer, J. R., Mouden, M., Knollema, S., Jager, P. L., & Ottervanger, J. P. (2017). Prognostic value of myocardial perfusion imaging with a cadmium-zinc-telluride SPECT camera in patients suspected of having coronary artery disease. *Journal of Nuclear Medicine, 58*(9), 1459-1463.

Esmaeili, F., Johari, M., Haddadi, P., & Vatankhah, M. (2012). Beam hardening artifacts: comparison between two cone beam computed tomography scanners. *Journal of dental research, dental clinics, dental prospects, 6*(2), 49.

Esmaeilzadeh, M., Parsaee, M., & Maleki, M. (2013). The role of echocardiography in coronary artery disease and acute myocardial infarction. *The journal of Tehran university heart center, 8*(1), 1.

Etemadi, Z., Ghafarian, P., Bitarafan-Rajabi, A., Malek, H., Rahmim, A., & Ay, M. R. (2018). Is correction for metallic artefacts mandatory in cardiac SPECT/CT imaging in the presence of pacemaker and implantable cardioverter defibrillator leads? *Iranian Journal of Nuclear Medicine, 26*(1), 35-46.

Farrell, C. M., Pinson, J.-A., & Dennett, A. M. (2021). CT Attenuation correction and its impact on image quality of myocardial perfusion imaging in coronary artery disease: A systematic review. *Asia Oceania Journal of Nuclear Medicine and Biology, 9*(1), 31.

Forrester, J. S., & Shah, P. K. (2020). Detection and Management of Coronary Disease in Early Middle Age. *The American journal of medicine, 133*(9), 1011-1013.

Francesco Faletra, N. P., Siew Yen Ho (2008). *Anatomy of the Heart by Multislice Computed Tomography* Francesco Fulvio Faletra, Natesa G. Pandian and Siew Yen Ho.

Frank H. Netter, M. (2014). *Atlas of Human Anatomy*: Elsevier.

Fukami, M., Tamura, K., Nakamura, Y., Nakatsukasa, S., & Sasaki, M. (2020). Evaluating the effectiveness of a single CT method for attenuation correction in stress-rest myocardial perfusion imaging with thallium-201 chloride SPECT. *Radiological physics and technology, 13*(1), 20-26.

Garcheva-Tsacheva, M. (2012). SPECT-CT in myocardial perfusion scintigraphy. *Archive of Oncology, 20*(3-4), 132-135.

Garcia, E. V. (2007). SPECT attenuation correction: an essential tool to realize nuclear cardiology's manifest destiny. *Journal of Nuclear Cardiology, 14*(1), 16-24.

Garner, H. W., Paturzo, M. M., Gaudier, G., Pickhardt, P. J., & Wessell, D. E. (2017). Variation in attenuation in L1 trabecular bone at different tube voltages: caution is warranted when screening for osteoporosis with the use of opportunistic CT. *American Journal of Roentgenology, 208*(1), 165-170.

Gimelli, A., Bottai, M., Quaranta, A., Giorgetti, A., Genovesi, D., & Marzullo, P. (2013). Gender differences in the evaluation of coronary artery disease with a cadmium-zinc telluride camera. *European journal of nuclear medicine and molecular imaging, 40*(10), 1542-1548.

Glazebrook, K. N., Doerge, S., Leng, S., Drees, T. A., Hunt, K. N., Zingula, S. N., . . . McCollough, C. H. (2019). Ability of dual-energy CT to detect silicone gel breast implant rupture and nodal silicone spread. *American Journal of Roentgenology, 212*(4), 933-942.

Gnanasegaran, G., Cook, G., Adamson, K., & Fogelman, I. (2009). *Patterns, variants, artifacts, and pitfalls in conventional radionuclide bone imaging and SPECT/CT.* Paper presented at the Seminars in nuclear medicine.

Goetze, S., Brown, T. L., Lavely, W. C., Zhang, Z., & Bengel, F. M. (2007). Attenuation correction in myocardial perfusion SPECT/CT: effects of misregistration and value of reregistration. *Journal of Nuclear Medicine, 48*(7), 1090-1095.

Goodman, C. M., Cohen, V., Thornby, J., & Netscher, D. (1998). The life span of silicone gel breast implants and a comparison of mammography, ultrasonography, and magnetic resonance imaging in detecting implant rupture: a meta-analysis. *Annals of plastic surgery, 41*(6), 577-585; discussion 585.

Govrin-Yehudain, J., Dvir, H., Preise, D., Govrin-Yehudain, O., & Govreen-Segal, D. (2015). Lightweight breast implants: a novel solution for breast augmentation and reconstruction mammaplasty. *Aesthetic surgery journal, 35*(8), 965-971.

Grantham, K. K., Li, H., Zhao, T., & Klein, E. E. (2015). The impact of CT scan energy on range calculation in proton therapy planning. *Journal of applied clinical medical physics, 16*(6), 100-109.

Hanson, C. A., & Bourque, J. M. (2019). Functional and anatomical imaging in patients with ischemic symptoms and known coronary artery disease. *Current cardiology reports, 21*(8), 1-11.

Hasan, M. R., Khan, M. H. R., Rahman, M. R., Parvez, M. S., Islam, M. R., & Paul, A. K. (2017). Quality Control of Gamma Camera with SPECT Systems. *International Journal of Medical Physics, Clinical Engineering and Radiation Oncology, 6*(03), 225.

Herdman, R., Ernster, V., & Bondurant, S. (2000). Safety of silicone breast implants.

Hilts, M., & Duzenli, C. (2004). *Image noise in X-ray CT polymer gel dosimetry.* Paper presented at the Journal of Physics: Conference Series.

Hirano, S., & Tsumoto, S. (2005). Rough representation of a region of interest in medical images. *International Journal of Approximate Reasoning, 40*(1-2), 23-34.

Hogg, P., Kelly, J., & Mercer, C. (2015). *Digital Mammography*: Springer.

Hsieh, F., Miroshnik, M., & Lam, T. C. (2013). Silicone breast implants are thicker than water. *Plastic and Reconstructive Surgery–Global Open, 1*(6), e43.

Huang, J.-Y., Huang, C.-K., Yen, R.-F., Wu, H.-Y., Tu, Y.-K., Cheng, M.-F., . . . Wu, Y.-W. (2016). Diagnostic performance of attenuation-corrected myocardial perfusion imaging for coronary artery disease: a systematic review and meta-analysis. *Journal of Nuclear Medicine, 57*(12), 1893-1898.

Inoue, Y., Nagahara, K., Kudo, H., & Itoh, H. (2018). CT dose modulation using automatic exposure control in whole-body PET/CT: effects of scout imaging direction and arm positioning. *American journal of nuclear medicine and molecular imaging, 8*(2), 143.

Ionescu, P., Vibert, F., Amé, S., & Mathelin, C. (2021). New Data on the Epidemiology of Breast Implant-Associated Anaplastic Large Cell Lymphoma. *European Journal of Breast Health, 17*(4), 302.

Irving, B. A., Weltman, J. Y., Brock, D. W., Davis, C. K., Gaesser, G. A., & Weltman, A. (2007). NIH ImageJ and Slice-O-Matic computed tomography imaging software to quantify soft tissue. *Obesity, 15*(2), 370-376.

Iskandrian, A. E., & Garcia, E. V. (2016). Nuclear Cardiac Imaging Principles and Applications 5 th Edition. In: Japanese Society of Nuclear Cardiology.

Islamian, J. P., Azazrm, A., Mahmoudian, B., & Gharapapagh, E. (2015). Advances in pinhole and multi-pinhole collimators for single photon emission computed tomography imaging. *World journal of nuclear medicine, 14*(1), 3.

Israel, O., Pellet, O., Biassoni, L., De Palma, D., Estrada-Lobato, E., Gnanasegaran, G., . . . Massalha, S. (2019). Two decades of SPECT/CT–the coming of age of a technology: an updated review of literature evidence. *European journal of nuclear medicine and molecular imaging, 46*(10), 1990-2012.

Jeevan, R. (2020). Reconstructive utilisation and outcomes following mastectomy surgery in women with breast cancer treated in England. *The Annals of The Royal College of Surgeons of England, 102*(2), 110-114.

Jerosch-Herold, M., Seethamraju, R. T., Swingen, C. M., Wilke, N. M., & Stillman, A. E. (2004). Analysis of myocardial perfusion MRI. *Journal of Magnetic Resonance Imaging: An Official Journal of the International Society for Magnetic Resonance in Medicine, 19*(6), 758-770.

Jiang, H. (2009). *Computed tomography: principles, design, artifacts, and recent advances.* Paper presented at the SPIE.

Jones, D. W., Hogg, P., & Seeram, E. (2013). *Practical SPECT/CT in nuclear medicine*: Springer.

Joseph Lee , & Delaney, F. T. (2021). Prevalence and clinical significance of incidental findings on CT attenuation correction for myocardial perfusion imaging. *Journal of Nuclear Cardiology*, 1-10.

Kanhai, R., Hage, J. J., Asscheman, H., & Mulder, J. W. (1999). Augmentation mammaplasty in male-to-female transsexuals. *Plastic and reconstructive surgery, 104*(2), 542-549; discussion 550.

Kaoutzanis, C., Winocour, J., Unger, J., Gabriel, A., & Maxwell, G. P. (2019). *The evolution of breast implants.* Paper presented at the Seminars in plastic surgery.

Kaufmann, P. A., & Camici, P. G. (2005). Myocardial blood flow measurement by PET: technical aspects and clinical applications. *Journal of Nuclear Medicine, 46*(1), 75-88.

Kayugawa, A., Noto, Y., Taga, T., Fukaya, T., Tasaki, K., Fujioka, T., & Ohkubo, M. (2015). *Characterization of the model-based iterative reconstruction algorithm: Confirmation of coexistence of dose reduction and spatial resolution improvement.*

Kern, M. J., Sorajja, P., & Lim, M. J. (2015). *Cardiac catheterization handbook*: Elsevier Health Sciences.

Khairuddin, A., Azir, K. F. K., & Kan, P. E. (2017). *Limitations and future of electrocardiography devices: A review and the perspective from the Internet of Things.* Paper presented at the 2017 International Conference on Research and Innovation in Information Systems (ICRIIS).

Kikuchi, N., Yanagawa, M., Enchi, Y., Nakayama, A., Yoshida, Y., Miyata, T., . . . Tomiyama, N. (2020). The effect of the reconstruction algorithm for the pulmonary nodule detection under the metal artifact caused by a pacemaker. *Medicine, 99*(24).

Kumar, S., Pandey, A. K., Sharma, P., Malhotra, A., & Kumar, R. (2012). Optimization of the CT acquisition protocol to reduce patient dose without compromising the diagnostic quality for PET-CT: a phantom study. *Nuclear medicine communications, 33*(2), 164-170.

Kuttner, S., Bujila, R., Kortesniemi, M., Andersson, H., Kull, L., Østerås, B. H., . . . Tarp, I. S. (2013). A proposed protocol for acceptance and constancy control of computed tomography systems: a Nordic Association for Clinical Physics (NACP) work group report. *Acta Radiologica, 54*(2), 188-198.

Lamba, R., McGahan, J. P., Corwin, M. T., Li, C.-S., Tran, T., Seibert, J. A., & Boone, J. M. (2014). CT Hounsfield numbers of soft tissues on unenhanced abdominal CT scans:

variability between two different manufacturers' MDCT scanners. *American Journal of Roentgenology, 203*(5), 1013-1020.

Laspas, F., Pipikos, T., Karatzis, E., Georgakopoulos, N., Prassopoulos, V., Andreou, J., . . . Danias, P. G. (2020). Cardiac magnetic resonance versus single-photon emission computed tomography for detecting coronary artery disease and myocardial ischemia: comparison with coronary angiography. *Diagnostics, 10*(4), 190.

Lawson, S., Avram, A., Dewaraja, Y., & Ackermann, R. (2016a). Phantom study evaluating effect of lowering CT tube current for attenuation correction in quantitative SPECT. *Journal of Nuclear Medicine, 57*(supplement 2), 1883-1883.

Lawson, S., Avram, A., Dewaraja, Y., & Ackermann, R. (2016b). Phantom study evaluating effect of lowering CT tube current for attenuation correction in quantitative SPECT. In: Soc Nuclear Med.

Lee, Qutub, M. A., Aljizeeri, A., & Chow, B. J. (2013). Integrating anatomical and functional imaging for the assessment of coronary artery disease. *Expert review of cardiovascular therapy, 11*(10), 1301-1310.

Lee, D. C., & Klocke, F. J. (2006). Magnetic resonance approaches and recent advances in myocardial perfusion imaging. *Current cardiology reports, 8*(1), 59-64.

Leischik, R., Dworrak, B., Sanchis-Gomar, F., Lucia, A., Buck, T., & Erbel, R. (2016). Echocardiographic assessment of myocardial ischemia. *Annals of translational medicine, 4*(13).

Levick, J. R. (2013). *An introduction to cardiovascular physiology*: Butterworth-Heinemann.

Lilly, L. S., & Braunwald, E. (2012). *Braunwald's heart disease: a textbook of cardiovascular medicine* (Vol. 2): Elsevier Health Sciences.

Liu, J. L., Maniadakis, N., Gray, A., & Rayner, M. (2002). The economic burden of coronary heart disease in the UK. *Heart, 88*(6), 597-603.

Livieratos, L. (2015). *Technical pitfalls and limitations of SPECT/CT.* Paper presented at the Seminars in nuclear medicine.

Ljungberg, M., & Pretorius, P. H. (2018). SPECT/CT: an update on technological developments and clinical applications. *The British journal of radiology, 91*(1081), 20160402.

MacCance, K. L., Huether, S. E., Brashers,V. L. & Rote, N. S. (2010). *Pathophysiology: The biologic bases for disease in adults and children* (6 ed.): Maryland Heights, MO: Mosby Elsevier.

Mahmoudi, R., Jabbari, N., Aghdasi, M., & Khalkhali, H. R. (2016). Energy dependence of measured CT numbers on substituted materials used for CT number calibration of radiotherapy treatment planning systems. *Plos one, 11*(7), e0158828.

Mahur, M., Gurjar, O. P., Grover, R., Negi, P., Sharma, R., Singh, A., & Singh, M. (2017). Evaluation of effect of different computed tomography scanning protocols on Hounsfield unit and its impact on dose calculation by treatment planning system. *Iranian Journal of Medical Physics, 14*(3), 149-154.

Malakar, A. K., Choudhury, D., Halder, B., Paul, P., Uddin, A., & Chakraborty, S. (2019). A review on coronary artery disease, its risk factors, and therapeutics. *Journal of cellular physiology, 234*(10), 16812-16823.

Mannarino, T., Assante, R., Ricciardi, C., Zampella, E., Nappi, C., Gaudieri, V., . . . Cesarelli, M. (2019). Head-to-head comparison of diagnostic accuracy of stress-only myocardial perfusion imaging with conventional and cadmium-zinc telluride single-photon emission computed tomography in women with suspected coronary artery disease. *Journal of Nuclear Cardiology*, 1-10.

Mariani, G., Bruselli, L., Kuwert, T., Kim, E. E., Flotats, A., Israel, O., . . . Watanabe, N. (2010). A review on the clinical uses of SPECT/CT. *European journal of nuclear medicine and molecular imaging, 37*(10), 1959-1985.

Masood, Y., Liu, Y.-H., DePuey, G., Taillefer, R., Araujo, L. I., Allen, S., . . . Zito, M.-J. (2005). Clinical validation of SPECT attenuation correction using x-ray computed tomography–derived attenuation maps: multicenter clinical trial with angiographic correlation. *Journal of Nuclear Cardiology, 12*(6), 676-686.

Mathur, S., Heller, G. V., Bateman, T. M., Ruffin, R., Yekta, A., Katten, D., . . . Ahlberg, A. W. (2013). Clinical value of stress-only Tc-99m SPECT imaging: importance of attenuation correction. *Journal of Nuclear Cardiology, 20*(1), 27-37.

Maurovich-Horvat, P., Ferencik, M., Voros, S., Merkely, B., & Hoffmann, U. (2014). Comprehensive plaque assessment by coronary CT angiography. *Nature Reviews Cardiology, 11*(7), 390-402.

Maxwell, G., Baker, M., & Gabriel, A. (2006). Augmentation mammaplasty: general considerations. *Surgery of the Breast, 2nd Ed. Baltimore: Lippincott Williams & Wilkins*, 1237.

Maxwell, G. P., & Gabriel, A. (2017). Breast implant design. *Gland surgery, 6*(2), 148.

McGuire, K. P. (2016). Breast anatomy and physiology. In *Breast Disease* (pp. 1-14): Springer.

Meine, T. J., Patel, M. R., Heitner, J., Fortin, T. A., Pagnanelli, R. A., Gehrig, T. R., . . . Borges-Neto, S. (2005). Cardiac imaging impaired by a silicone breast implant. *Clinical nuclear medicine, 30*(4), 262-264.

Members, T. F., Montalescot, G., Sechtem, U., Achenbach, S., Andreotti, F., Arden, C., . . . Cuisset, T. (2013). 2013 ESC guidelines on the management of stable coronary artery disease: the Task Force on the management of stable coronary artery disease of the European Society of Cardiology. *European heart journal, 34*(38), 2949-3003.

Mettler Jr, F. A., & Guiberteau, M. J. (2012). *Essentials of Nuclear Medicine Imaging: Expert Consult-Online and Print*: Elsevier Health Sciences.

Miles, J., Cullom, S. J., & Case, J. A. (1999). An introduction to attenuation correction. *Journal of Nuclear Cardiology, 6*(4), 449-457.

Miller, T. J., Wilson, S. C., Massie, J. P., Morrison, S. D., & Satterwhite, T. (2019). Breast augmentation in male-to-female transgender patients: Technical considerations and outcomes. *JPRAS open, 21*, 63-74.

Miseré, R. M., van Kuijk, S. M., Claassens, E. L., Heuts, E. M., Piatkowski, A. A., & van der Hulst, R. R. (2021). Breast-related and body-related quality of life following autologous breast reconstruction is superior to implant-based breast reconstruction-A long-term follow-up study. *The Breast, 59*, 176-182.

Morrish, O., & Goldstone, K. (2008). An investigation into patient and staff doses from X-ray angiography during coronary interventional procedures. *The British journal of radiology, 81*(961), 35-45.

Mory, C., Auvray, V., Zhang, B., Grass, M., Schäfer, D., Chen, S. J., . . . Douek, P. (2014). Cardiac C-arm computed tomography using a 3D+ time ROI reconstruction method with spatial and temporal regularization. *Medical physics, 41*(2), 021903.

Moss, A. J., Williams, M. C., Newby, D. E., & Nicol, E. D. (2017). The updated NICE guidelines: cardiac CT as the first-line test for coronary artery disease. *Current cardiovascular imaging reports, 10*(5), 15.

Mousa, A., Kusminarto, K., & Suparta, G. B. (2017). A new simple method to measure the X-ray linear attenuation coefficients of materials using micro-digital radiography machine. *Int. J. Appl. Eng. Res, 12*(21), 10589-10594.

Nichols, K. J., & Van Tosh, A. (2019). Rotating and stationary SPECT system patient motion myocardial perfusion artifacts. In: Springer.

Nikolaou, K., Alkadhi, H., Bamberg, F., Leschka, S., & Wintersperger, B. J. (2011). MRI and CT in the diagnosis of coronary artery disease: indications and applications. *Insights into imaging, 2*(1), 9-24.

Nowbar, A. N., Gitto, M., Howard, J. P., Francis, D. P., & Al-Lamee, R. (2019). Mortality From Ischemic Heart Disease. *Circ Cardiovasc Qual Outcomes, 12*(6), e005375. doi:10.1161/CIRCOUTCOMES.118.005375

Oddstig, J., Hedeer, F., Jögi, J., Carlsson, M., Hindorf, C., & Engblom, H. (2013). Reduced administered activity, reduced acquisition time, and preserved image quality for the new CZT camera. *Journal of Nuclear Cardiology, 20*(1), 38-44.

Ogawa, K. (2004). Image distortion and correction in single photon emission CT. *Annals of nuclear medicine, 18*(3), 171-185.

Okuda, K., Nakajima, K., Kikuchi, A., Onoguchi, M., & Hashimoto, M. (2017). Cardiac and respiratory motion-induced artifact in myocardial perfusion SPECT 4D digital anthropomorphic phantom study. *Annals of Nuclear Cardiology, 3*(1), 88-93.

Ozcan, U. A., Ulus, S., & Kucukcelebi, A. (2019). Breast augmentation with Aquafilling: complications and radiologic features of two cases. *European Journal of Plastic Surgery, 42*(4), 405-408.

Pandya, S., & Moore, R. G. (2011). Breast development and anatomy. *Clinical obstetrics and gynecology, 54*(1), 91-95.

Park, J.-H., Park, J.-U., & Chang, H. (2021). Advances in Biomaterials for Breast Reconstruction. *Applied Sciences, 11*(16), 7493.

PASSAU, K. (2011). A comparison of Attenuation Correction methods in 111 In-Pentetriotide abdominal SPECT. *reconstruction, 900*(1), 2.

Paternò, G., Cardarelli, P., Gambaccini, M., Serafini, L., Petrillo, V., Drebot, I., & Taibi, A. (2019). Inverse Compton radiation: a novel x-ray source for K-edge subtraction angiography? *Physics in Medicine & Biology, 64*(18), 185002.

Peters, W. (2002). The evolution of breast implants. *Canadian Journal of Plastic Surgery, 10*(5), 223-236.

Philip I. Aaronson, J. P. T. W., Michelle J. Connolly. (2013). *<The cardiovascular system at a glance by Philip I Aaronson Jeremy P T Ward Michelle J Connolly (z-lib.org).pdf>*.

Pienaar, W., McWilliams, S., Wilding, L., & Perera, I. (2011). The imaging features of MACROLANE™ in breast augmentation. *Clinical radiology, 66*(10), 977-983.

Pirayesh, E. (2021). The truncation artifact in a skinny patient following myocardial perfusion SPECT. *Iranian Journal of Nuclear Medicine, 29*(1), 35-37.

Płachcińska, A., Włodarczyk, M., Kovacevic-Kuśmierek, K., Bieńkiewicz, M., Drożdż, J., Chiżyński, K., . . . Kuśmierek, J. (2016). Diagnostic performance of myocardial perfusion single-photon emission computed tomography with attenuation correction. *Kardiologia Polska (Polish Heart Journal), 74*(1), 32-39.

Polonsky, T. S., McClelland, R. L., Jorgensen, N. W., Bild, D. E., Burke, G. L., Guerci, A. D., & Greenland, P. (2010). Coronary artery calcium score and risk classification for coronary heart disease prediction. *Jama, 303*(16), 1610-1616.

Polycarpou, I., Chrysanthou-Baustert, I., Demetriadou, O., Parpottas, Y., Panagidis, C., Marsden, P. K., & Livieratos, L. (2017). Impact of respiratory motion correction on SPECT myocardial perfusion imaging using a mechanically moving phantom assembly with variable cardiac defects. *Journal of Nuclear Cardiology, 24*(4), 1216-1225.

Preuss, R., Weise, R., Lindner, O., Fricke, E., Fricke, H., & Burchert, W. (2008). Optimisation of protocol for low dose CT-derived attenuation correction in

myocardial perfusion SPECT imaging. *European journal of nuclear medicine and molecular imaging, 35*(6), 1133-1141.

Purser, N. J., Armstrong, I. S., Williams, H. A., Tonge, C. M., & Lawson, R. S. (2008). Apical thinning: real or artefact? *Nuclear medicine communications, 29*(4), 382-389.

Qutbi, M., & Soltanshahi, M. (2018). A practical method to reduce breast attenuation during SPECT myocardial perfusion imaging. *Journal of Nuclear Cardiology, 25*(6), 2179-2181.

Ramos, S. M. O., Glavam, A. P., de Brito, A. S., Kubo, T. T. A., Tukamoto, G., Sampaio, D. d. C. P., & de Sá, L. V. (2020). Prone Myocardial Perfusion Imaging and Breast Attenuation: A Phantom Study. *Current Medical Imaging, 16*(1), 70-79.

Ramos, S. M. O., Glavam, A. P., de Brito, A. S. X., Kubo, T. T. A., Tukamoto, G., Sampaio, D., & de Sa, L. V. (2020). Prone Myocardial Perfusion Imaging and Breast Attenuation: A Phantom Study. *Current medical imaging reviews, 16*(1), 70-79.

Ramos, S. M. O., Glavam, A. P., Kubo, T. T. A., & Sá, L. V. d. (2014). Optimization of a protocol for myocardial perfusion scintigraphy by using an anthropomorphic phantom. *Radiologia Brasileira, 47*, 217-222.

Rep, M. S., Attard, M., Camoni, L., & Santos, A. (2017). Quality control of nuclear medicine instrumentation and protocol standardisation. EANM Technologist's Guide.

Roh, T. S. (2016). Position Statement of Korean Academic Society of Aesthetic and Reconstructive Breast Surgery: Concerning the Use of Aquafilling (R) for Breast Augmentation. *Archives of Aesthetic Plastic Surgery, 22*(1), 45-46.

Saba, L. (2017). *Imaging of the cardiovascular system, thorax, and abdomen*: CRC Press.

Saini, A., Pandey, V., Kumar, P., Singh, A., & Pasricha, R. (2021). Investigation of tube voltage dependence on CT number and its effect on dose calculation algorithms using thorax phantom in Monaco treatment planning system for external beam radiation therapy. *Journal of Medical Physics, 46*(4), 315.

Saleki, L., Ghafarian, P., Bitarafan-Rajabi, A., Yaghoobi, N., Fallahi, B., & Ay, M. R. (2019). The influence of misregistration between CT and SPECT images on the accuracy of CT-based attenuation correction of cardiac SPECT/CT imaging: Phantom and clinical studies. *Iranian Journal of Nuclear Medicine, 27*(2), 63-72.

Salih, N., Hamid, H., Bakar, N., Yahya, A., & Dewi, D. Structural Characterization of ECG-gated Cardiac CT Images: Texture Analysis on Systole and Diastole Phases.

Sawyer, J. D., Franke, J., Scaife, S., Sommer, N. Z., & Neumeister, M. W. (2022). Autologous Breast Reconstruction is Associated with Lower 90-day Readmission Rates. *Plastic and Reconstructive Surgery Global Open, 10*(2).

Schindler, T. H., Bateman, T. M., Berman, D. S., Chareonthaitawee, P., De Blanche, L. E., Dilsizian, V., . . . Soman, P. (2020). Appropriate use criteria for PET myocardial perfusion imaging. *Journal of Nuclear Medicine, 61*(8), 1221-1265.

Schmauss, D., Machens, H.-G., & Harder, Y. (2016). Breast reconstruction after mastectomy. *Frontiers in surgery, 2*, 71.

Schuijf, J. D., Shaw, L. J., Wijns, W., Lamb, H. J., Poldermans, D., de Roos, A., . . . Bax, J. J. (2005). Cardiac imaging in coronary artery disease: differing modalities. *Heart, 91*(8), 1110-1117.

Schulze, R., Heil, U., Groß, D., Bruellmann, D., Dranischnikow, E., Schwanecke, U., & Schoemer, E. (2011). Artefacts in CBCT: a review. *Dentomaxillofacial Radiology, 40*(5), 265-273.

Seo, Y., Mari, C., & Hasegawa, B. H. (2008). *Technological development and advances in single-photon emission computed tomography/computed tomography.* Paper presented at the Seminars in nuclear medicine.

Sharma, P., Patel, C. D., Karunanithi, S., Maharjan, S., & Malhotra, A. (2012). Comparative accuracy of CT attenuation-corrected and non–attenuation-corrected SPECT myocardial perfusion imaging. *Clinical nuclear medicine, 37*(4), 332-338.

Sharp, P. F., Gemmell, H. G., Murray, A. D., & Sharp, P. F. (2005). *Practical nuclear medicine*: Springer.

Shcherbinin, S., Celler, A., Belhocine, T., Vanderwerf, R., & Driedger, A. (2008). Accuracy of quantitative reconstructions in SPECT/CT imaging. *Physics in Medicine & Biology, 53*(17), 4595.

Sherwood, L. (2010). *<Human physiology. From cells to systems >*.

Shin, J. H., Suh, J. S., & Yang, S. G. (2015). Correcting shape and size using temporary filler after breast augmentation with silicone implants. *Archives of Aesthetic Plastic Surgery, 21*(3), 124-126.

Sicari, R., & Cortigiani, L. (2017). The clinical use of stress echocardiography in ischemic heart disease. *Cardiovascular Ultrasound, 15*(1), 1-16.

Slezák, P., & Waczulíková, I. (2011). Reproducibility and repeatability. *Physiol Res, 60*, 203-205.

Son, M. J., Ko, K. H., Jung, H. K., Koh, J. E., & Park, A. Y. (2018). Complications and radiologic features of breast augmentation via injection of aquafilling gel. *Journal of Ultrasound in Medicine, 37*(7), 1835-1839.

Spear, S. L., & Jespersen, M. R. (2010). Breast implants: saline or silicone? *Aesthetic surgery journal, 30*(4), 557-570.

Stary, H. C., Chandler, A. B., Dinsmore, R. E., Fuster, V., Glagov, S., Insull Jr, W., . . . Wissler, R. W. (1995). A definition of advanced types of atherosclerotic lesions and a histological classification of atherosclerosis: a report from the Committee on Vascular Lesions of the Council on Arteriosclerosis, American Heart Association. *Circulation, 92*(5), 1355-1374.

Stinis, C. T., Lizotte, P. E., & Movahed, M.-R. (2006). Impaired myocardial SPECT imaging secondary to silicon-and saline-containing breast implants. *The international journal of cardiovascular imaging, 22*(3), 449-455.

Streed Jr, C. G., Harfouch, O., Marvel, F., Blumenthal, R. S., Martin, S. S., & Mukherjee, M. (2017). Cardiovascular disease among transgender adults receiving hormone therapy: a narrative review. *Annals of internal medicine, 167*(4), 256-267.

Stupic, K. F., Ainslie, M., Boss, M. A., Charles, C., Dienstfrey, A. M., Evelhoch, J. L., . . . Hill, D. L. (2021). A standard system phantom for magnetic resonance imaging. *Magnetic resonance in medicine*.

SURGEONS, B. A. O. A. P. (28 February 2021). BAAPS Annual Audit Results. Retrieved from https://baaps.org.uk/baaps_annual_audit_results_.aspx

Surgeons, B. A. o. A. P. (2019, March 27). COSMETIC SURGERY STATS: DAD BODS AND FILTER JOBS,. Retrieved from https://baaps.org.uk/media/press_releases/1535/cosmetic_surgery_stats_dad_bods_and_filter_jobs

Tadesse, G. F., Geramifar, P., Tegaw, E. M., & Ay, M. R. (2019). Techniques for generating attenuation map using cardiac SPECT emission data only: a systematic review. *Annals of nuclear medicine, 33*(1), 1-13.

Tang, K., Wang, L., Li, R., Lin, J., Zheng, X., & Cao, G. (2012). Effect of low tube voltage on image quality, radiation dose, and low-contrast detectability at abdominal multidetector CT: phantom study. *Journal of Biomedicine and Biotechnology, 2012*.

Tantawy, H. M., Abdelhafez, Y. G., Helal, N. L., Kany, A. I., & Saad, I. E. (2020). Effect of correction methods on image resolution of myocardial perfusion imaging using single

photon emission computed tomography combined with computed tomography hybrid systems. *Journal of Physics Communications, 4*(1), 015011.

Tautz, L., Friman, O., Hennemuth, A., Seeger, A., & Peitgen, H.-O. (2011). Automatic detection of a heart ROI in perfusion MRI images. In *Bildverarbeitung für die Medizin 2011* (pp. 259-263): Springer.

Thompson, J., Hogg, P., Higham, S., & Manning, D. (2013). Accurate localization of incidental findings on the computed tomography attenuation correction image: the influence of tube current variation. *Nuclear medicine communications, 34*(2), 180-184.

Tonge, C. M., Ellul, G., Pandit, M., Lawson, R. S., Shields, R. A., Arumugam, P., & Prescott, M. C. (2006). The value of registration correction in the attenuation correction of myocardial SPECT studies using low resolution computed tomography images. *Nuclear medicine communications, 27*(11), 843-852.

Trignano, E., Baccari, M., Pili, N., Serra, P. L., & Rubino, C. (2020). Complications after breast augmentation with hyaluronic acid: a case report. *Gland surgery, 9*(6), 2193.

Underwood, S., Anagnostopoulos, C., Cerqueira, M., Ell, P., Flint, E., Harbinson, M., . . . Shaw, L. (2004). Myocardial perfusion scintigraphy: the evidence. *European journal of nuclear medicine and molecular imaging, 31*(2), 261-291.

Unukovych, D., Khrapach, V., Wickman, M., Liljegren, A., Mishalov, V., Patlazhan, G., & Sandelin, K. (2012). Polyacrylamide gel injections for breast augmentation: management of complications in 106 patients, a multicenter study. *World journal of surgery, 36*(4), 695-701.

Vallabhajosula, S. (2009). *Molecular imaging: radiopharmaceuticals for PET and SPECT*: Springer Science & Business Media.

Van Audenhaege, K., Van Holen, R., Vandenberghe, S., Vanhove, C., Metzler, S. D., & Moore, S. C. (2015). Review of SPECT collimator selection, optimization, and fabrication for clinical and preclinical imaging. *Medical physics, 42*(8), 4796-4813.

Van den Wyngaert, T., Elvas, F., De Schepper, S., Kennedy, J. A., & Israel, O. (2020). SPECT/CT: standing on the shoulders of giants, it is time to reach for the sky! *Journal of Nuclear Medicine, 61*(9), 1284-1291.

Verberne, H. J., Acampa, W., Anagnostopoulos, C., Ballinger, J., Bengel, F., De Bondt, P., . . . Flotats, A. (2015). EANM procedural guidelines for radionuclide myocardial perfusion imaging with SPECT and SPECT/CT: 2015 revision. *European journal of nuclear medicine and molecular imaging, 42*(12), 1929-1940.

Verberne, H. J., Acampa, W., Anagnostopoulos, C., Ballinger, J., Bengel, F., De Bondt, P., . . . Flotats, A. (2018). EANM procedural guidelines for radionuclide myocardial perfusion imaging with SPECT and SPECT/CT. In: CT.

Villa, A. D., Sammut, E., Nair, A., Rajani, R., Bonamini, R., & Chiribiri, A. (2016). Coronary artery anomalies overview: The normal and the abnormal. *World J Radiol, 8*(6), 537-555. doi:10.4329/wjr.v8.i6.537

von Heimburg, D., Zachariah, S., Low, A., & Pallua, N. (2001). Influence of different biodegradable carriers on the in vivo behavior of human adipose precursor cells. *Plastic and reconstructive surgery, 108*(2), 411-420; discussion 421.

Votavová, R., Linhartová, A., Kořínek, J., Marek, J., & Linhart, A. (2015). Echocardiography in coronary artery disease. *Cor et Vasa, 57*(6), e408-e418.

Walz-Flannigan, A. I., Brossoit, K. J., Magnuson, D. J., & Schueler, B. A. (2018). Pictorial review of digital radiography artifacts. *Radiographics, 38*(3), 833-846.

Weinmann, A. L., Hruska, C. B., & O'Connor, M. K. (2009). Design of optimal collimation for dedicated molecular breast imaging systems. *Medical physics, 36*(3), 845-856.

Wierckx, K., Gooren, L., & T'Sjoen, G. (2014). Clinical review: breast development in trans women receiving cross-sex hormones. *The journal of sexual medicine, 11*(5), 1240-1247.

Wosnitzer, B., Gadiraju, R., & DePuey, G. (2011). The truncation artifact. *Journal of Nuclear Cardiology, 18*(1), 187-191.

Yada, N., & Onishi, H. (2016). Validation of computed tomography-based attenuation correction of deviation between theoretical and actual values in four computed tomography scanners. *Asia Oceania Journal of Nuclear Medicine and Biology, 4*(2), 81.

Young, V. L., & Watson, M. E. (2001). Breast implant research: where we have been, where we are, where we need to go. *Clinics in plastic surgery, 28*(3), 451-483.

Zaidi, H., Montandon, M.-L., & Alavi, A. (2007). Advances in attenuation correction techniques in PET. *PET clinics, 2*(2), 191-217.

Zhang, D., Sun, J., Pretorius, P. H., King, M., & Mok, G. S. (2020). Clinical evaluation of three respiratory gating schemes for different respiratory patterns on cardiac SPECT. *Medical physics, 47*(9), 4223-4232.

Zipes, D. P., Libby, P., Bonow, R. O., Mann, D. L., & Tomaselli, G. F. (2018). *Braunwald's heart disease e-book: A textbook of cardiovascular medicine*: Elsevier Health Sciences.